UNIVERSITY OF OSLO
Physics of Geological Processes

BLOWING THE VISCOELASTIC TRUMPET

Experiment Design for Mapping Stress-Strain Patterns in Viscoelastic Hydrofracture

Master Thesis

Håvard Svanes Bertelsen

2014-07-16

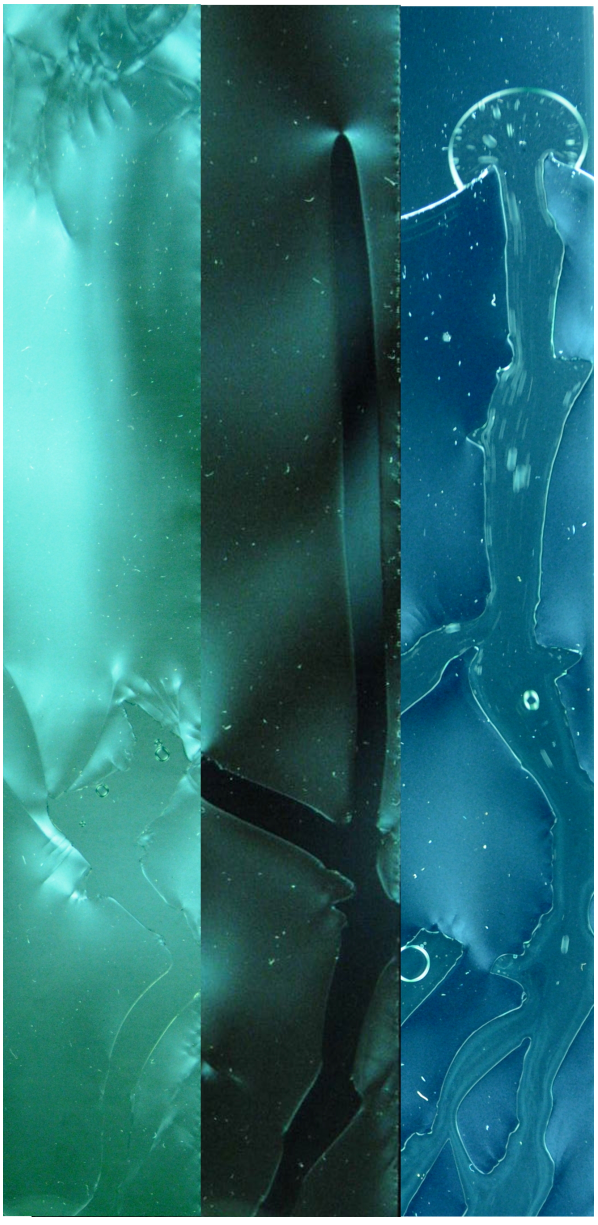

"A goal is not always meant to be reached, it often serves simply as something to aim at. "

Bruce Lee

Preface

Too many months ago I started this project with enthusiasm and curiosity. I was given the complex task of developing an original scientific method robust enough to carry out functional experimental stress-strain analysis in viscoelastic media as an analogue for magma intrusion. It was all to be done with old school science and rough prototyping under the concept of "simplicity is the last step of art". Needless to say, I was exited.

Through my studies I gained hands-on experience in experiment design and rough prototyping, and I have sacrificed blood, sweat and tears in the frontline of science, notably from cutting myself on glass shards from broken experiments. I have delved in the deep, dark caves of complex rheology and found that the more I think I know, the less I truly know — and that laponite is a devious clay that will deceit you if you do not follow a rigorous sample protocol.

These words are the fruits of labor from this long and cumbersome project. They cannot express the neverending days in the lab, the sadness and tiredness with each failed attempt, nor the joy and newfound hope when success came within reach.

I am grateful in particular to the intellectual origin of my project at PGP, professor Olivier Galland and professor Dag K. Dysthe — it takes ingenuity to design a task so simple, yet so complex. If one thing I wish I had taken the time to discuss more with you. I would like to thank the research technician Elijah Jeremiah Aller for sharing his expertise as a glassblower and thereby putting an end to my glass testcells shattering when least wanted. I would also like to thank my significant other, Marit-Kristine, and my friends and family for illuding me into believing in my self and inspiring me to carry on. Last but not least I thank my doctor and therapists for providing various pain relief when my herniated disks have been acting out after extensive sitting and studying.

I hope you will enjoy reading this thesis!

Håvard Svanes Bertelsen
University of Oslo 2014-07-16

Abstract

Magma is the foremost contributor to transporting mass and heat through the Earth's crust and knowledge of its ascent mechanics is of great importance for understanding geological processes. Magma intrusions are linked with resource emplacement, thus intrusion mechanisms has implications for effective resource extraction in e.g. mining, oil and gas drilling.

In this thesis I explore the possibilities and challenges in utilizing optical rheometry and velocimetry in couple to observe the stress-strain relationships and deformation features of viscous fingering and hydrofracturing of complex viscoelastic materials as an analog for magma intrusions. With a self-made prototype of the concept I examined the deformation features of a colloidal smectite clay suspension, posing as a host rock analog, intruded with olive oil.

The results of the concept conceived are very promising. The use of a polariscope to obtain the birefringence pattern of the flow display a wide variety of features that are invisible to the human eye. The observations include several artifacts with similar appearance as structural geological features. One major implication of this research is the fact that intrusions that look viscous exhibit elastic stress-patterns and fractures when observed through a polariscope. Several prior works need to consider their conclusions on categorization of fracture patterns. This alone proves the validity of the concept.

A significant conclusion from the experiments is that the rheological response in a gel matrix subjected to fluid injection is indeed dependent on viscosity ratio.

In addition to the observational results, the smectite host rock analog used in the experiments have proved to display a wide range of viscoelastic behaviour. The sample preparation protocol needs to be rigourous to achieve reproducible results, but laponite serves well in modelling viscoelastic deformation.

Contents

List of Figures

List of Tables

Chapter 1

Introduction

1.1 The brittle versus ductile controverse

Magma is the foremost contributor to transporting mass and heat through the Earth's crust. Composing a mixture of molten rock, volatiles, and solids, magma is formed deep within the crust and in the upper mantle. If the magma buoyancy overcomes the host rock resistance to deformation, the magma ascends from the deep — cracking and displacing rock on its way towards the surface.

The nature of this cracking and displacing influences the rate and direction of the magma transport, how far the magma travels before it freezes, the degree of chemical reaction with the host rock, the morphology of volcanic landforms on the surface, and even the interplay between magmatism and regional tectonics [30, 31].

Contrasting morphologies are observed in frozen and exhumed intrusions in the field, ranging from flow-deformed mushroom-shaped diapirs to fracture-deformed dykes. It is widely recognized that gabbroic intrusions typically are found as narrow dykes, while granites take on more equidimensional diapiric forms [21, 30].

As described in figure (1.1), diapiric rise implies extensive deformation of the host rock and consequently the ascent velocity is controlled essentially by the host rock viscosity, with only small variations between inviscid and rigid magma. In dykes, on the other hand, the wall rock is pushed apart with most of the deformation occuring within the flowing magma, and as a result the ascent velocity is largely controlled by the magma viscosity. So there is a fundamental difference regarding e.g. the ascent rate governing properties of the classical geophysical diapir and dyke [30].

Close spatial arrangements between intrusions and large faults are often

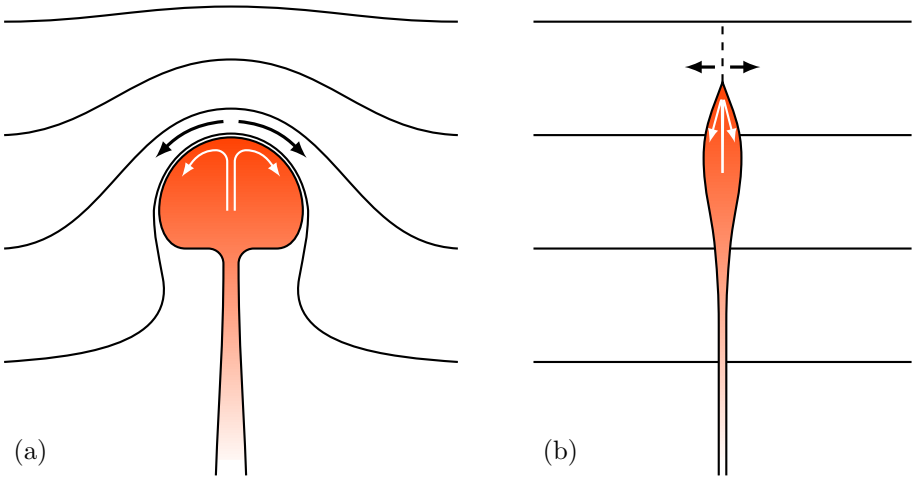

Figure 1.1: Idealized end-member cases of magma uprise. Diapir (a) displacing and intruding viscous host rock, the host rock rising with the diapir. Dike (b) fracturing and intruding elastic host rock, displacement of material adjacent to dyke is negligible. Dike thickness greatly exaggerated. Figure and explanation based on Rubin [30].

observed in the field, and many structural geology cartoons show elongated intrusions in crustal-scale faults. As an example James Hutton, the Scottish geology pioneer, found boulders with granite cutting through metamorphic schists at Glen Tilt in the Cairngorm mountains in the Scottish Highlands as far back as 1785. The deformation pattern, depicted in figure (1.2), showed a granite appearing to be flowing at the time of intrusion, yet it penetrated rather than displacing the host rock [11].

It is well known that rock behaves elastic when the timescale of loading is short, and viscous when the timescale of loading is long, and traditionally dykes and diapirs have been treated as two entirely distinct processes. However, the rheologically complex nature of rocks is generally not perfect elastic, viscous, or plastic; and geodynamic processes operates with several simultaneous characteristic loading times ranging from a fraction of a second, to millions of years. Depending on extrinsic conditions such as state of stress, temperature and strain rate, rock deformation normally exhibits a combination of these ideal models [5, 12].

The segregative view seems also fueled by a somewhat semantic discussion of distinguishing between magma ascent, as vertical growth, and magma emplacement, as horisontal growth [22]. This is part of

Figure 1.2: Map, Glen Tilt, Tayside. A replica of a watercolor done by geologist James Hutton showing a geological map of the Glen Tilt valley, Cairngorm mountains, Scotland. The pattern depicts a granite dyke intruding a metamorphic schist strata. Retrieved from USGS Multimedia Gallery.

the reasoning to several studies concluding that currently equidimensional intrusion originally intruded as dikes before dilating into diapiric forms[30]. From a physics standpoint it should be fairly obvious that dykes and diapirs exhibits both features, albeit the proportion differs, and a separation in the nomenclature does not necessarily mean hybrid growth does not occur.

The ideal diapir and dyke end-members have been extensively studied using analytical, numerical, and experimental methods, and several explanations for how magma and host rock rheology influence the mechanisms of magma ascent have been offered over the last 50 years. Such models are however incapable of describing the intrusion processes in the regime between the ideal end-members[30]. Altough the evidence for transitional behaviour in and around intrusions has been around for hundreds of years and the theoretical framework of viscoelasticity being developed by renowned physicists such as Maxwell, Boltzmann, and Kelvin already in the nineteenth century, little effort has been given towards transitional behaviour for magma intrusions.

The transport and emplacement of granites has been one of the primary concerns of this debate. The equidimensional forms it has been found in has led researchers to believe that the granite plutons were spawned by a entirely viscous diapiric process. However, the rate for such a process to occur close to surface is too slow for the granite to propagate before it freezes, and in recent years a consensus has emerged that recognizes that

granite ascends by fracture *and* flow in a rapid dynamic process operating at timescales of less than houndred thousand years[22].

1.2 Aim of this thesis

Former experimental work on transitional magma ascent has been phenomenological rather than quantitative. In this thesis I therefore seek to develop a conceptual experimental model for quantifying stress-strain relationships in viscoelastic media, and to design a functioning prototype. The model should be able to help enlighten or even answer some of the questions emerging from the brittle versus ductile discussion:

- What properties governs the transition between brittle and ductile intrusion mechanisms?
- How do we identify hybrid behaviour, and how do we identify the end-members of intrusion mechanisms?
- What are the stress-strain relationships in a hybrid intrusion?
- What are the stress-strain relationships at the complex crack-tip process zone?
- Which geologic regimes allows the occurance of hybrid behaviour?

Chapter 2

State of the art

In situ noninvasive observation gives the only certain representation of an ongoing process. Because magma intrusions happen subsurface, direct observation is at present only possible through seismic methods. The information gathered from such methods is however insufficient to resolve the scale or complexity of most intrusions. To break down the unanswered questions of magma intrusions other approaches are more suitable. Field study of exhumed magma intrusions, analogue experiments, and theoretical approaches through mathematics and simulations are the preferred tools in the study of magma intrusions.

In addition to the geological frame of reference one has to consider supplement from other disciplines. In this thesis we discuss shortly the application of stress and strain mapping techniques of photoviscoelasticity from photo mechanics, and birefringent fluid-flow and velocimetry from fluid mechanics.

2.1 Field observations of dykes and diapirs

As mentioned in the introduction, structural mapping of exhumed magma intrusions have a long history, and the literature is extensive. The study of exhumed magma intrusions is restricted to the description of arrested intrusion bodies or conduits where magma transport has occurred. Also, since we in this paper discuss the transitional viscoelastic regime, mainly taking place at great depths, the surfaced remnants of a magma intrusion have undergone significant deformation and metamorphism after the intrusion reached its final state. Nevertheless, such remnants are the only tangible evidence from the transition zone and therefore a vital component in this study.

The closest thing to measure and monitor the ongoing process of a magma intrusion is seismic recording. Because seismic waves propagate efficiently through Earth's interior and interact with its internal structure, they provide a high-resolution noninvasive record of subsurface features. However the high resolution compared to the scale of many subsurface structures is unable to depict but the largest of intrusive bodies, and even for large bodies the complex processes at the crack tip process zone is hidden for seismic techniques. For shallow intrusions below volcanoes the seismic picture is a bit clearer. Joined with geodetic measurements such study can yield valuable information on the dynamics of the process.

The following summary of field observations is short compared to the extent of the literature and is mainly based on Rubin (1995).

2.1.1 From blob to blade

2.1.1.1 Shapes

Because dykes carries little heat, the intrusion deformation can be preserved until the dyke is exhumed. Also, the short timescale of intrusion allows for near real-time seismic and geodetic measurements of dykes in active volcanoes[33]. Observing diapirism is more difficult, owing to the likelihood of post intrusion deformation, and long timescale of intrusion. In outcrops different intrusion patterns are observed for different combinations of host rock and magma rock, e.g. as a rule dolerite typically intrudes in narrow dykes, while granites can be found in more massive equidimensional shapes, e.g. figure (2.1.

In addition significant ductile strain can often be found in the host rock surrounding diapiric intrusions, while the host rock is pushed aside with relatively little deformation in dykes, except at the complex crack tip, leading to the conclusion that viscous deformation plays a large role in diapiric intrusion and less for dyke intrusion. Gabbros and granites vary somewhat in temperature and density, however the major difference is the 2 to 8 orders of magnitude contrast in viscosity, granites being high-viscosity. The patterns observed are consistent with the theory that the timescale of loading increases with the viscosity of the magma[30].Similar effects of viscosity contrast are observed in other natural phenomena, e.g. aqueous fluids intrudes hard rock in cracks, while salt and silt can be found rising through a denser rock in diapirs as seen in figure (2.2)[30].

Varieties of the dyke and diapir shapes like elongated plutons, along with close spatial and temporal relation between plutons and large faults, e.g. Pitcher (1979)[23], suggest hybrid behavior may operate on geologic

Figure 2.1: To the left an exhumed granite massive of diapiric shape and to the right a diabas, dolerite equivalent, dyke. The granite massive photo depicts the Half Dome in Yosemite, while the diabas intrusion is from the Nain area of Labrador. Half Dome retrieved from Wikimedia Commons, diabas intrusion retrieved from The Department of Natural Resources, Newfoundland and Labrador - Canada

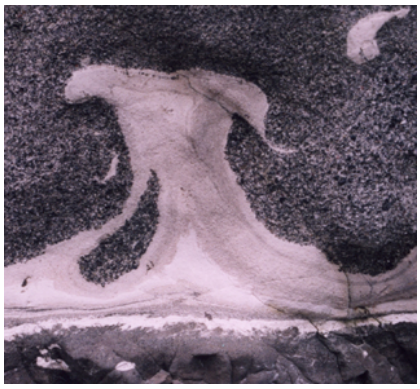

Figure 2.2: Silt diapir rising through a denser sedimentary layer at Boso Peninsula, Japan. Copyright Roberto Weinberg 2007, retrieved from users.monash.edu.au/ weinberg.

scales. This is further substantiated by studies of deformation fabrics in and around granite plutons, concluding that considerable ductile deformation of the host rock had taken place while the bulk of the intruding granite was essentially liquid containing suspended crystals[30].

2.1.1.2 Aspect ratios

Dykes are roughly planar intrusion sheets, with an aspect ratio between thickness and length normally ranging from 1:100 to 1:10000, while diapirs are more spherically shaped with aspect ratios generally between 1:1 and 1:10. The thickness of dykes or diameter of diapirs varies a great deal. Mafic dykes, e.g. dolerite, have reported average thicknesses ranging from centimeters to tens of meters to nearly one kilometer in dykes from the Proterozoic era. The mafic dykes are generally thinner and more extensive (more width) than their silisic counterparts, e.g. dolerite, relating to the viscosity increase with increasing silica content due to silica chains[33].

2.1.2 The crack tip process zone

Exposed dyke tips show an abundance of deformation features and metamorphism, and inelastic deformation is sometimes observed extending from centimeters to several meters from the dyke tips. At the margins of some granitic plutons observations indicate the initiation of viscous dykes, e.g. in Moore and Sisson (1987)[18] where a few fine-grained granodiorite dykes graded into pegmatite in the direction that the dyke narrowed[30]. Because pegmatite are derived from water-rich melts or perhaps even aqueous fluids, they have viscosities of magnitudes less than typical granites, meaning they can be influential in rapid dyke propagation in developing dykes. Such low-viscosity phases at the crack tip could inhibit both crack-tip blunting and magma freezing, mechanisms that have been used to reject the idea of a diapir-dyke hybrid[30].

The seismic monitoring of volcanism is often associated with “anomalous” earthquakes and earthquakes of magnitude 1 and greater seem to be ubiquitous features of dyke propagation [32]. This has been interpreted as a result from tensile fracturing associated with the hydraulic fracture processes of dykes. Such phenomenon has also been observed during laboratory experiments of hydraulic fracturing. The suggestion that it results from dyke propagation remains however controversial[32, 33]. Rubin and Gillard (1998)[32] concluded in their theoretical study of dyke-induced earthquakes that “...the distribution of (recorded) dyke-induced seismicity reflects the

distribution of ambient stresses that are near to failure and does not necessarily reflect the extent of the dyke.".

2.1.3 Intrusion propagation

2.1.3.1 Direction

A pure diapiric processes is thought to be vertical, while dykes propagate in the direction perpendicular to the least compressive stress or the dykes might invading existing cracks if the magma pressure exceed the ambient compression perpendicular to the crack. If the magma excess pressure is small compared to the ambient compressive stress then only the cracks nearly perpendicular to the compressive stress may be dilated, and if the magma pressure exceeds the greatest compressive stress cracks of any orientation can be dilated[33].

The independence of dyke propagation direction from the direction of gravity has been used to distinguish dyke ascent from from diapirism. Dykes can often be found in swarms extending tens to hundreds of kilometers, arranged in a linear or radial fashion[33]. Similar patterns can be observed in experiments, with a transitional regime in viscoelastic hydraulic fracturing[8, 15].

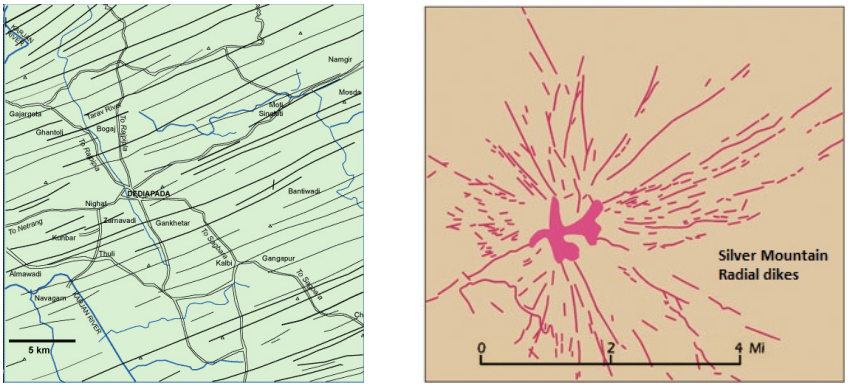

Figure 2.3: Simplified geological maps of linear and radial dyke swarms. To the left we see the Dediapada linear dyke swarm in the Narmada-Satpura region of the Deccan, retrieved from http://www.mantleplumes.org/Deccan.html. To the right are the radiating dykes of Silver Mountain, Colorado, from the Colorado Geological Survey http://geosurvey.state.co.us/.

2.1.3.2 Speed

Because of the extremely large effective viscosities of rock, rates of pure diapiric ascent are considered slow, perhaps on the order of several centimeters per year, while mantle-derived dyke intrusions are inferred from seismic measurements and numerical analysis to propagate at rates in the range 0.01 to $10\,\mathrm{m\,s^{-1}}$. Meter-wide doleritic shallow dykes below volcanoes in Hawaii and Iceland approach $1\,\mathrm{m\,s^{-1}}$, meaning even narrow width basaltic dykes can propagate great distances before freezing [30, 33].

2.1.3.3 Ascent

Magma ascent is commonly portrayed as a pulse of isolated batches. The theory around this pulsing is not entirely clear, but several ideas have been proposed. A common assumption is that the ascent velocity of an incipient dyke increases as more magma is pumped into the dyke resulting in a buoyancy increase to a point where the magma may accelerate upward, without significant additional input from the source. The dyke tail cannot be entirely extinguished because of the very large viscous resistance resulting from the thinning crack. The flow rate in the dyke varies proportional to the thickness squared. A new thick batch emerging from the source will therefore catch up with the thinner parts, resulting in a pulsing motion [33].

2.1.4 What can we learn from field observations?

The field studies of exhumed magma intrusions along with seismic and geodetic study leaves us with firsthand data on the process, the interpretation of such results may be subjective and purely descriptive, but the lessons learned are manifold. What I consider most relevant from the field work review is that:

- The mode of ascent and propagation for magma is not restricted to end-members like dykes, diapirs and porous flow. Hybrid behavior on a geological scale, and is substantiated by e.g. the overlapping range of aspect ratios found in what is considered dykes and diapirs.
- The timescale of loading increases with the viscosity, leaving viscosity contrast between host rock and intrusive magma the primary parameter for propagation and shape control.
- Considerable ductile deformation of host rock can also be observed when the viscosity ratio with the bulk of the intrusion should be high,

leaving hybrid behavior dependent on more parameters than viscosity contrast.

- Both dyke and diapir processes are observed to be scalable and similarities with other natural processes and experiments suggesting, experiments as a viable and valid approach.

- Inelastic deformation around shallow dykes in the brittle regimes suggest hybrid behavior can occur even close to the surface.

- Knowledge of what happens at the crack tip is essential for understanding the process of magma ascent and propagation.

2.2 Magma intrusion theory

To properly predict and describe magma intrusions through theoretical means one has to develop a broad insight into flow and fracture phenomena through continuum mechanics, especially the field of rheology, which concerns materials with both solid and fluid behavior. Only a superficial background study of some of the main focus areas has been done in this review.

2.2.1 Rheology of the Earth

Rheology is, in the most general way, the study of deformation and flow, but tends to be focusing on materials behaving in complex ways; non-linearity, time-dependence, creep, electro- and magnetorheology etc.

The main focus of rheology is to empirically establish the relationships between deformations and stresses, and analyze the meaning and implications of these relations, and to make use of their consequences.

Geodynamic processes operates with characteristic times ranging from a fraction of a second in seismic body waves, to hundreds of millions of years regarding the thermal history of the Earth. The length scale varies from 10^{-10} m (1 ångstrøm) - a typical value of lattice spacing - to 10^{6} m, the linear dimension of a mantle convection cell. Within this huge span, deformation and flow occurs at all scales. The common precondition to a satisfactory analysis of these geological processes is an understanding of the rheology of Earth materials and of its dependence on intrinsic and extrinsic parameters.

2.2.1.1 The transition zone

The rheology of the mantle and crust can be constrained from geophysical evidence e.g. postglacial isostatic rebound[26]. Deformation in the shallow crust is dominated by brittle processes, and the strength of rock will increase with overburden pressure. In large, shallow crust deformation will be independent of temperature and rock type. As depth increases further into the crust, the increasing temperature will promote viscous deformation. At around $10 - 15\,\text{km}$ we venture into the brittle-ductile transition zone, as depicted to the left in figure (2.4), where viscoelastic deformation is pervasive.

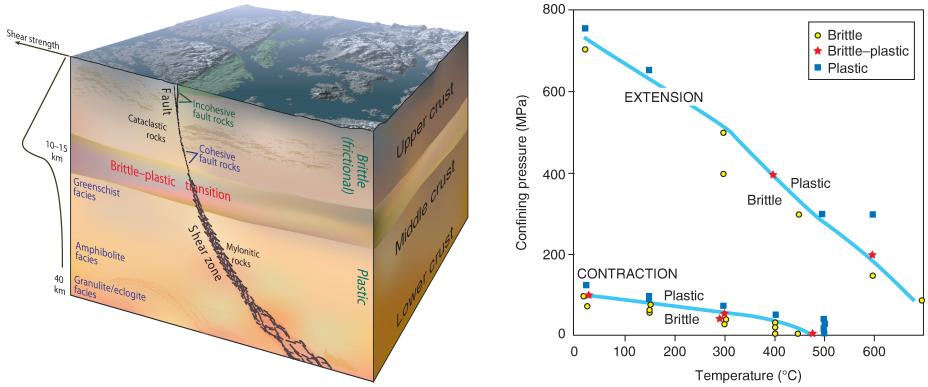

Figure 2.4: The brittle-ductile transition zone. From Fossen (2010) [5]

However, the mode of deformation is not only dependent on ambient pressure and temperature, but also the local stress field, as seen to the right in figure (2.4), timescale of loading and deformation history. The presence of a free fluid phase will tend to decrease the strength of the rock and promote diffusional creep, and for viscous deformation processes chemical constituents in the rock may have significant effects on the mechanical behavior[26]. The rheology concerning a highly dynamic process such as magma intrusions is therefore not easily contained.

2.2.1.2 Shear-thinning in magmas

Magmas are shown to display a viscosity dependency with the stress, often with a decrease of apparent viscosity, i.e. shear-thinning. The level of dependency is found variable and poorly constrained, and can be linked to the underlying mechanics of the shear-thinning. The origin itself is not quantitatively determined, however viscous heating, particle migration and crystal breakage are amongst the most likely sources. Characterization of

these sources is necessary to scale back the flow behavior in laboratory experiments to the natural scales [2].

2.2.2 Non-Newtonian fluids

The simplest fluid rheology is that of a Newtonian fluid, which can be described using Newton's law of viscosity:

$$\tau = \mu\dot{\gamma}.$$

The law states that the shear stress τ acting on a fluid body is linearly proportional to the shear rate $\dot{\gamma}$ and viscosity μ.

Newton's law of viscosity may be adequate for simple Newtonian fluids, however, a wide array of fluids exists with complex molecular structures leading to time and rate dependent properties. These liquids, known as non-Newtonian, have non-linear flow curves and their response to deformation and strain rate, elongation, and shearing can be categorized into classifications of time-independent, viscoelastic, and time-dependent behavior[9].

Figure 2.5 show typical shear stress to strain rate relations for various Newtonian and non-Newtonian fluids. As seen in the figure, shear-thickening fluids require an increasing amount of stress as strain rates increase leading to a concave curve, their apparent viscosity increases with increased stress, while a majority of non-Newtonian fluids, the shear-thinning fluids act in an opposite manner in which the rate of stress increase will decrease with the strain rate applied, that is, the apparent viscosity decreases with increased stress. In Bingham fluids, or yield-stress fluids, a yield stress must be overcome within the fluid before any strain is induced. In this case, the fluid acts as an elastic solid below a critically applied stress but begins to flow once the yield stress is overcome[9].

The viscosity of time-independent non-Newtonian liquids is often described using the power law model which relates the response of viscosity as a function of shear rate,

$$\tau = K\dot{\gamma}^n.$$

where K is the flow consistency coefficient, and n is the power law index[9]. Typical velocity profiles for power-law fluids in a laminar non-turbulent pipe flow are shown in figure 2.6.

For a certain class of fluids the apparent viscosity continues to change as a function of the time for which the particular shear rate is applied. These are the time dependent non-Newtonian fluids. Fluids which become more shear-thickening with time, or in other words the apparent viscosity

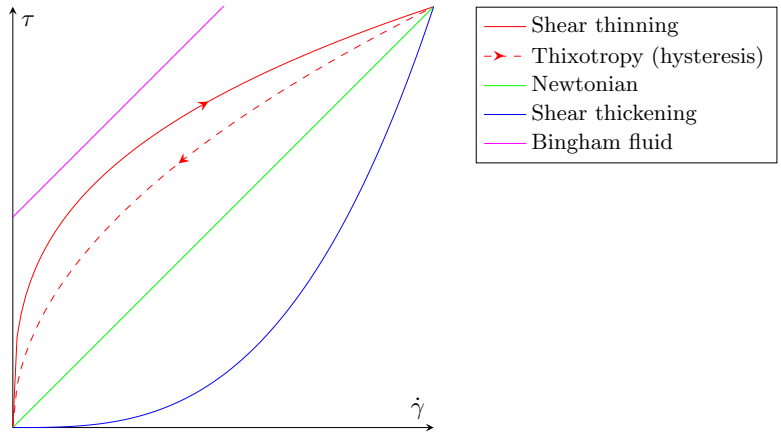

Figure 2.5: Illustrative plot of shear stress τ as function of strain rate $\dot{\gamma}$ for Newtonian and non-Newtonian fluids, see legend. Adapted from Holland (1973) [9]

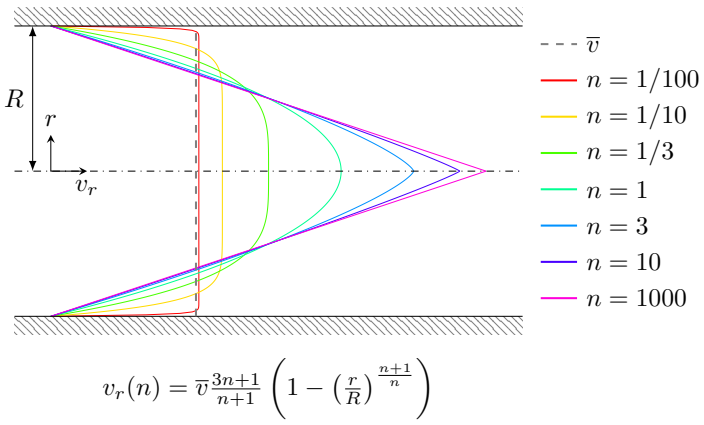

Figure 2.6: Plot of velocity profiles for power-law fluids in a pipe of radius R. Assuming laminar non-turbulent flow, the velocity v_r (colored lines) is plotted as a function of distance to the centerline r, for different power-law coefficients n. Newtonian fluids have $n = 1$, shear-thinning fluids have $n < 1$, and shear-thickening fluids have $n > 1$. The mean flow velocity $\overline{v}$ (gray, dashed) is plotted for comparison. Adapted from Holland (1973) [9]

increases with duration of stress, are called rheopectic. Fluids which become more shear-thinning with time, or in other words the apparent viscosity decreases with duration of stress, are called thixotropic. Their structure progressively breaks down with time at a constant shear rate. Thixotropy is a reversible process, and eventually a dynamic equilibrium is reached were the rate of structural breakdown is balanced by the simultaneous rate of reformation. Most thixotropic fluids will recover their original viscosity if allowed to settle for a sufficient time[9]. An example of this hysteresis is shown in figure 2.5.

2.2.3 Rheological models

2.2.3.1 General linear model

Simplifications of the problem are readily available. Using mechanical model analogues, a linear approximation neglecting transient phenomena results in a Maxwell viscoelastic body for the upper mantle. To upgrade the model, a transient response can be introduced by adding a Kelvin element, making it a Burgers body, the simplest linear model to account for elastic, transient and steady-state deformation[26]. Such a model can be used to model the host rock response in a magma intrusion. However, the Burgers model, figure (2.7), is only a first approximation to the problem with only one relaxation time [26].

2.2.4 Hydraulic fracturing

The fracture dynamics of dykes are often associated with hydraulic fracturing [30, 33], i.e. fracturing of rock with a fluid with higher pressure than ambient stress. Other fracture mechanisms, not concerning the fluid magma phase, also play a role in the fracture of host rock in the proximity of an intrusion, however hydraulic fracturing is what drives the magma to propagate and what we focus on in this literature review.

To produce a hydraulic fracture the fluid pressure in the crack must be sufficiently larger than the ambient effective stress so that the minimum principal stress becomes tensile and overcomes the tensile strength of the host rock. The confining pressures of rock deep in the crust work against tension fractures in particular because of the need to separate the cracks walls. The need for minimum principal stress in order for a hydraulic fracture to initiate is used to infer the stress history of a host rock with such fractures[5]. However, since hydraulic fractures also can propagate in existing cracks such analysis can be ambiguous.

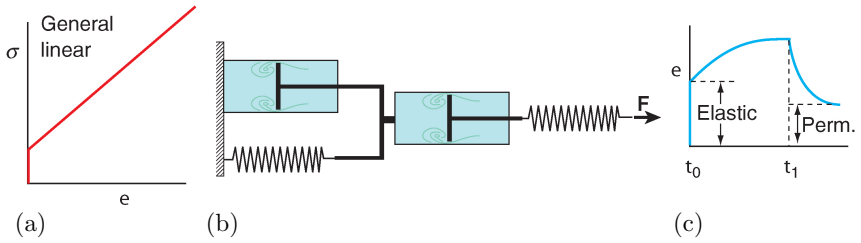

Figure 2.7: Illustration of the mechanical analogue of the Burgers general linear model (b). Perfect elastic deformation is represented by a spring, while a perfect viscous deformation is represented by a dashpot. The general linear stress-strain relation shows an initial elastic strain response and additional viscous strain after yield stress is reached (a). The strain history curve for a constant stress above yield illustrates the instant elastic strain when subjected to stress at $t = t_0$ followed by the time-dependent viscous strain. When stress is removed at $t = t_1$, the elastic strain in the Maxwell element is instantly recovered while the Kelvin element exhibits gradually recovery in elastic afterworking. The viscous stress of the Maxwell element is permanent. The strain and recovery rates are controlled by the viscosities. Figure from Fossen (2010)[5].

The displacement field of a fracture is usually classified into three different modes in the field of fracture mechanics:

Mode I - opening or extension mode, tensile stress perpendicular to the crack plane.

Mode II - sliding mode, shear stress parallel to the crack plane and perpendicular to the crack front.

Mode III - tearing mode, shear stress parallel to both crack plane and front.

Illustrations of the different modes are shown in figure (2.8).

The hydraulic fracture analogue in linear elastic fracture mechanics is mode I fracture, where a tensile stress normal to the crack plane enables crack propagation. If we assume the crack front to be parallel to the z-axis, figure (2.8) depicts the profile of the crack tip. If we consider a homogeneous, linear elastic material, the Cauchy stresses in the vicinity of the crack tip has the form:

$$\sigma_{ij}(r,\theta) = \frac{K}{2\pi r} f_{ij}(\theta),$$

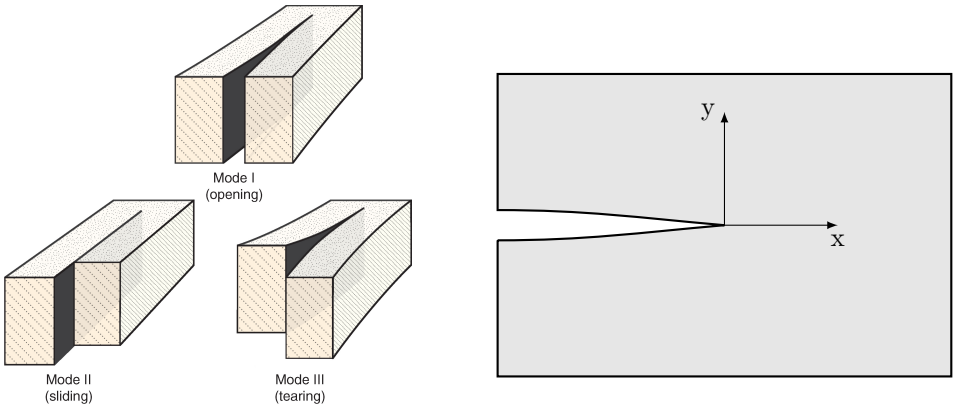

Figure 2.8: To the left: Fracture modes and their displacements. From Fossen (2010)[5]. To the right: the profile of a mode I crack.

where K is the stress intensity factor and r is the distance from the crack tip, θ is the angle with respect to the plane of the crack, fij is a dimensionless quantity that is universal in the sense that it does not depend on the length of the crack or the details of the applied load, but depends on the angle with respect to the crack and on the material properties[5, 20].

2.2.5 Viscous fingering

As we in this thesis are especially interested in the viscous and viscoelastic modes of magma transport, we must do an in-depth study of the viscous analogue to fracturing, the so called viscous fingering. We start with shortly describing the most common setup for studying viscous fingering, before we delve into the theory.

2.2.5.1 The Hele-Shaw cell

In 1898 Hele-Shaw introduced a simple system to study water flow around various geometries [7]. The system, a Hele-Shaw cell, consisted of two parallel transparent plates separated by a gap, small relative to the plate dimensions. Fluids were injected into the cell at varying pressures and the transparency of the cell allowed direct observation and documentation via photography. The Hele-Shaw concept was favorable analytically because the reduction to two dimensions allowed for considerable simplifications in the constitutive equations of flow [17]. The Hele-Shaw geometry is illustrated in figure (2.9).

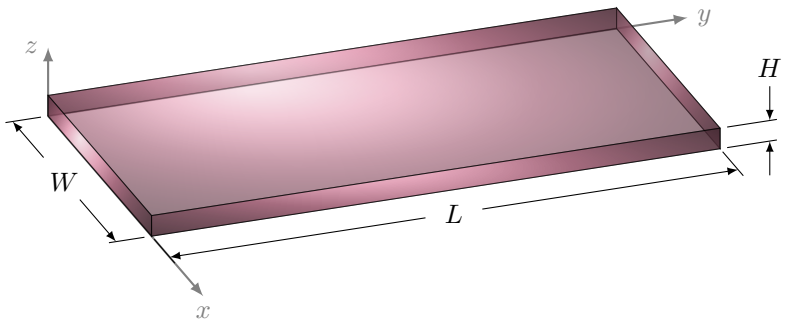

Figure 2.9: Hele-Shaw geometry. The gap, H, is smaller than the dimensions in the plane, W and L, to allow a reduction to two dimensions when studying flow within the geometry.

2.2.5.2 Saffman-Taylor fingering

The Hele-Shaw setup was later modified by Saffman and Taylor [35] to address the phenomenon of interfacial motion between two immiscible viscous fluids. In the classical Saffman-Taylor experiment a viscous fluid confined in the narrow channel of a Hele-Shaw cell is pushed upon by a less viscous one resulting in a finger-like pattern, like the one shown in figure (2.10).

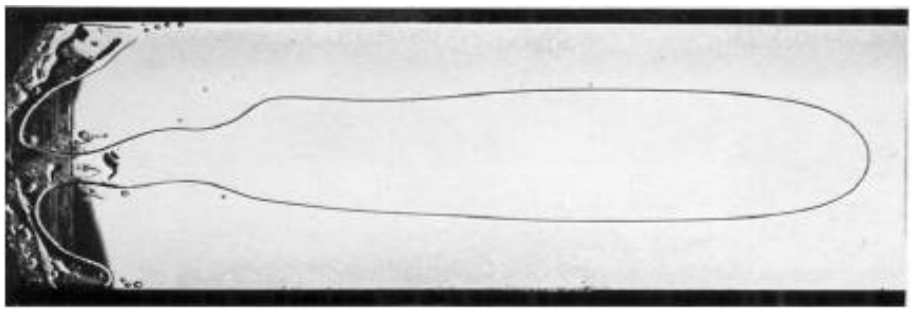

Figure 2.10: Saffman-Taylor fingering. An air finger advancing into glycerine from the experiments of Saffman and Taylor[35].

The discoveries of Saffman and Taylor has served as a reference in viscous intrusion experiments in two dimensions, and the problem is well studied and documented. The most common geometries used in such experiments are the linear and radial Hele-Shaw cell as shown in figure (2.11).

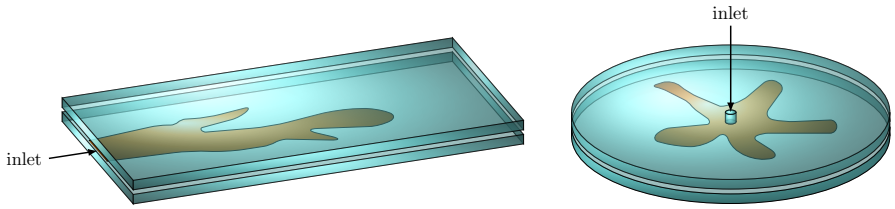

Figure 2.11: Linear and radial Hele-Shaw cell

The following summary of the Saffman-Taylor instability is a paraphrasing of "Viscoelastic surface instabilities" by Lindner and Wagner (2009)[17] supported by additional resources where cited.

The classical Saffman-Taylor instability in a Hele-Shaw cell can be described completely mathematically using air as the less viscous fluid. We assume Newtonian steady state viscous flow, neglecting the viscosity of air and assuming that the viscous liquid perfectly wets the channel. The main flow in the Hele-Shaw cell is governed by Darcy's law which reduces far away from the fingers to:

$$U_\infty = -\frac{H^2}{12\eta}|\nabla p|,$$

which says that the mean velocity of the fluid in the far field U_∞, averaged over the thickness of the channel H, is a function of the applied pressure gradient ∇p and the viscosity of the fluid η. In a gravity field the buoyancy from density difference is included in the pressure gradient. If the fluid is incompressible the divergence of the flow is zero, $\nabla \cdot \vec{U}_\infty = 0$, immediately resulting in a Laplacian pressure field, $\nabla^2 = 0$. The surface tension between the air and the viscous fluid, $\sigma_{\alpha\beta}$, results in a pressure jump at the air-fluid interface given by the Laplace-Young boundary conditions:

$$\Delta p = p_{air} - p_{fluid} = \sigma_{\alpha\beta}(\frac{2}{H} + \kappa),$$

where κ is the mean curvature in the direction of the channel width, still considering a two-dimensional approximation. Thus, taking boundary conditions into account, we can describe the problem completely.

When the less viscous fluid pushes on the more viscous fluid, an initially straight interface becomes unstable. The instability causes small perturbations on the interface leading to increased pressure gradients and thus higher velocity in front of the perturbations, amplifying the perturbations.

On the contrary, the capillary forces of the surface tension seeks to stabilize the straight interface, competing with the viscous forces arising from the fluid pressure. Using linear stability analysis on the system results in a characteristic wavelength of the perturbations. The maximum growth rate is found for the most unstable wavelength:

$$\lambda_c = \frac{\pi H}{\sqrt{\mathrm{Ca}}},$$

where Ca, is the capillary number or ratio between viscous and capillary forces. The capillary number is given by:

$$\mathrm{Ca} = \frac{\mu U_f}{\sigma_{\alpha\beta}},$$

where U_f is the finger tip velocity. Low capillary numbers describes flows dominated by capillarity, whereas for high capillary numbers the capillary forces are negligible compared to the viscous forces. In other words an increase in Ca corresponds to an increased flow velocity or a lowering of surface tension. The growth rate as a function of the wavenumber $k = 2\pi/\lambda$ is showed in graph (a1) of figure (2.12) and an illustration of the critical wavelength in inset(a2).

Perturbations that are favored by the characteristic wavelength begin to grow into small fingers. As they advance the fingers compete and the less advanced fingers are eventually screened and overtaked by the more advanced fingers. In a linear Hele-Shaw cell, finally a single finger like the one in figure (2.10) is left to propagate by itself through the cell. An example of the initial finger growth and finger competition, together with the growth rate obtained from the linear stability analysis, can be seen in subfigure (b) in figure (2.12).

For Newtonian fluids, the finger width w can be determined by the capillary number. In addition the finger width limited by the cell width W for very large values of Ca. The capillary forces tend to widen the fingers whereas viscous forces tends to narrow them, so that the width decreases with increasing finger velocity[1]. The finger width does not diminish completely but converges to a limiting value of about half the cell width or $\lambda_f = 1/2$. Lindner and Wagner finds the relative finger width λ_f, or the ratio of the finger width to the cell width, $\lambda_f = w/W$, to be a function of the dimensionless control parameter $1/B$:

$$\frac{1}{B} = 12 \left(\frac{W}{H}\right)^2 \mathrm{Ca},$$

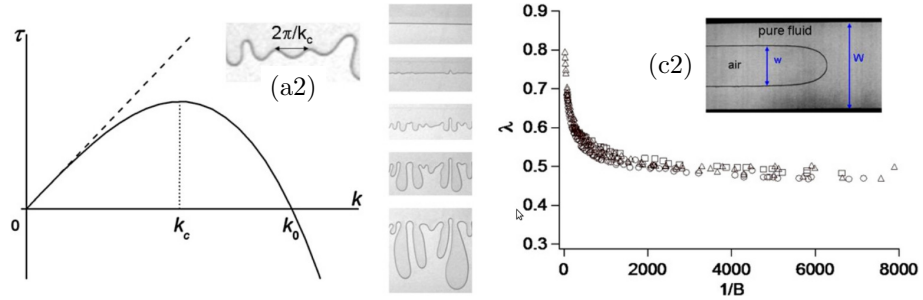

Figure 2.12: To the left (a1) shows the growth rate τ as a function of the wave number k, the most unstable wavelength is derived by linear stability analysis to be $2\pi/kc$ described in the inset (a2). In the center (b) we see snapshots of the destabilization of a planar front (at the top) between air and silicon oil evolving in to a finger-like pattern (bottom) (D. Derks and A. Lindner). To the right (c1) the relative finger width $\lambda_f = w/W$ is shown as a function of the dimensionless control parameter $1/B$ for air pushing silicon oils of different viscosities in channels of different geometries, the widths are pointed out in inset (c2), a snapshot of a finger advancing into a linear cell (C. Chevalier). Figure and explanation adapted from Lindner and Wagner[17]

involving the cell aspect ratio and the capillary number. As an example the relationship for air pushing silicon oils is plotted in the graph (c1) in figure (2.12), showing that different surface tensions, viscosities and geometries complies with an universal curve.

If the displacing fluid were to completely expel the more viscous fluid from the gap between the plates there would be a relationship

$$U_\infty = \lambda_f U_f,$$

describing the relation between the main flow velocity and the finger tip velocity. In general this is not so since a fraction m of the more viscous fluid is left adhering to the plates, so that we get the relationship

$$U_\infty = (1 - \overline{m})\lambda_f U_f,$$

where $\overline{m}$ is the average value of m around the boundary of the finger [36].

In radial cell Saffman-Taylor experiments the characteristic wavelength is even more evident in the finger-pattern. The initial interface is the radial case a circular blob, if the interface becomes unstable again, like in the linear

cell, fingers start to grow. As the radius increases with finger propagation, the finger tips themselves becomes unstable resulting in splitting of the tips when approaching characteristic wavelengths of the perturbations on the tips.

2.2.5.3 Saffman-Taylor fingering in shear-thinning fluids

In addition to Newtonian fluid instabilities in Hele-Shaw cells, non-Newtonian fluids has been investigated by several researchers. Whereas in Newtonian fluids in Hele-Shaw cell, viscous fingering leads to the growth of smooth fingers, non-Newtonian fluids has an inherent shear-dependent and or time-dependent anisotropy giving room for other patterns.

In shear-thinning fluids at high velocities fingers are found to be significantly narrower than the classical limit of $\lambda_f = 1/2$, sometimes even fracture-like. This is a result of the viscosity anisotropy emerging from the viscous flow in shear-thinning fluids. In other words, regions with high shear rate, e.g. the crack tip, have a lower viscosity allowing for preferential flow at the tip, and the base or fjord of the finger pattern has a high viscosity resulting in slow or no flow[17].

For weak shear-thinning fluids, shear-dependence in the range $1 > n > 0.65$, simply replacing the constant viscosity by a averaged shear-dependent viscosity allows rescaling onto the universal curve obtained for Newtonian fluids. For strong shear-thinning fluids, $n < 0.65$, the rescaling fails and deviates from the classical results[17]. The shear-thinning also drastically decrease the wavelength of maximal growth thus increasing branching and the fingering pattern for strong shear-thinning fluids resembles patterns that are formed as a function of anisotropy in the system, e.g. dendritic growth.

Kondic et al. (1998)[14] proposed a phase diagram, shown in figure (2.13), for shear-thinning fluids based on a non-Newtonian power law numerical model with viscosity given as a function of the flow velocity V and shear dependence n:

$$\mu = V^n$$

The phase diagram is scaled based on the dimensionless Weissenberg number We and the capillary number. The Weissenberg number is the ratio of the relaxation time of the fluid and a specific process time, e.g. in simple steady shear it is defined as the shear rate $\dot{\varepsilon}$ times the relaxation time t_r[42]:

$$\mathrm{We} = \dot{\varepsilon}\tau_r$$

An increased Weissenberg number corresponds to an increasing shear-thinning effect.

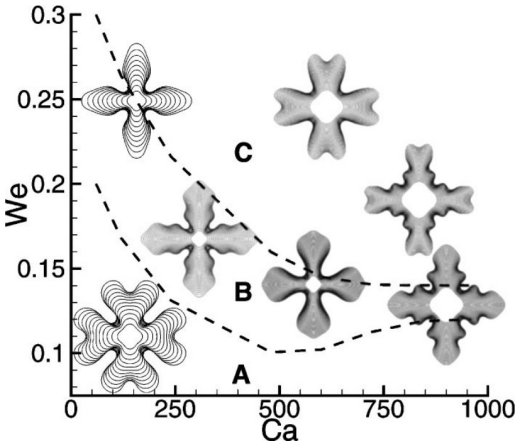

Figure 2.13: Phase diagram for radial pattern formation in a strongly shear-thinning fluid, $n = 0.15$, for small values of We$<$0.25. In regime A one gets wide Newtonian-like petals, in B tip-splitting is suppressed, and in C narrow fingers relative to A, but tip-splitting petals are observed. An increase in We corresponds to an increased shear-thinning, while an increase in Ca could be due to a higher flow velocity or lower surface tension. Figure and explanation from Kondic et al. (1998)[14].

The phase diagram shows three regimes with distinct patterns. The regime borders seem asymptotical. For very low Weissenberg and capillary numbers the pattern is similar to the ones attained for Newtonian fluids. With increased numbers there is an intermediate regime where finger tip splitting is inhibited and the fingers are narrow. For even more increasing numbers, reflecting high velocity flows, or low surface tension, and high shear rates the fingers are even thinner, and splitting occurs. For higher capillary numbers the fingering increases. The relaxation time also plays an important role. As the fluid relaxation time decreases, the ability of the fluid to resist tip splitting increases[14].

The effect of shear thinning rheology on tip splitting can be seen by comparing Newtonian and shear-thinning injection simulations as seen in figure (2.14). In the simulations from Fast et al. (2001)[4] the Newtonian fluid exhibits the expected finger growth and tip-splitting, whereas in the shear-thinning fluid tip-splitting is inhibited at first and branching occurs behind the tip at a later stage in the intrusion. Fast et al. hypothesises this as an effect of the difference in viscosities at the crack tip compared to the viscosity at the base, or fjord, of the fingers. The higher velocity at the tip induces shearing which in-turn decreases the fluid viscosity, allowing for preferential flow at the tip. In a Newtonian fluid on the other hand the

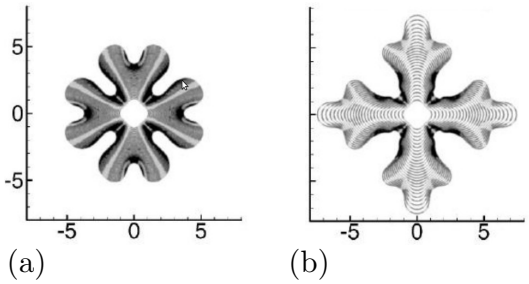

Figure 2.14: Comparison of fingering for Newtonian (a) and shear-thinning fluid (b) injections into a radial Hele-Shaw geometry. The fluid flows has the same capillary number. Figure from the numerical work of Fast et al. (2001)[4].

viscosity is constant.

2.2.6 Rheological modelling of magma

"Dikes vs. diapirs in viscoelastic rock" by Rubin[30] (1993) is one of the first studies that really address viscoelastic behavior in magma migration. The paper investigates the influence of viscosity contrast on magma transport by examining a pressurized dyke propagating in a linear viscoelastic medium. Using the Maxwell solid as model for the host rock and treating magma flow within the dyke as Poiseulle flow, he finds essentially elastic host rock response during intrusion of basalt and low viscosity rhyolite dykes, but viscous deformation exceeding the elastic deformation during high viscosity rhyolite intrusion of hot rock. This intrusion model depending upon viscosity contrast can help explain occurrences of dykes with aspect ratios lower than 10^{-2}, but higher aspect ratio intrusions like equidimensional granite plutons cannot be attributed solely to the viscosity contrast.

Rubin's model is effective in its simplicity, however the composition of rock in earths crust is rheologically vastly more complex than a Maxwell solid. The choice of excess magma pressure as primary driving force, as opposed to a combination of buoyancy and pressure, substitutes a clearly directional net force with forces distributed equally in every direction. The model assumes existing seed cracks, neglects fracture resistance, is unable to address the complexity of the crack-tip process zone and several other simplifications are done. These assumptions are well justified by the author "...on the grounds that at this point any simple analytic results should aid in our understanding of the processes involved". Similar theoretical

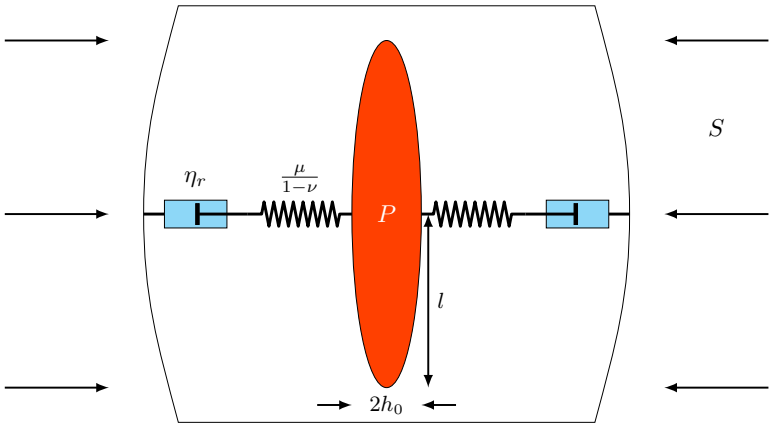

Figure 2.15: Theoretical model of a stationary dyke in host rock. The dyke is modeled as a viscous fluid, while the host rock is modeled as a Maxwell linear viscoelastic body.

work on viscoelastic intrusion models has been done, yet the viscoelastic model is only developed as a hypothesis, and there is no experimental data connecting the theoretical work with observations.

Another aspect of Rubin's model is how the magma itself is modeled. The intruding magma is simplified as a viscous fluid when it in fact displays viscoelasticity, albeit with lower viscosity and less elastic response than the host rock [30].

Rubin found that dyke or diapir growth is governed by primarily two parameters; the elastic response of the host rock, and the viscosity contrast between the intruding magma and the host rock. Considering expected ratios of the excess magma pressure at the dyke entrance to the elastic stiffness of the host rock, the host rock has to have a viscosity contrast of 11 to 14 orders of magnitude to the magma to behave as essential elastic during dyke intrusion.

2.2.7 What does theory and simulations tell us?

Theories and simulations explore the mechanisms behind the processes, they are not only descriptive but also predictive. However, analytical and numerical models are based on simplifications of the natural process, e.g. for magma intrusion simple, and often linear, rheological models are used, while the rheology of Earth, and hybrid magma intrusions in particular, is very complex. Thus, in some cases theory and simulations are limited to fit ideal

end-members of the processes, leaving them indicative instead of predictive. Nevertheless, theory and simulations form the analytical framework from which we develop our experimental methods and interpret our experimental results.

The literature on magma intrusion theory is not well sorted and lacking of consistency, with a few honorable exceptions, e.g. Rubin's work through several articles[30, 32, 33]. Therefore we see the need to support our literature review on magma intrusion theory with analogue theory from physics and fracture mechanics. The key points found from theory and simulations are:

- Magma rheology is complex and poorly constrained, displaying both viscoelasticity and shear-thinning behavior.
- Intrusion morphology and intruded matrix rheological response is dependent on both intrusion and matrix rheology. The two governing parameters are, according to Rubin, the elastic response of the host rock and the magma to host rock viscosity contrast.
- The simplest analogue mechanics of magma intrusions' viscous and elastic end-members are found in viscous fingering and hydraulic fracturing, respectively.
- According to literature on viscous fingering and hydraulic fracturing, the rheological and morphological responses in intrusion processes are also strongly dependent on often neglected parameters such as e.g. interfacial tension.
- The many unknown or poorly constrained parameters of magma and host-rock rheologies make scaling to laboratory studies difficult.

2.3 Intrusions in the laboratory

There have been several attempts to simulate magma intrusions under controlled conditions using models analoguous to the natural intrusion system. An analogue model is a simplified representation of the system under study. To select the setup and materials for an analogue experiment, one should scale the laboratory model to the natural geological process according to the similarity criteria established in "Theory of scale models as applied to the study of geologic structures" by Hubbert[10] in 1937. The model must be geometrically, kinematically, dynamically and rheologically similar to the process to be considered a proper scale model. Analog models

commonly use granular materials to simulate frictional Mohr–Coulomb plasticity and various viscous and viscoelastic fluids to simulate ductile creep [3]. The main challenge in scaling intrusion experiments lies in the lack of certainty regarding the physical and rheological constraints of the natural process. However, at this point, any new insight to the dynamics of viscous intrusion into a viscoelastic media will help understanding the magma intrusion processes.

2.3.1 Radial viscoelastic fracturing

While the Saffman-Taylor fingering, or viscous fingering, is an entirely viscous phenomena, magma intrusion is more complex as it deals with both viscous and elastic deformation. "From viscous fingering to viscoelastic fracturing in colloidal fluids" by Lemaire et al. (1991)[15] and Hirata's "Fracturing due to fluid intrusion into viscoelastic materials" (1998)[8] are two examples going one step further using the Hele-Shaw geometry studying the interfacial patterns of fluid intrusions into viscoelastic bodies.

2.3.1.1 "From viscous fingering to viscoelastic fracturing in colloidal fluids", Lemaire et al. (1991)

Lemaire et al. performs three sets of experiments, which of only two are considered here. In the first set they use a radial Hele-Shaw cell made of two square glass plates with side $L = 0.45\,\mathrm{m}$ separated by a gap $H = 0.3\,\mathrm{mm}$. The thickness of glass plates are 12 mm so one can assume low-deformability under the injection pressures used. The geometry is filled with a colloidal dispersion of smectite clay in water, varying the viscoelastic properties by adjusting the mass fraction of clay. As the intruding fluids they use water (viscosity $\mu = 0.89\,\mathrm{mPa\,s}$ at $298\,\mathrm{K}$) and the slightly more viscous dodecane ($\mu = 1.35\,\mathrm{mPa\,s}$). The interfacial tension between water and the clay suspension is vanishing, whereas it is large in the case of dodecane ($0.051\,\mathrm{N\,m^{-1}}$). The fluids are injected at constant flow rate through a 1 mm hole at the center of the bottom plate.

A representative set of results from the experiment are shown in figure (2.16. For low flow rate and low clay concentration one can observe typical viscous fracturing patterns, the tip profile is rounded and branching occurs at the finger tips at angles less than 90°. For higher flow rates and higher clay concentration the resulting pattern is closer to elastic fracturing. The tips are acute and the branching occurs behind the crack tip at straight angles, the cracks are generally curved and branching occurs systematically

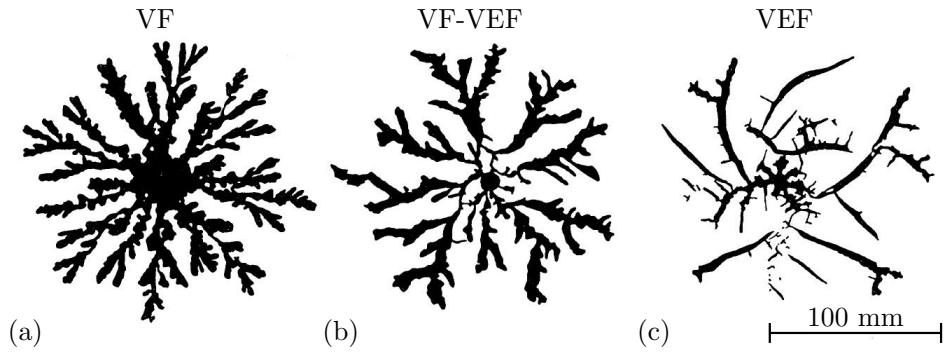

Figure 2.16: Patterns obtained by injecting water into a radial Hele-Shaw cell filled with a colloidal dispersion of smectite clay in water, with increasing clay to water ratio from left to right. Subfigure (a), the results from a clay/water ratio of 0.08, displays a viscous fingering (VF) pattern, subfigure (b), clay/water ratio 0.10, is identified as a crossover regime between viscous fingering and viscoelastic fracturing (VEF), and subfigure (c), clay/water ratio 0.20 is identified as a viscoelastic fracturing pattern. Figure from the experiments of Lemaire et al.[15].

on the convex side of the main crack, indicatinf that the branching is a result of tensile stress parallel to the growth direction of the main cracks.

Lemaire et al. plotted the local curvature along the fluid/clay interface as seen in figure (2.17). The curvature plot shows that the viscous finger pattern have large radii convex, curvatures at the tips, that is the tips are blunted, and that the clay fjords between the fluid fingers and cracks are sharp with a convex curvature. When the elastic effects come too play in the viscoelastic regime, the fjords tend to disappear or widen, and the amplitude of the convex curvatures at the tip increases, i.e. the tip sharpens. Far into the viscoelastic regime, the elastic effects become even more appearent, with large domains of vanishing curvature at the increasingly longer crack walls and narrow spots of very large convex curvature at the crack tips.

The large morphological differences allows classifications into deformation categories, according to Lemaire et al., without ambiguity. The deformation phase diagram is depicted in figure (2.18).

In rheology the Deborah number is often used to describe the fluidity of a material. The Deborah number is the ratio between the time it takes for the material to adjust to applied stresses, the relaxation time (t_r), and the characteristic timescale of a flow event in the material, t_{fl}:

$$\mathrm{De} = \frac{t_r}{t_{fl}}.$$

Figure 2.17: Local curvature along the fluid/clay interface corresponding to the patterns shown in figure (2.16). As seen in the legend to the right positive (upwards) values corresponds to convex curvature, representing tips of fingers or cracks, while negative values corresponds to a concave curvature, representing the clay fjords between the fluid fingers and cracks. Figure from Lemaire et al.[15] with added annotations.

If the relaxation time is much shorter than the timescale of the flow event, the material response fluid-like dominated by Newtonian viscous flow, and, vice versa, if the relaxation time is higher than the timescale of the flow event, the material enters the non-Newtonian regime responding more elastic and solid-like as. Essentially the smaller the Deborah number, the more fluid it is, the greater the Deborah number, the more solid it is[28]. Viscoelastic materials are characterised by at least one internal relaxation time and for colloidal suspensions the relaxation time is related to the structural reorganizations and Brownian motion of the colloidal particles in the suspension fluid[15].

The roughly hyperbolic crossover between the viscous and viscoelastic regimes in the phase diagram agrees with the idea that the crossover happens at a critical Deborah number[15]. When the timescale of the flow event t_fl, expected to vary like the reciprocal of the flow rate Q, $t_{fl} \propto 1/Q$, exceeds the frequency of structural reorganizations in the clay t_r, expected to be proportional to the reciprocal of the clay to water ratio,

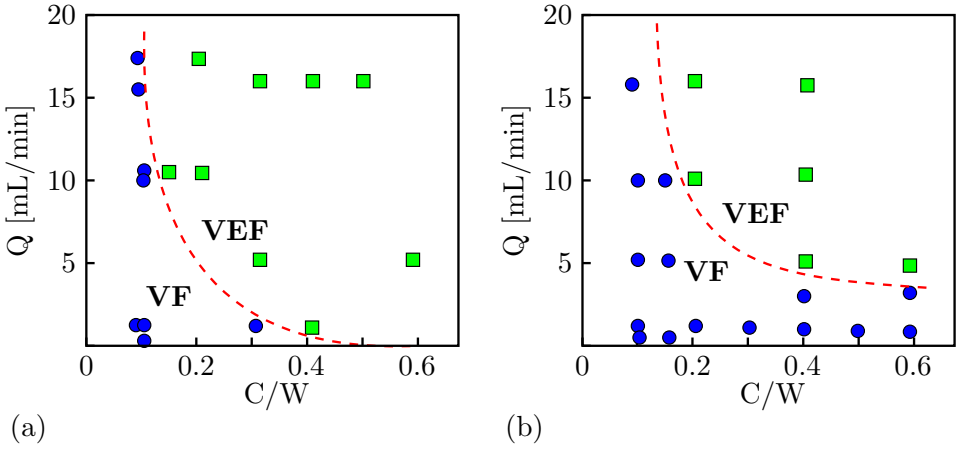

Figure 2.18: Pattern phase diagram showing the relation between injection flow rate and clay/water mass fraction, and the emerging intrusion pattern. In (a) water is the intrusion fluid, while it is dodecane in (b). The blue circles shows the relation for patterns identified as viscous fingering and the green spheres represents the viscoelastic fracturing regime. The dashed red line shows the assumed crossover between the regimes. Based on similar figure from Lemaire et al.[15].

$1/t_r \propto 1/(C/W) \rightarrow t_r \propto C/W$, we get the resulting relation

$$\mathrm{De} = \frac{t_r}{t_{fl}} \propto \frac{C/W}{1/Q} \Rightarrow Q_{crit} \propto \frac{1}{C/W}, \tag{2.1}$$

which yields an equilateral hyperbola and the conclusion that the stronger the suspension, the smaller flow rate is necessary to exceed the the structural rearrangement rate. To support this statement, Lemaire et al. also used video records to estimate the timescale of the flow events in the transition between the viscous and the viscoelastic regime. The average finger or crack width l, and the average crack tip velocity U, was measured and used to calculate the flow timescale

$$t_{fl} = \frac{1}{Q} = \frac{l}{U}.$$

Transition occured at $t_{fl} = 0.2\,\mathrm{s}$ for $C/W = 0.2$, and at $t_{fl} = 0.3\,\mathrm{s}$ for $C/W = 0.3$, which both are consistent with equation 2.1

Lemaire et al. observes that the interfacial tension in the intruding fluids increases crack width. The change in geometry causes a lower stress

intensity at the crack tip compared to what would be the case for no surface tension and as we can see in figure (2.18) the phase boundary for the dodecane experiments is shifted, giving a larger viscous regime than water.

The mass fractal dimension, D_m, is also measured using a box counting method, resulting in values close to that of diffusion-limited-aggregation-type patterns, ($D_m \approx 1.68$), for the viscous fingering pattern, but systematically giving lower mass fractal dimension for viscoelastic fracturing patterns, $D_m \approx 1.6$ down to 1.4 ± 0.05. Interfacial tension does not seem to interfere with mass fractal dimension.

In the second set Lemaire et al. study the effect of varying the cell deformability by varying the thickness of the glass plates between 4 and 24 mm, keeping the clay concentration and flow rate fixed. The resulting patterns in figure (2.19) show a clear dependence on the plate thickness and also induces transition from flow to fracture. Lemaire et al. assumes that

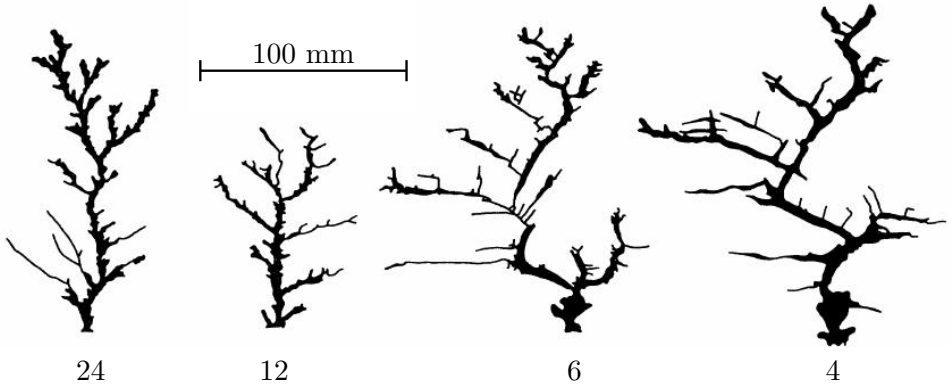

Figure 2.19: Pattern obtained with constant paste concentration (C/W = 0.1) and injection rate (Q = 10 mL/min) by using Hele-Shaw cells with varying plate thickness, from left to right decreasing thickness in mm resulting in viscous fracturing for thick plates to viscoelastic fracturing for small plate thickness. Only one of the the main branches of the pattern is represented. Figure and explanation from Lemaire et al.[15].

the critical factor for crack opening is when elastic energy stored as cell deformation exceeds the energy needed to overcome the yield stress in the clay. Using pressure in a the intruding fluid, P, as a measure of potential energy, E_p, per unit volume, V, through the definition of work, W, gives

the following relation:

$$P = \frac{F}{A} = \frac{F \cdot L}{A \cdot L} = \frac{W}{V} = \frac{E_p}{V} \Rightarrow E_p = PV,$$

where A is an arbitrary area and L a unit length. In other words the stored elastic energy as a function of cell deformation is of the order $P\Delta V$. Equating this to a simplified Griffith's criterion fitting viscoelastic fracture, neglecting kinetic and cohesive energies with respect to energy dissipation, gives us an approximation of the critical pressure needed for crack opening. The critical pressure at which fracturing will be initiated, P_{VEF}, is found to follow the formula:

$$P_{\text{VEF}} \approx C \left(\frac{e}{L}\right)^2, \quad C = \left(\frac{\tau_y a E^2}{\epsilon^2 L}\right)^{\frac{1}{3}} \tag{2.2}$$

where e is the plate thickness, L the length of the plate, τ_y the clay yield stress, a the cell gap height, E the elastic modulus of the glass, and ϵL is the radius on which the pressure is applied ($\epsilon \ll 1$). In other words the critical pressure is found to be proportional to the square of the plate thickness.

Thus, one would expect the critical pressure to be smaller than the fluid pressure for thin plates, inducing viscoelastic fracture patterns, and higher than the fluid pressure for thick plates, resulting in viscous fingering. This conclusion matches the observed patterns in figure (2.19).

2.3.1.2 "Fracturing due to fluid intrusion into viscoelastic materials", Hirata (1998)

The experiments of Hirata are similar to those of Lemaire et al., however complementing in many aspects. The Hele-Shaw cell is radial, consisting of a square Pyrex-glass plate and an acrylic acid resin vessel with sides $L = 0.30\,\text{m}$ and a gap $H = 0.3\,\text{mm}$. Viscoelastic materials are primarily categorized into two categories according to their flow behavior, fluid or solid, and Hirata makes a point out of using a Kelvin viscoelastic solid as the fracturing medium, unlike Lemaire et al., who used a clay suspension considered to be a Maxwell viscoelastic fluid. The Kelvin solid used is an agar gel, and the viscoelastic properties are varied by adjusting the mass fraction of agar to water. The intruding fluid is the air (viscosity $\mu = 1.82 \times 10^{-5}\,\text{Pa s}$ at $290\,\text{K}$).

Fluid intrusion into viscoelastic materials often occur under a constant pressure, and not under a constant intrusion flow[33]. Therefore Hirata injects the air at a constant pressure through a $2.5\,\text{mm}$ injection hole in the upper plate. Pressure control and measurement is accurate to $\pm 0.01\,\text{kPa}$,

and no fluctuation of injection pressure is observed during pattern growth. To capture the dynamical processes of the pattern growth a video camera with a framerate of 30 frames per second was utilised.

Rheological tests on the agar concluded in lower concentration agar, of mass fraction $C_w = 0.05 - 0.15\,\%$, being considered viscous fluid, and at $C_w = 0.20\,\%$ and above the assumption of agar behaving as a viscous fluid becomes invalid. It is also apparent by the patterns resulting from the experiments, figure 2.20, that agar mass fraction at $C_w = 0.2 - 0.3\,\%$ show the properties of a viscoelastic body, while a lower mass fraction of $C_w = 0.1\,\%$ behaves as an essentially viscous fluid.

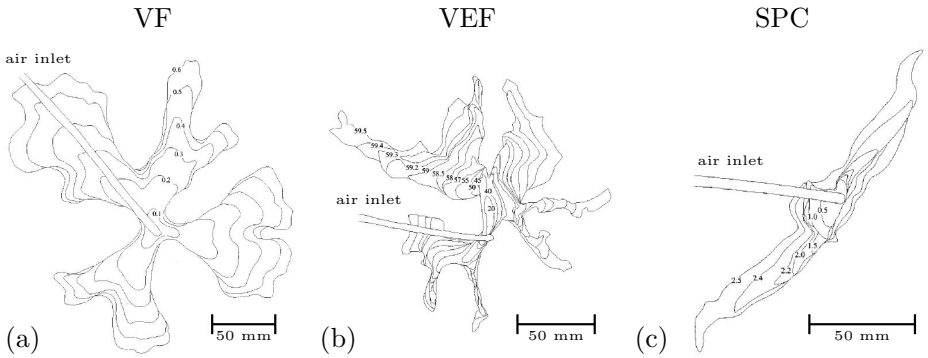

Figure 2.20: Evolutions of patterns observed by air injection into Hele-Shaw cell filled with agar gels. From Hirata[8].

The characterization of the three growth patterns as observed by Hirata is shown in table 2.1. A phase diagram showing the relation between the growth patterns and the independent variables, agar concentration and air injection pressure, is shown in figure 2.21.

Pattern	Branching	Tip geometry
SPC	No	Acute
VEF	Yes	Acute
VF	Yes	Round

Table 2.1: Characterization of three growth patterns. Hirata[8].

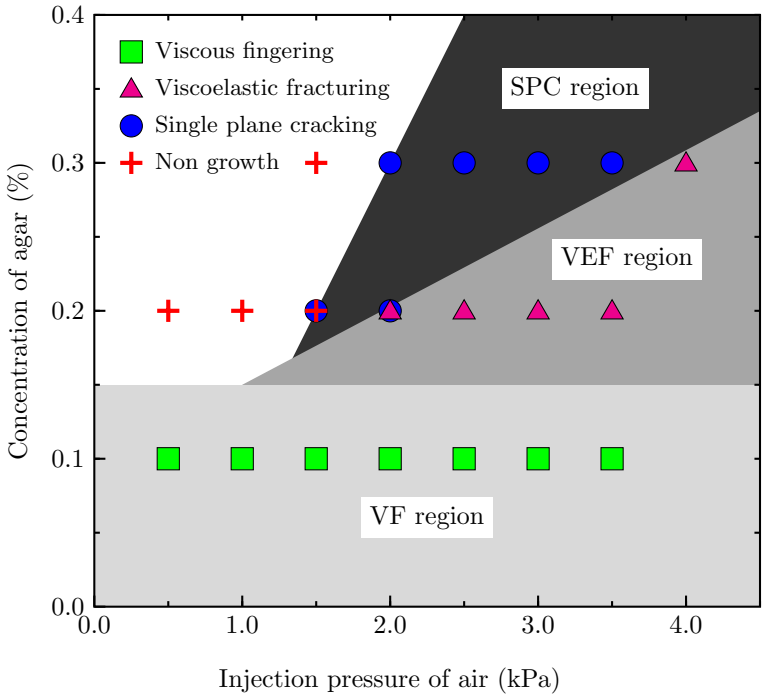

Figure 2.21: Phase diagram for pattern formation by fluid injection. Both the pressure of air injection and the concentration of agar are experimental parameters. Hirata[8].

2.3.2 What can we learn from experiments?

The advantages of experiments are their physical results and the opportunity for systematical parameter study. The main challenge is scaling intrusion experiments since there is uncertainty regarding the physical and rheological constraints of the natural process. Few truly viscoelastic intrusion experiments have been performed, and they are phenomenological and qualitative in form. The experiments presented above tell us that:

- Transition from tip splitting in the viscous regime to branching in the elastic regime is indicative of the deformation category.
- The local curvature of the intrusion to matrix interface is indicative of the deformation category.
- The large morphological differences between viscous fingering, viscoelastic fracturing, and elastic fracturing allows classifications into

deformation categories.

- Changing the injection fluid viscosity and interfacial tension with the matrix greatly affects the resulting intrusion morphology.
- Cell geometries and deformability affects the rheological response.

2.4 What is missing?

From what we have learned in our literature study we see that research on the dynamics and mechanics of magma intrusions is restricted to theoretical work based on field observations and reological models, or qualitative analysis of laboratory experiments that do not scale well with the natural problem. We argue that focus on the following research topics are required for advance in the field:

- Magma and host rock combined rheometric parameter study.
- Proper scaling of magma intrusions to laboratory scale models.
- Quantitative stress-strain analysis on these models.

Ideally on would start on the top of this list and work one's way to the bottom, however as we stated in the beginning of this review: magma intrusions happen subsurface and are impossible to observe directly and unintrusively. Considering that the characteristic time and length scales of such processes ranges from fractions of seconds to millions of years, and from one ångstrøm to hundreds of thousands meter, makes characterization of rheological properties a difficult task indeed.

We suggest starting in the laboratory with developing analogue experiments on magma intrusions. If we can use a quantitative stress-strain analysis in such an experiment to obtain constitutive relations of materials of complex rheologies, similar to the assumed magma and host rock rheology, then we should be able to put further constraints on the natural problem through reversed scaling.

A concept viable to achieve such a feature is the use of so called optical rheometry in combine with the more known particle image velocimetry. Similar combined setups have been used with success in the studies of stagnation flows in polymer melts [39].

The use of optical methods to study the dynamics and structure of complex materials subject to external fields has a long history, ranging back to the discovery of the photoelastic phenomenon by the Scottish physicist

David Brewster in 1816. With the advent of computers, the traditional areas of optical rheometry have been partly replaced by modern numerical techniques. However in recent decades, with the rapid expansion of soft solids for commercial use, such optical techniques have been revitalized as a viable technique[25]. Optical rheometric techniques have the advantage of being non-intrusive and provide a whole field stress-strain analysis. They are particularly useful for studying complicated geometries and loading conditions, or materials with non-trivial behavior, where analytical and numerical methods may be cumbersome or inaccurate[6].

The optical rheometric studies are concerned with the link between microstructural behavior under loading and their optical response[6]. We want to strengthen the concept by adding particle image velocimetry to provide us with macroscopical deformation and flow fields.

Chapter 3

Materials and method

The methodology of our experiments is presented below starting with a concept walkthrough, following up with the prototype experimental setup, a material description including rheometry measurements, and lastly, a step-by-step work-flow.

3.1 Concept

We assume that magma intrusion into Earth's crust is a problem of viscous intrusion into a viscoelastic medium, and define our main objective as observable, if not quantifiable, stress and strain during such an intrusion. We propose to achieve this with polariscopy of a scale model of the magma intrusion, supported by particle image velocimetry.

The concept setup, visualized in figure 3.1, consists of a Hele-Chaw cell filled with a viscoelastic host-rock analog, that is placed between polarizer sheets forming a make-shift polariscope. Viscous fluid, posing as magma, is injected into the viscoelastic medium, deforming it through fracture and flow. Choosing a matrix material that is optically isotropic when unstressed, but anisotropic when subjected to stress facilitates observation of birefringence induced by stress, strain and flow; i.e. the birefringence should be proportionate to the stress field. If the matrix in addition is seeded with particles, velocimetry will provide the macroscopic strain field.

3.2 Experiment setup

The experiment setup was simple in form and use, and low cost. I constructed it myself, mostly using scavenged parts from discarded

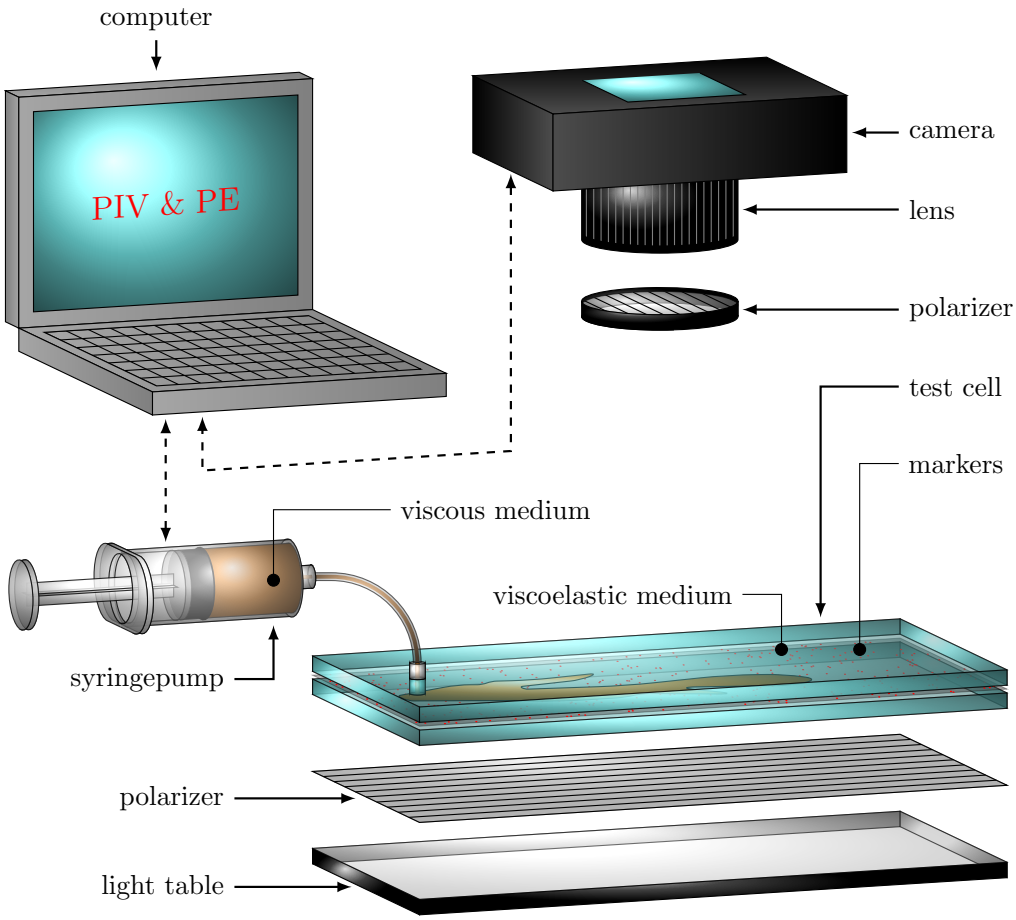

Figure 3.1: Conceptual experimental setup. A Hele-Shaw test cell filled with a viscoelastic medium is intruded by a viscous medium. The deformation of the viscoelastic medium manifests itself through a hybrid of fracture and flow, while stress induced birefringence, marker particle movement and interfacial movement is monitored and logged via camera and crossed polarizers. Intrusion flow rate is controlled using a syringe pump or similar. In the sketch a linear cell with inlet at the short side of the top plate is shown. This is just an example of cell and inlet geometry — the concept is valid for any Hele-Shaw type cell.

Table 3.1: Aspect ratios, $\epsilon = H/W$, for the Hele-Shaw cells, H is the gap height and W the width of the cell. All geometries had a length L of approximately 400 mm.

H [mm]	W [mm]	$\epsilon = H/W$
1.3	100	0.013
1.3	50	0.026
2.1	71	0.030

experimental equipment, but despite its simplicity, it provided the function that was demanded from the concept.

3.2.1 Cell

The linear Hele-Shaw cells used in the experiments, seen in figure 3.2, consisted of two rectangular 5 mm soda-lime glass sheets separated by a frame with a rectangular cutout in different aspect ratios. The separator frame was made of either 2.1 mm aluminum sheets with a soft rubber gasket at the inner edge to prevent leakage, or 1.3 mm acrylic sheets with silicone grease functioning as a seal. The different cell geometries defined by the separator frame are listed in table 3.1

The top glass plate had holes of 4 mm diameter drilled in the short ends so that the hole was approximately centered in respect to the 3 closest edges of the separator frame. In each hole a Luer-Lok one-way stopcock was attached with silicone glue. The stopcocks were closed during gel aging to provide a closed atmosphere. The whole cell was clamped together with screw clamps covering the long ends of the glass sheets.

3.2.2 Optics

The optical setup, as seen in figure 3.3, was fairly simple. The cell was illuminated with a white light source composing two 36 W 4000 K fluorescent lamps, using aluminum foil as reflector and frosted glass to diffuse the light. The light source was cooled with a ventilator fan to prevent temperature change. A linear polarizer sheet of unknown origin and specifications was used to polarize the light before entering the experiment cell. The camera was a Nikon D300 fitted with a Nikkor 24-85 mm f/3.5-4.5 G AF-S Ø67 mm lens, and a Schneider optics B+W MRC 67 mm circular polarizer functioning as the analyzer part of the make-shift polariscope. The whole setup was enclosed in a box which was painted in matte black to prevent light pollution from other sources than the white light source.

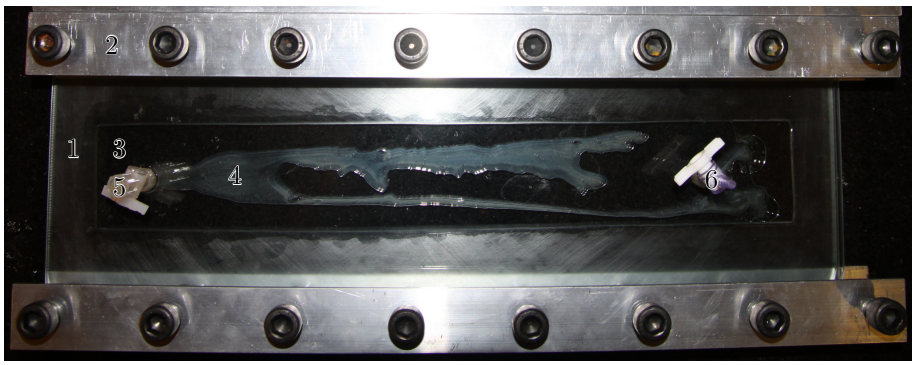

Figure 3.2: The experiment cell consisted of two glass sheets separated by a frame (1) with rectangular cutout of various aspect ratios, which was clamped together by screw clamps (2). Inside the gel matrix (3), one can see the shape of a fully developed oil intrusion (4). The inlet (5) and outlet (6) of the cell had stopcocks attached to provide a closed atmosphere.

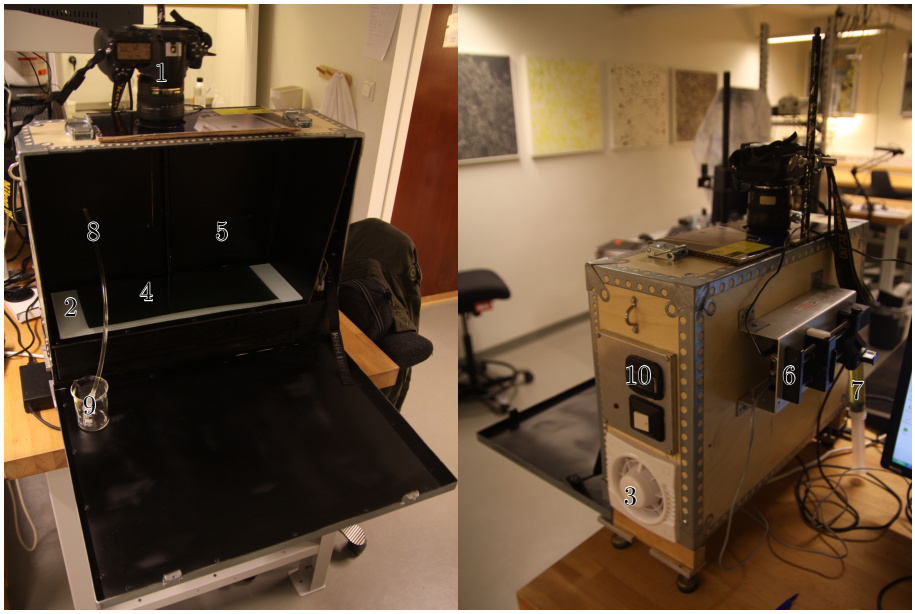

Figure 3.3: Photos of the experiment setup showing the optical arrangement together with flow control parts. The optical setup consisted of: a camera (1) with a circular polarizer filter, a white light source (2) cooled with a ventilator fan (3), a linear polarizer sheet (4), and a box enclosing the experiment (5). The flow control setup consisted of a syringe pump (6) with a oil-filled syringe (7) attached; connected to the cell through a rubber hose (8) with a stopcock at the end (9). The temperature is probed using a digital thermometer (10) with the sensor placed inside the box.

The camera was originally controlled through a computer interface, but it was found to capture faster at high resolution when using the continuous capture function provided on the camera itself.

Different camera settings were tested during the experiments and adjusted to fit the experiment purpose; listed here are the final settings:

- The focal length was set to 35 mm as the selected lens had the least spherical aberration at this setting, adjusting the field of view accordingly by distancing the camera.
- The thin geometry of the experiment cell allowed for a narrow depth of field so the aperture was set to the widest possible at $f/4.0$.
- An ISO sensitivity at 800 was selected as a higher setting seemed to produce too much noise, and finally the shutter speed was set at 1/60 s, which resulted in acceptable contrast, but was too slow to avoid blurring of fast moving features.
- The spatial resolution of the camera was set to the highest possible, 4288x2848 pixels, to capture the details of the deformation, but the resulting capture rate limitation at 1 frame per second gave poor temporal resolution in respect to the experiment flow rates.

3.2.3 Flow control

The flow control setup, presented in figure 3.3, consisted of a NE-500 Programmable OEM Syringe Pump from New Era Pump Systems, Inc., and the syringe pump was controlled using the SyringePumpPro software from the same company. An oil-filled BD-60 syringe with Luer-Lok tip was attached to the pump, and connected to a length of stiff rubber hosing of 2 mm inner and 5 mm outer diameter. At the end of the hose a Luer-Lok one-way stopcock was attached for easy closing of the oil containing parts.

3.3 Materials

In this section we first present a short reasoning of our material selection, before giving a detailed overview of the viscoelastic matrix material. The material, laponite, is traditionally regarded as unpredictable of nature, and care must be taken to control its rheology. A detailed laponite sample preparation protocol is also included. Last in this section, basic rheometry measurements are presented.

3.3.1 Material selection

A promising candidate for model systems depicting the complex dynamic processes of the Earth are clays. Their small particle sizes and micro-porous structure give them the ability to absorb variable amounts of water, becoming hydrated clays, or to be dispersed in water and form colloidal dispersions. This makes possible a remarkable diversity of phases and facilitates a wide range of rheological behavior in fracture or flow experiments. Natural clays are abundant and inexpensive, but are mostly highly heterogeneous mixtures of minerals and are normally unsuitable for reproducible results. However, pure clays can be made synthetically; e.g. laponite, which is what we have selected as our viscoelastic matrix.

The viscosity ratio of magma to host rock is reportedly an important factor (e.g. [30]) for the resulting mechanism and morphology of a magma intrusion feature. To pose as our magma, we have therefore chosen two fluids of different viscosities, namely olive oil and water, which are cheap and readily available. Oil and water have simple Newtonian rheologies, which does not scale well with the complex rheologies of magma, but the first step to creating a simple solution is starting with simpler problems.

3.3.2 Laponite

Laponite, produced by Rockwood Additives Ltd, is a synthetic smectite clay which, suspended in water, can take on a diversity of rheologies from the pure elastic to the pure viscous. It is widely used as a liquid rheology modifier in household and industrial products, such as makeup and paint, and has lately gathered great interest for scientific pursuits. Despite its high purity there has been great controversy and diskussion regarding reproducibility of laponite samples and how the laponite rheology phase diagram looks [34]. However, according to several recent studies, e.g. Kaushal and Joshi (2014) [13] and Ruzicka and Zaccarelli (2011) [34], this incoherence stems from laponite sensitivity to sample preparation procedures, and the fact that low concentration laponite suspensions are subject to a delayed healing process; i.e. an aging process. Ruzicka and Zaccarelli claim that, if aging and sample preparation are considered, a unifying picture emerges from different experimental studies.

3.3.2.1 Chemical structure

The structure of Laponite closely resembles that of hectorite, a natural clay mineral. It is a layered hydrous magnesium silicate and classified as

a (2:1) phyllosilicate. Octahedrally coordinated magnesium oxide sheets are sandwiched between two parallel sheets of tetrahedrally coordinated silica, making a tetrahedrally-octahedrally-tetrahedrally-structure (a TOT-structure), as shown in figure (3.4).

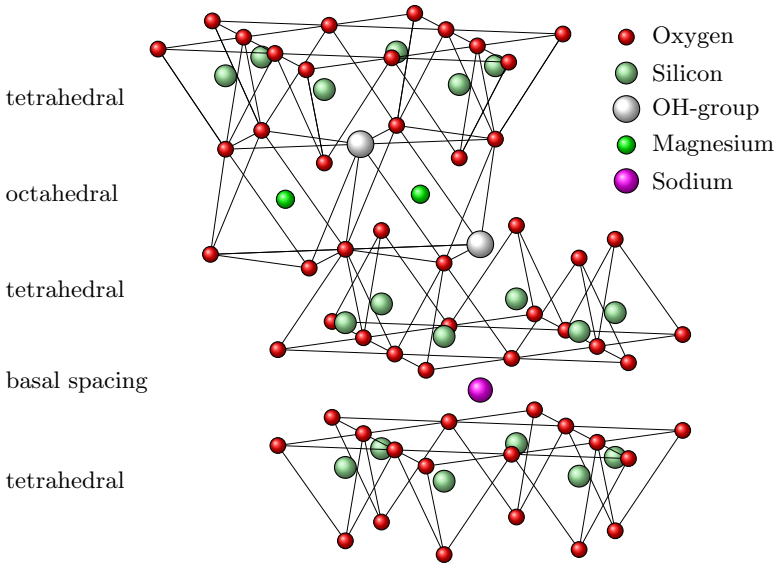

Figure 3.4: Laponite structure. Octahedrally coordinated magnesium oxide sheets are sandwiched between two parallel sheets of tetrahedrally coordinated silica making a tetrahedrally-octahedrally-tetrahedrally-structure, a TOT-structure. The negative net charge TOT-sheets are bonded together with sodium cations. Figure adapted from Ruzicka and Zaccarelli [34].

Laponite's elementary particles have small anisotropy compared to natural clay materials and form disk-shaped crystals with 1:25 aspect ratio on the nanometer scale. The particles are charged with a net negative charge on the faces and net positive charge on the rim (see figure 3.5).

3.3.2.2 Dispersion in water

Laponite in its gel forming grades disperse readily in water under agitation at room temperature. As illustrated in figure (3.6), the dispersion happens over several stages:

- Stage 1: laponite powder is added to water under agitation and wetting of aggregated particle stacks starts.

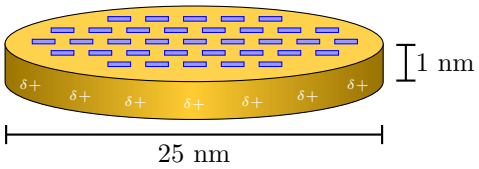

Figure 3.5: The primary particle of laponite illustrating the negative charges in the plane and the positive charges on the rim. Adapted from Rockwood Additives [29].

- Stage 2: The wetted particle stacks disperse into individual particle stacks.
- Stage 3: Hydration of the sodium ions forming the ionic binding of the laponite platelets begins a swelling between the primary particles composing the stacks.
- Stage 4: The swelling cause the primary particles to separate, the dispersion is complete and a sol-state has formed.

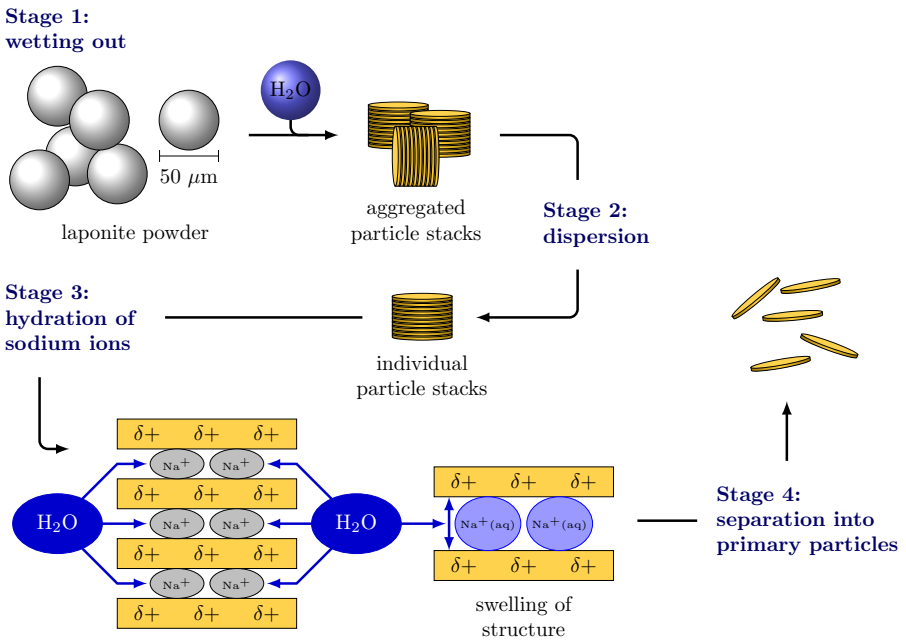

Figure 3.6: Diagram of laponite dispersion stages adapted from Rockwood Additives [29].

Stages 1 and 3 are time-dependent, while stages 2 and 4 are shear-dependent. Rapid agitation and extended mixing time is therefore needed to form a clear, colorless solution. With slow agitation and short mixing time larger partially hydrated laponite particles will form. The partially hydrated particles may form a gel coating, making the particles hard to redisperse [29].

Laponite gel is formed by ionic bonds and its rheology is as such largely unaffected by temperature. However, the rate of hydration of laponite is highly temperature-dependent. Below 10 °C hydration times will increase significantly and at temperatures above 35 °C the hydration time is so rapid that gel coated clumps of powder can form. The temperature dependence of hydration can be used to speed up the mixing process if one disperse laponite in room temperature and let it wet out completely before raising the temperature to increase hydration of the individual particle stacks [29].

3.3.2.3 Structural phases

When dispersion is done and the laponite sol is set to rest, the individual particles starts bonding and rearranging, forming a gel network. T-bonding, figure 3.7(a), where the rim positive charges connect with the plane negative charges so that one disk is perpendicular on the other, or parallel, partially overlapped (PPO) bonding, figure 3.7(b), are the prevalent bonding types forming laponite network structures.

(a) T-bonding (b) PPO-bonding

Figure 3.7: Laponite bonding types; T-bonding (a) and parallel, partially overlapped bonding, or PPO-bonding (b).

The chosen network structure is highly dependent on the concentration and the ionic strength of the laponite solution, and various glass and gels states can be formed by varying these parameters [34]. Figure (3.8) show test tubes with laponite samples of different concentrations and sketches of corresponding structural arrangement.

For solutions with low concentrations $C_{wt} < 1\,\%$ a separation into a sol and a gel state is observed some time after mixing. At concentrations

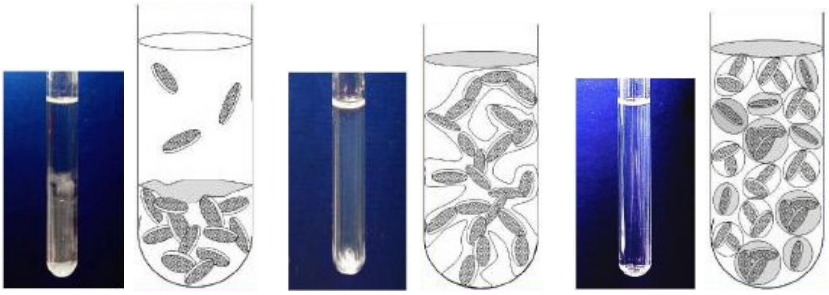

(a) $C = 0.3\,\%$ (b) $C = 1.5\,\%$ (c) $C = 3.0\,\%$

Figure 3.8: Laponite samples with corresponding structures for different clay concentrations and no added salt. From Ruzicka and Zaccarelli (2011) [34].

$1 < C_{wt} < 2\,\%$ true equilibrium gels are formed, while at $2 < C_{wt} < 3\,\%$ a wigner glass state emerge [34].

Above $3\,\%$ laponite starts showing birefringence under a polariscope. This is caused by transition from an isotropic state at lower concentrations, to a so-called nematic phase where the laponite disks form structures with long-range alignment order, making the laponite optically anisotropic. Laponite is not observed to enter a smectic phase [34].

The concept of isotropic, nematic and smectic states is illustrated in figure (3.9). An isotropic phase has no long-range order, nematic phases self-align to have long-range directional order as mentioned above, while smectic phases are ordered in alignment and position. While the example describes the ordering for rod-like molecules, the concept is similar for disk-shaped molecules like laponite platelets.

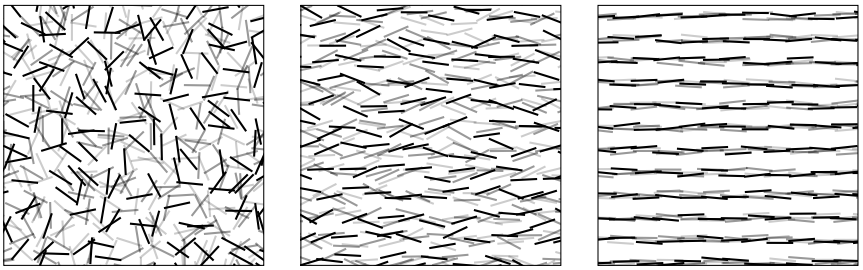

Figure 3.9: The microscopic structure of the isotropic, nematic and smectic state for rod-like molecules

Ruzicka and Zaccarelli (2011) [34] gathered the results from several

studies to produce the laponite structural phase diagram shown in figure (3.10). The phase diagram illustrates the wide range of structural forms laponite can take on.

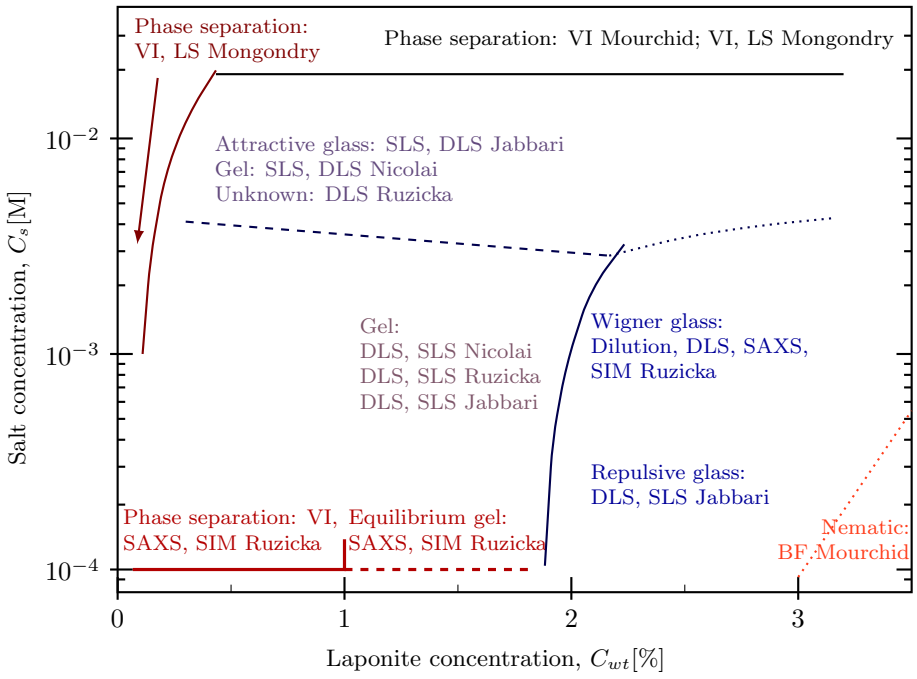

Figure 3.10: Laponite structural phase diagram as a function of clay and salt concentration. From Ruzicka and Zaccarelli (2011) [34].

3.3.2.4 Aging

To reach stable or metastable phases, laponite needs time to form a bond network as stated in earlier sections. The waiting time, t_w, needed for laponite to reach a transition from its fluid phase to an arrested state is shown in figure (3.11). The samples from figure (3.8) corresponds to the three main regimes in this diagram.

After an arrested glassy state is reached, rearranging and bond-making is inhibited by a so-called cage effect: particles are trapped by their nearest neighbors and cannot relax to their underlying equilibrium state. However, Brownian motion allows for structural reorganizations affecting the rheology over time, so reaching an arrested state does not mean that aging effect in laponite has stopped. The rate of the structural reorganizations is related to the internal relaxation time in colloidal fluids.

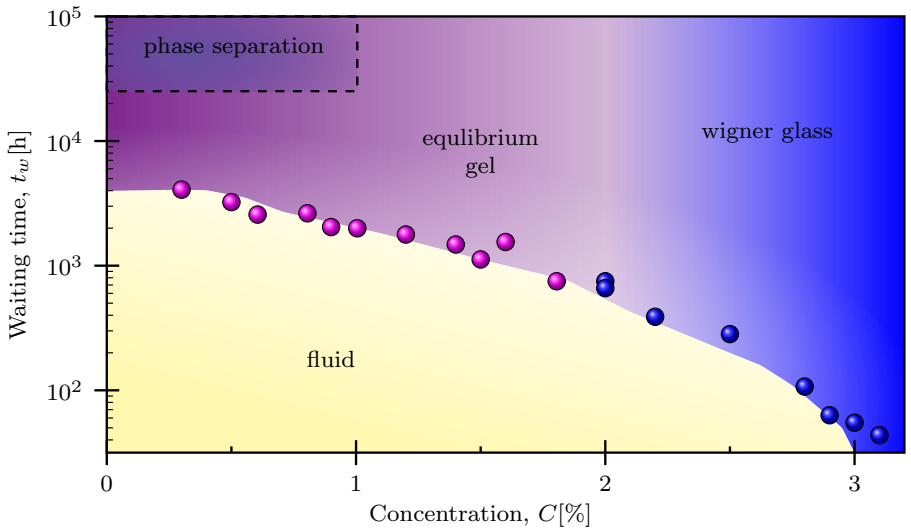

Figure 3.11: Laponite structural phase transition diagram showing transition times from liquid to arrested state as a function of laponite concentration. No salt was added in the solutions. Figure adapted from Ruzicka and Zaccarelli [34]

3.3.2.5 Rheology

The rheological behavior of laponite is versatile, ranging from the highly viscous to the near perfect elastic. In addition it is strongly thixotropic, and one of the most shear-thinning commonly used rheological additives [29]. The rheological behavior depends on concentration, ionic strength, and aging time, and thus deformation history.

A proper classification of laponite rheology has been attempted several times. The time dependency has been hard to determine and the material was not found to obey fundamental principles of linear viscoelasticity. The results have been inconclusive, among other reasons, because the researchers have used different laponite sample preparation protocols.

In a recent study, Kaushal and Joshi (2014) [13], used a novel interpretation of the viscoelastic framework and were able to fit their constitutive equations to experimental results. Their results are summarized for a 3.5 % laponite solution in figure (3.12) and they conclude that laponite rheology is in fact predictable.

3.3.2.6 Refractive index

Laponite gel has a refractive index close to that of water. Based on the works of Ravi Kumar et al. (2008) [27] the laponite refractive index is

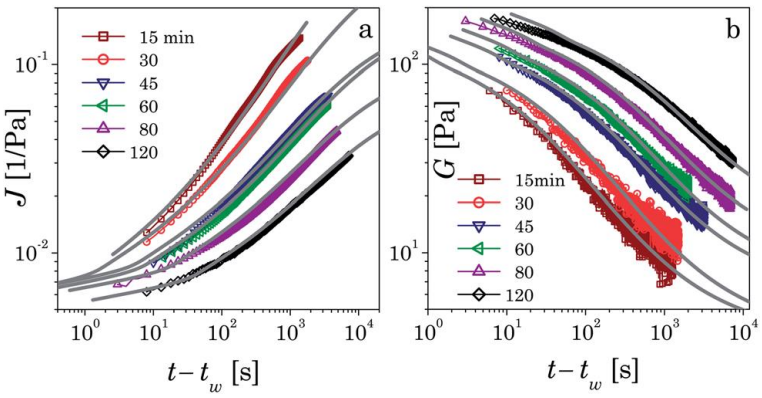

Figure 3.12: The creep compliance (J), left (a), and relaxation modulus (G), right (b), for a laponite concentration $C = 3.5\,\%$. The experimental data (colors) are plotted as a function of time elapsed (t) since application of step stress and step strain respectively, at different waiting times (t_w). The gray solid lines in (a) are the predictions of compliance obtained from the stress relaxation modulus shown in (b), while the gray solid lines in (b) are the predictions of the relaxation obtained from compliance data shown in (a). From Kaushal and Joshi (2014) [13].

dependent on concentration and temperature, while aging and filtration seem to have little effect. Disregarding any difference in sample preparation, they are found to be $n_{C=3.0\%} = 1.3355$ and $n_{C=3.5\%} = 1.3360$ at a temperature of $20\,^\circ$°C, for the respective concentrations used in our experiments [27].

3.3.2.7 Sample protocol

Finding a good approach to sample preparation is one of the most important steps to obtain accurate and reproducible results. As mentioned, laponite is sensitive to many external factors, and several studies have been rendered inconclusive or irreproducible by underestimating the significance of sample preparation and handling [34].

Our sample preparation protocol was developed based on recommendations from Rockwood Additives [29] and "A fresh look at the Laponite phase diagram" by Ruzicka and Zaccarelli. The protocol was continuously revised between experiments and modified according to our needs. The following protocol is the last revision:

- First *and* last step: all experiment parts were cleaned in a workmanlike manner.

- When dry, the parts were put together into their experiment assembly.
- Deionized water was poured into a glass beaker and control weighed.
- Based on to the water weight and desired laponite concentration, laponite powder was weighed on weighing paper.
- The water was put to a vigorous stir, powerful enough to create a stable vortex.
- Laponite powder was sifted gradually into the vortex, in a period of 2 min).
- Laponite powder residue on weighing paper was weighed.
- The beaker was sealed using Parafilm.
- 30 min fixed mixing time was initiated.
- After mixing time had passed, the sample was degassed for 2 min.
- The sample was transferred to the Hele-Shaw cell using a syringe. The cell was in an upright position and the desired amount of laponite was injected at a steady non-turbulent pace.
- The stopcocks on the cell inlet and outlet were closed.
- Waiting time was initiated.

In addition the following criteria was followed:

- Laponite powder was stored in a sealed container in a dry environment. Laponite powder is hygroscopic and will absorb water from the air over time.
- Room temperature was kept constant between 21 °C to 23 °C;
- Sample temperature was kept constant at all times.

The lab apparatuses used was:

- Mettler Toledo PB3002-S/FACT precision laboratory scale
- Stuart Scientific portable magnet stirrer SM27
- Vacuum diaphragm pump (MP 601 E)

3.3.3 Rheometry

To acquire the viscosities of our materials, we used a high precision falling ball viscosimeter, model B3 from VEB MLW, which is chiefly used for measurements of the viscosity of Newtonian fluids. The measured variable used to deduce the viscosity is the time required for a ball to fall under gravity through a sample-filled cylindrical tube with inclination 10° to the vertical [43]. The relation of the fall time to the viscosity is stated in the following formula [43, p. 10]:

$$\mu = t(Q_1 - Q_2) \cdot K, \tag{3.1}$$

where μ is the sample's dynamic viscosity in $\mathrm{mPa\,s^{-1}}$, t is fall time of the ball in s, Q_1 and Q_2 are the densities (at measuring temperature) of the ball and sample, respectively, in $\mathrm{g\,cm^{-3}}$, and K is a constant describing the ball interaction with the wall in $\mathrm{mPa\,cm^3 g^{-1}}$.

For Newtonian fluids the fall time is averaged over a series of measurements and viscosity is given directly from the formula. For shear-thinning, thixotropic fluids, like laponite, the procedure is a bit different. Thixotropy, in parallel with the progressive destruction of structures manifests itself by continuous reduction fall time, until reaching a minimum value. After the fluid is set in the apparatus, one has to wait for some time for the fluid structure to regenerate before conducting the measurements (see section 3.3.2 on laponite waiting times). Therefore, the first and longest fall time will correspond to the gel viscosity, and the minimum fall time reached after several measurements correspond to the sol viscosity. The relative decrease of viscosity is a direct measure of thixotropy and thus a useful characteristic of the substance tested [43, p. 12].

3.3.3.1 Calibration, deionized water

To check the apparatus, a test with deionized water was performed. The test was done at a room temperature of 294.9 K with a glass ball of density $Q_1 = 2.23\,\mathrm{g\,cm^{-3}}$ and ball constant $K = 9.69\,\mathrm{mPa\,cm^3 g^{-1}}$. The density of the water was measured to be $Q_2 = 1.00\,\mathrm{g\,cm^{-3}}$ and the average fall time of five measurements fall was found to be $t = 79.34\,\mathrm{s}$. Putting these figures into equation (3.1), we get the measured dynamic viscosity

$$\mu = 79.34\ \mathrm{s}(2.23\ \mathrm{g/cm^3} - 1.00\ \mathrm{g/cm^3}) \cdot 9.69 \cdot 10^{-3}\ \mathrm{mPa \cdot cm^3/g} = \underline{0.945\ \mathrm{mPa \cdot s}},$$

given with a three decimal accuracy as recommended by the instruction manual [43, p. 11].

The temperature dependence of the dynamic viscosity of water follows the equation

$$\mu(T) = 2.414 \cdot 10^{-5} \cdot 10^{247.8/(T-140\ \mathrm{K})}\ \mathrm{Pa{\cdot}s},$$

accurate to within 2.5% from 270 K to 640 K at standard atmospheric pressure [38, p. 18]. Applying the testing temperature gives the dynamic viscosity

$$\mu(T) = 2.414 \cdot 10^{-5} \cdot 10^{247.8/(294.9\ \mathrm{K}-140\ \mathrm{K})}\ \mathrm{Pa{\cdot}s} = \underline{0.96\ \mathrm{mPa{\cdot}s}},$$

which corresponds well with the measured dynamic viscosity. In conclusion the apparatus is calibrated within reasonable limits for our purposes.

Olive oil

Olive oil is not necessarily the same from batch to batch, and for our experiments we used a fairly old olive oil with expiration date in April 1993, so tabular values of viscosity was not to be used. The test was done at 294.7 K with a steel ball of density $Q_1 = 8.14\ \mathrm{g/cm^3}$ and ball constant $K = 0.122\ \mathrm{mPa{\cdot}cm^3/g}$. The density of the olive oil was measured to be $Q_2 = 0.90\ \mathrm{g/cm^3}$ and the average fall time of five measurements was found to be 88.71 s. Put into equation (3.1), we get the dynamic viscosity

$$\mu = 88.71\ \mathrm{s}(8.14\ \mathrm{g/cm^3} - 0.90\ \mathrm{g/cm^3}) \cdot 0.122\ \mathrm{mPa{\cdot}cm^3/g} = \underline{78.36\ \mathrm{mPa{\cdot}s}}$$

given with a two decimal accuracy as recommended by the instruction manual [43, p. 11].

Laponite

We used Laponite RD, which is a gel forming grade of laponite, in concentrations 2.9 % to 3.0 % and 3.5 %. Measurements were only done on the laponite of concentration 3.5 % with a waiting time $t_w = 10\,\mathrm{min}$, which was the shortest waiting time used for this concentration in our experiments. The test was done at 294.5 K with a steel ball of density $Q_1 = 7.7704\ \mathrm{g/cm^3}$ and ball constant $K = 10.075\ \mathrm{mPa{\cdot}cm^3/g}$. The density of the laponite was measured to be $Q_2 = 1.02\ \mathrm{g/cm^3}$. The initial laponite falling time was measured to be 402.10 s, and the minimum falling time, achieved after 16 runs, was 6.30 s.

Put into equation (3.1), we get the gel viscosity

$$\mu = 402.10\ \mathrm{s}(7.7704\ \mathrm{g/cm^3} - 1.02\ \mathrm{g/cm^3}) \cdot 10.075\ \mathrm{mPa{\cdot}cm^3/g} = \underline{27.35\ \mathrm{Pa{\cdot}s}},$$

and the sol viscosity

$$\mu = 6.30 \text{ s}(7.7704 \text{ g/cm}^3 - 1.02 \text{ g/cm}^3) \cdot 10.075 \text{ mPa·cm}^3/\text{g} = \underline{428.46 \text{ mPa·s}}.$$

Both viscosities given with a two decimal accuracy as recommended by the instruction manual [43, p. 11].

It is worth noting that the laponite regeneration was so fast that it was observable for the last measurement runs, in the sense that the falling ball was observed to accelerate considerably, so that shear-thinning still occurred. The speed was very fast at the end of the fall tube, so it is assumed turbulent flow occurred, which is not recommended according to the manual [43, p. 11].

3.4 Work-flow

The experimental procedure was adjusted several times during prototyping; listed here is the final version.

1. Experiment cell parts washed in workmanlike manner making sure there is no residue of oil and laponite, or dust.

2. Experiment cell assembled making sure no dust is present on the inside of the cell.

3. The inlet and outlet stopcocks are connected to the cell, both in open position.

4. The experiment cell is put under crossed polarizers to check for any birefringence caused by defects or uneven clamping. If there are defects present the cell must be diskarded.

5. The syringe is filled with degassed intrusion liquid, making sure to remove all air bubbles inside the syringe.

6. The syringe is connected to the injector rubber hosing with the hose stopcock open. The stopcock end of the hose is placed in a glass beaker to prevent spillage. The syringe is pressed and until the hose is completely filled with intrusion liquid, making sure there are no air bubbles inside the hose.

7. The syringe is attached to the syringe pump and the syringe pump is tested.

8. The stopcock on the end of the hose is closed, so that no air enters the intrusion liquid.

9. All camera settings, excluding focus, are set. Specifically, make sure the camera is in manual mode, with auto-focus off, and set the image quality and size, self-timer control, shutter speed, sensor sensitivity, focal length and aperture.

10. The light is switched on, the camera tested, and light switched off again to prevent heating.

11. The laponite is prepared and injected into the cell according to sample protocol.

12. Waiting time is initiated.

13. The box and cell are carefully dusted with compressed air.

14. 10 min prior to experiment, the cell is placed gently inside the box, lying horisontally on top of the polarizer sheet.

15. The camera focus is adjusted and the polarizer lens turned until the polarizers are perfectly crossed.

16. The cell stopcocks are opened.

17. The intrusion hose stopcock is opened and connected to the cell inlet, keeping any air bubbles from coming into the system.

18. The experiment box is closed.

19. 1 min prior to experiment the temperature is noted and the backlight turned on.

20. 10 s prior to experiment the camera is started

21. The syringe pump is started — experiment in progress.

22. The process is observed through the camera viewfinder.

23. The syringe pump is stopped when laponite or oil reaches the outlet.

24. Temperature is controlled to ensure no temperature change took place.

25. The experiment box is opened, all stopcocks are closed, hoses are diskonnected, and the cell disassembled, emptied and washed.

3.5 Particle image velocimetry

A superficial velocimetry was attempted on all experiments using the strongly birefringent laponite particles. Ideally one would use seeding particles designed for such purpose, but we wanted to see if the laponite particles themselves could at least give us some information about the bulk flow.

Using MatLab, the attempted procedure was as follows. Raw imagery in RGB color space was converted to LAB color space, where pixel intensity or lightness is put in a separate layer. This layer is extracted and contrast adjusted. The now pure intensity image was put through an opening morphological operation, using a large enough structuring element to remove all particles, leaving a smoothed image of the background birefringence. The opened image was subtracted from the intensity image and we were left with a grayscale image with much less noise, and particles standing out from background. These images was then input for a standard PIV performed in PIVsuite[44], a collection of MatLab code for PIV analysis.

Chapter 4

Results

A series of 14 intrusion experiments in Hele-Shaw cells were conducted, exploring the parameter space of 3 different independent variables in the following order:

Set 1:	laponite waiting time	t_w	[min]
Set 2:	laponite concentration (mass fraction)	C	[%]
Set 3:	injected fluid	IF	

The sections below present observations from the acquired image sequences, along with a qualitative image analysis. The results are presented set-wise, with an in-depth analysis of set 1, and more superficial analysis of the subsequent sets. Only a selection of the experiments are introduced. Last in the results chapter we present heterogeneities observed in the experiments.

All experiments are conducted inside a make-shift polariscope; meaning the observed features are all patterns of birefringence or polarization occurring inside the cell.

4.1 Set 1: laponite waiting time dependence

In set 1, six intrusion experiments were performed to explore intrusion phenomenology dependence on laponite waiting time. It is well known that waiting time, or ageing, is crucial for laponite rheology (see section 3.3.2). The analysis is divided into two parts, firstly morphology, where intrusion shapes and shape evolution are presented, and second flow study, presenting a study of flow and velocity parameters including basic velocimetry.

The laponite waiting time was varied in the range 45 min to 870 min, as seen in table 4.1. Olive oil was injected into a Hele-Shaw cell of aspect ratio $\epsilon = 0.030$ at a constant flow rate $Q = 5\,\mathrm{mL\,min^{-1}}$. The cell was filled approximately three quarters full with a laponite concentration C of small variation ranging from 2.9 % to 3.0 %.

Table 4.1: Overview of the experiments (N) forming set 1 and the waiting time (t_w) parameter variation

N	t_w
1	45
4	240
5	360
6	480
7	600
8	870

4.1.1 Intrusion morphology

All intrusions start with a round bubble around the inlet, developing into a smooth blob for short waiting times and rough blob for longer waiting times. Three blob examples ranging from smooth to rough are shown in figure 4.1.

For the shortest waiting time, 45 min, the blob inflates uniformly until it approaches a certain width, and elongates into to an oblong shape propagating in a steady manner towards the outlet. The time development of this experiment can be seen in figure 4.5.

For the four middle waiting times, 240 min to 600 min, the initial rough blob develops a flower-like fracture pattern around the outskirt of the blob, with fractures thin like hair strands spreading at various angles outwards from the blob towards the long edges and outlet of the cell.

Some examples of the flower pattern, including two of the medium waiting times and the longest waiting time, are shown in figure 4.2. The fractures composing the pattern increase both in length and number

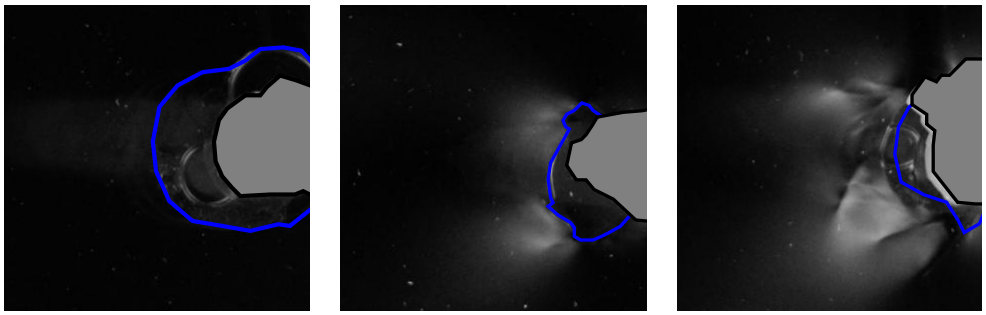

(a) N1, $t_w = 45\,\text{min}$ (b) N6, $t_w = 480\,\text{min}$ (c) N8, $t_w = 870\,\text{min}$

Figure 4.1: Typical initial blob roughness for different waiting times (t_w). Blob boundary in blue, inlet is gray. Examples from experiments 1, 4, and 8. Images are taken 7 s into the experiment.

as waiting times increase, furthermore, the backmost fractures form a parabola-like curve which widens with waiting time.

A noteworthy observation from the very thin flower-fractures (and other very thin fractures) was that no fractures were visible outside out of the polariscope, only the shape of the intrusion.

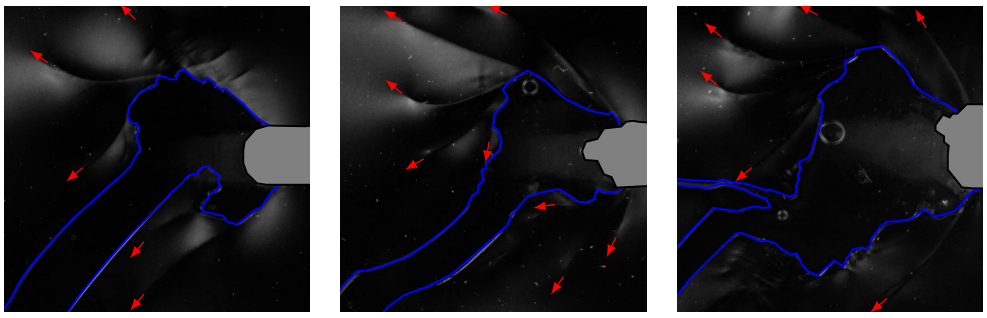

(a) N5, $t_w = 360\,\text{min}$ (b) N7, $t_w = 600\,\text{min}$ (c) N8, $t_w = 870\,\text{min}$

Figure 4.2: Examples of the flower-like fracture pattern emerging for medium to long waiting times (t_w). Blob boundary in blue, red arrows indicating the trajectory of the cracks composing the flower-like fracture pattern, the inlet is gray. Examples from experiments 1, 4, and 8. Images are taken 40 s into the experiment.

At the forward end of the blob thin fingers emerge; normally two fingers splitting at oblique angles to the cell centerline, so that they form a V-like shape as depicted in figure 4.3. In each experiment one of the initial fingers take the lead, hereafter referred to as primary fingers, while others,

referred to as secondary fingers, are suppressed early and slowed down, or even halted.

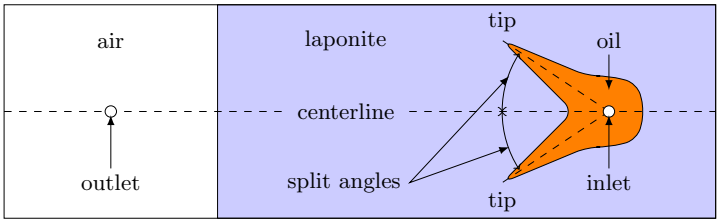

Figure 4.3: Cartoon explaining the tip splitting phenomena. Angle measurements are done at the time of tip splitting in the location described in the cartoon.

Some fingers do not follow the initial angle, and can be seen curving towards the cell edges at a later time step. When a finger tip approaches the cell edges two things may happen. For the most part, the finger starts clinging to the edge and follows it to the far end of the cell. In one event, $t_w = 240\,\text{min}$, the finger instead bounces of the edge leaving a rough blob with fractures and then proceeds to curve towards the opposite edge. These clinging and bouncing events are presented in figure 4.4.

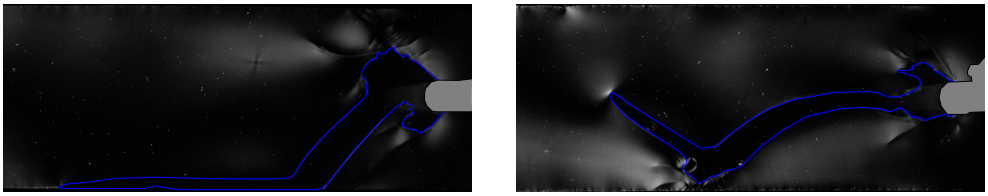

(a) Edge clinging (b) Edge bouncing

Figure 4.4: Edge clinging and bouncing examples. Left: edge clinging in experiment 5, $t_w = 240\,\text{min}$; right: edge bouncing in experiment 4, $t_w = 360\,\text{min}$. Intrusion boundary in blue, the inlet is gray.

The tip curvature range from rounded convex to acute concave and may vary from finger to finger, and as the finger propagates. After some time the fingers seem to stabilize in tip shape, width, and trajectory. An example of the time development in this regime is shown in 4.6.

For the longest waiting time, $t_w = 870\,\text{min}$, the initial blob is noticeably more jagged than the others. The flower-like pattern has more fractures and the fingers emerging have sharp tips, and are somewhat thinner than in the middle experiments. Both fingers from the initial split survives and propagate without noticeable hinder, clinging to each long edge of the cell.

A significant observation from experiment 8 is the abruptness of which the finger split occurs, the fingers covering great distance after first emerging. The time development of this experiment is shown in figure 4.7.

4.1.1.1 Contour analysis

The contours of intrusions is a key basis for morphology analysis in intrusion experiments, e.g. Lemaire et al. (1991)[15] or Hirata (1998)[8] Because the intrusion shapes were hard to extract through image analysis, I manually traced the intrusion contours. Only a selection of experiments was traced as this was a very time consuming approach. The traced contours can be seen in the in figure 4.8.

The manually traced curvatures fit well with the observed curvatures, however if we use the curvature development to calculate the current flow rate of the intrusions and compare it with the syringe pump flow rate settings, as seen in figure 4.9, we see that there are large fluctuations in the accuracy of the trace. If the contours were perfectly fitted we would expect the flow rates to be constant and similar to the pump rate, however the variations in flow rate are large and increase as the intrusion geometry gets complicated. Nevertheless, the mean measured flow rates, averaged over time, are not far from the actual flow rates. These flow rate measurements are to be seen as a qualitative measurement of the accuracy of the contour analysis below and are not treated as actual flow properties.

Curvature

Using the traced contours of late stage intrusions a limited curvature analysis was performed, as the curvature of an intrusion is often used as an indicator of the rheological conditions. In figure 4.10 one can see the local radii (in degrees) of the outer perimeter for each of the vertices in the curvature. Normally one would use the actual curvature instead of the radii, but as the traced curvature is a stepwise linear approximation this is hard to achieve without strange artifacts. The traced contours have a poor spatial resolution, so using the radii of the vertices means that the fine variations are not possible to derive, e.g. it is impossible to discern whether or not a tip has a convex or concave tip shape.

The curvature plot of the viscous blob of experiment 1 is overall relatively flat.

For the medium waiting times in experiment 5 and 6 the rugged initial blob is seen as a rapidly varying curvature, while the primary fingers are

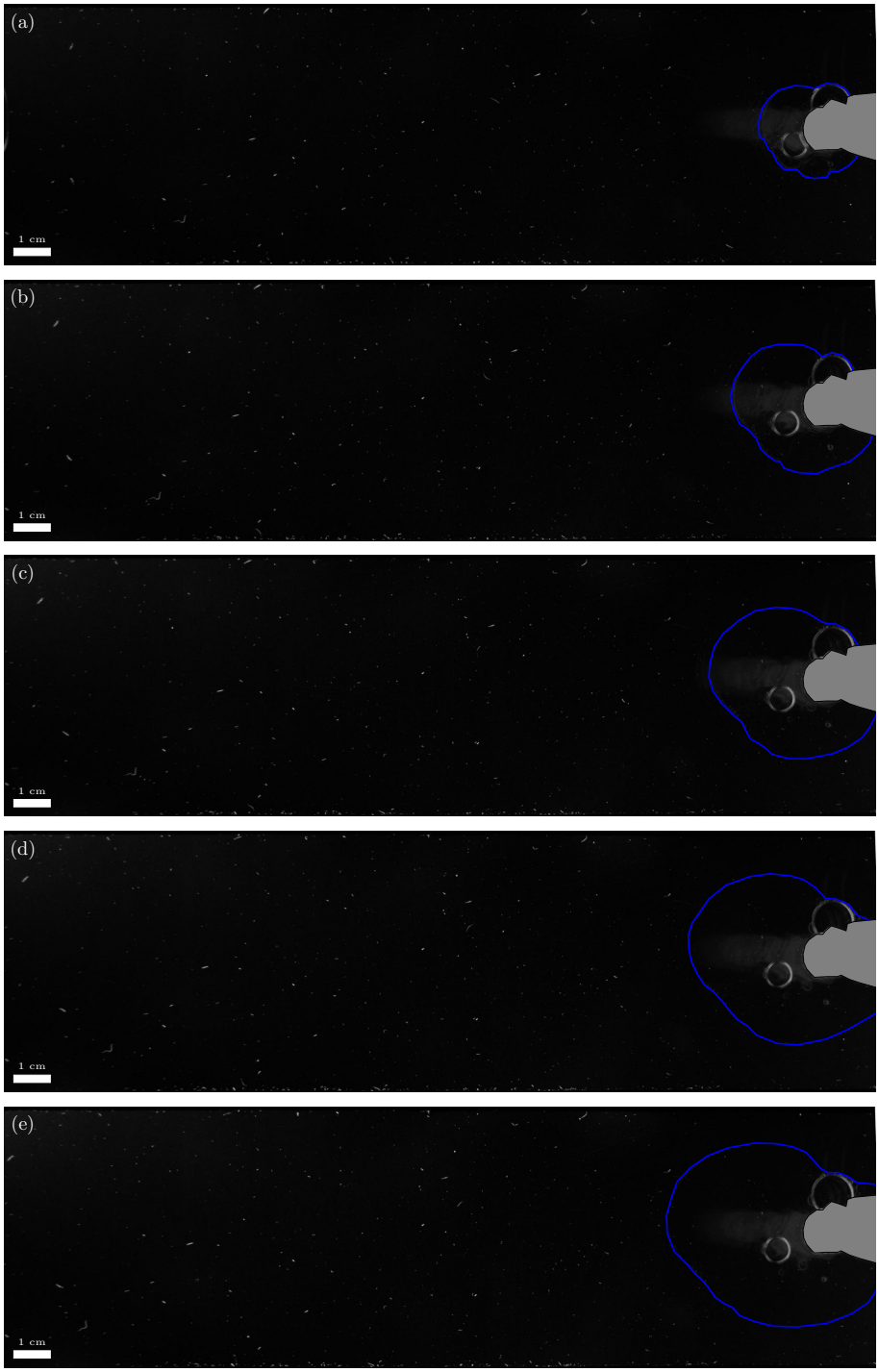

Figure 4.5: Selection of images showing the time development for experiment 1, $t_w = 45\,\text{min}$. The time-step between the images is 10 s. Intrusion boundary in blue, inlet is gray.

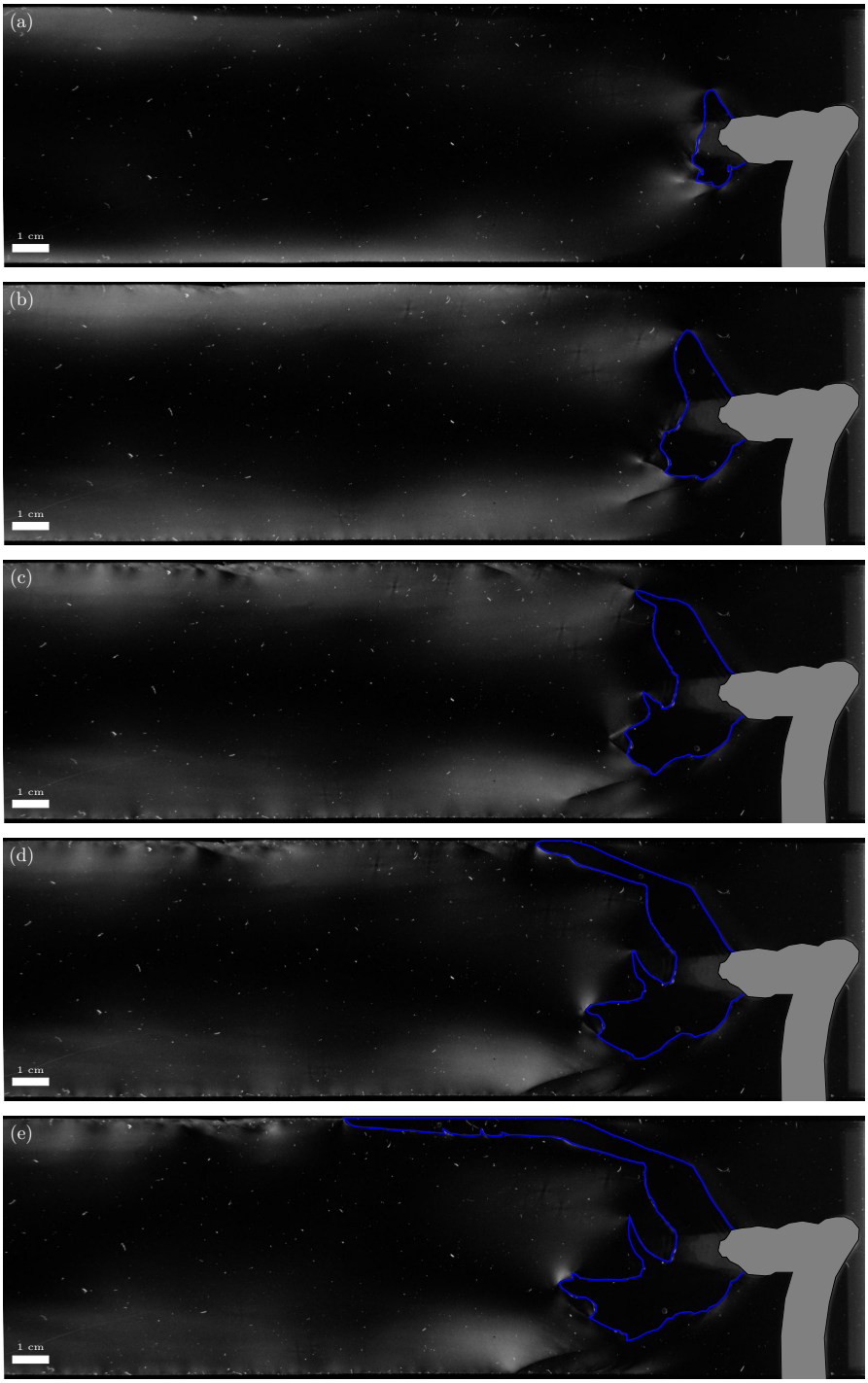

Figure 4.6: Selection of images showing the time development for experiment 6, $t_w = 480\,\text{min}$. The time-step between the images is 10 s. Intrusion boundary in blue, inlet is gray.

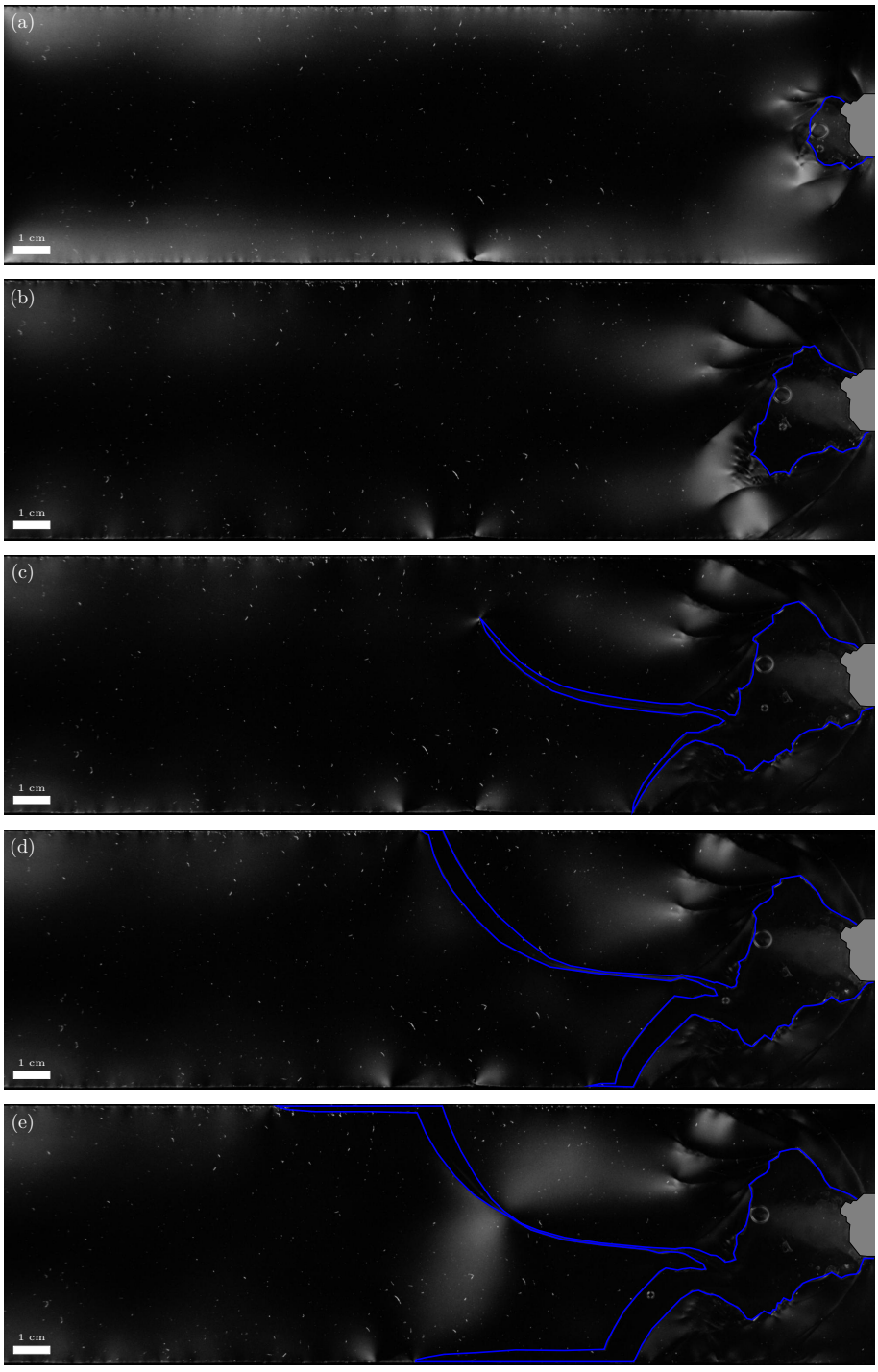

Figure 4.7: Selection of images showing the time development for experiment 8, $t_w = 870\,\text{min}$. The time-step between the images is 10 s. Intrusion boundary in blue, inlet is gray.

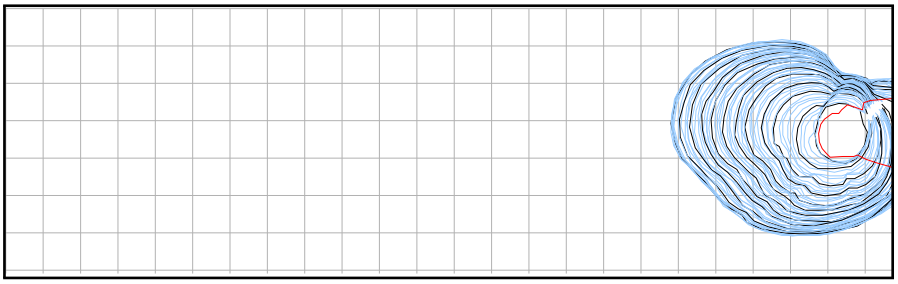

(a) Experiment 1, $t_w = 45\,\text{min}$

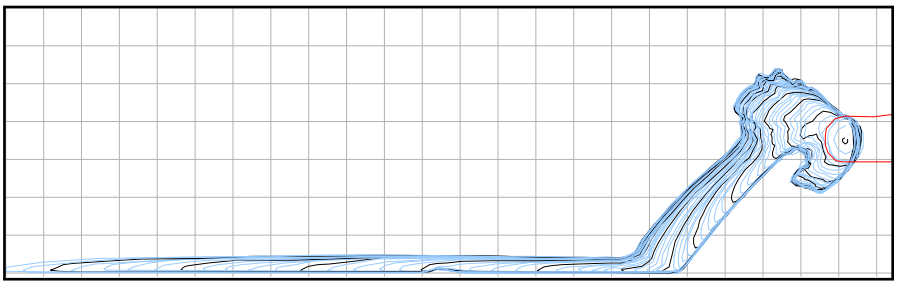

(b) Experiment 5, $t_w = 360\,\text{min}$

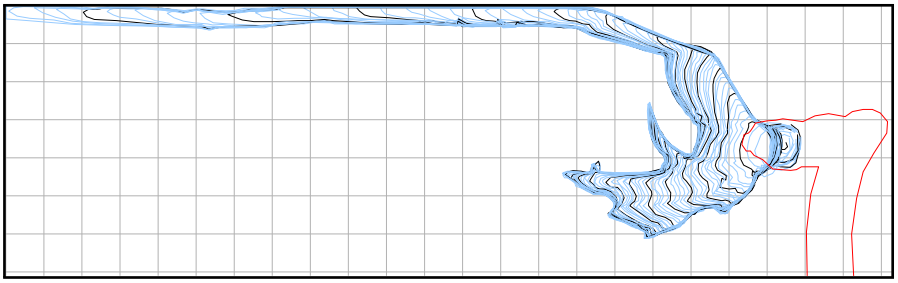

(c) Experiment 6, $t_w = 480\,\text{min}$

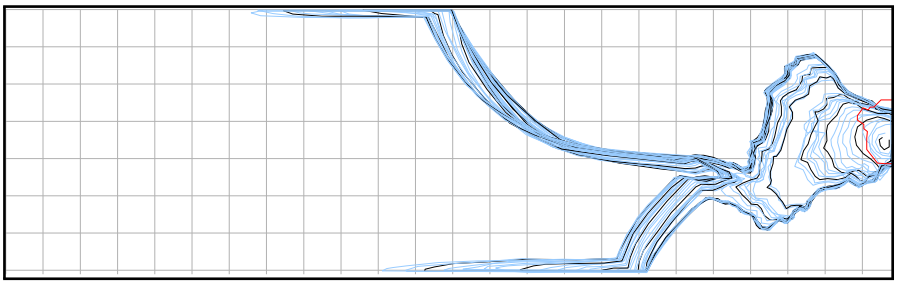

(d) Experiment 8, $t_w = 870\,\text{min}$

Figure 4.8: Contour plot showing the time development of experiment 1, 5, 6, and 8. Blue contours show the development per second, black per 5 seconds. The red lines indicates were the inlet blocks the view. Grid lines have 1 cm spacing.

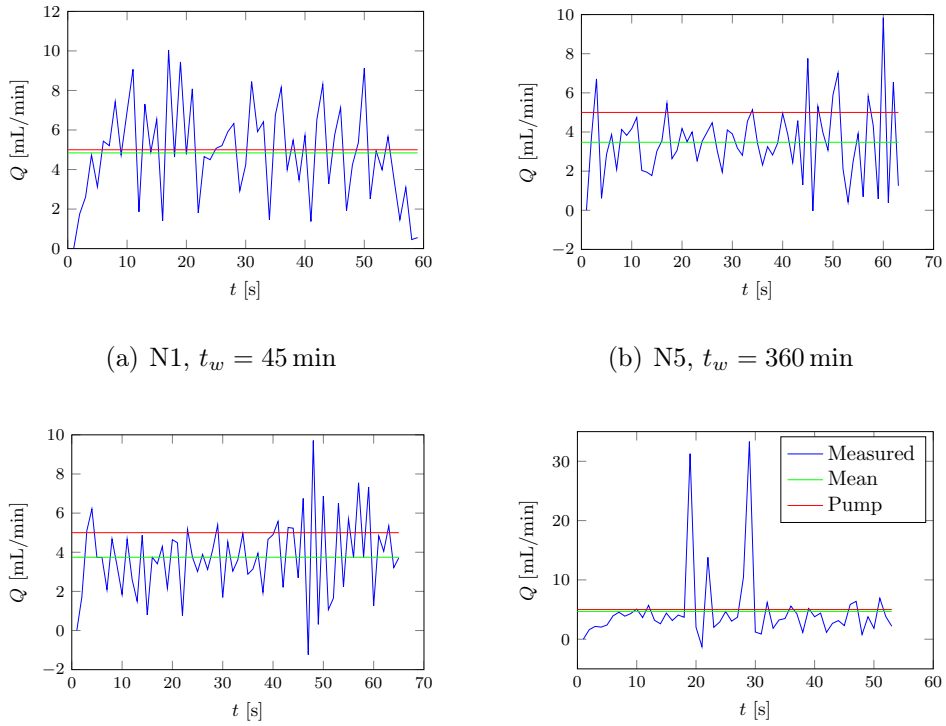

(a) N1, $t_w = 45\,\text{min}$

(b) N5, $t_w = 360\,\text{min}$

(c) N6, $t_w = 480\,\text{min}$

(d) N8, $t_w = 870\,\text{min}$

Figure 4.9: Continuous flow rate plots based on intrusion contour tracing for experiments 1, 5, 6, and 8. The continuous flow rates can be seen as a qualitative measure of the accuracy of the contour analysis.

expressed as acute extrema surrounded by relatively flat curvature being the edges of the fingers. A difference between the two can be seen. Experiment 5 has a smooth finger making near straight angles with the blob, represented by the two minima left and right of the primary finger peak. In experiment 6, on the other hand, these finger exit minima are hidden in the jaggedness of the blob.

This is also seen for the intrusion in experiment 8, with longest waiting time. In addition the finger has large angles left and right of its primary and secondary finger curvature hailing from the near right angle from where the fingers starts clinging to the edges.

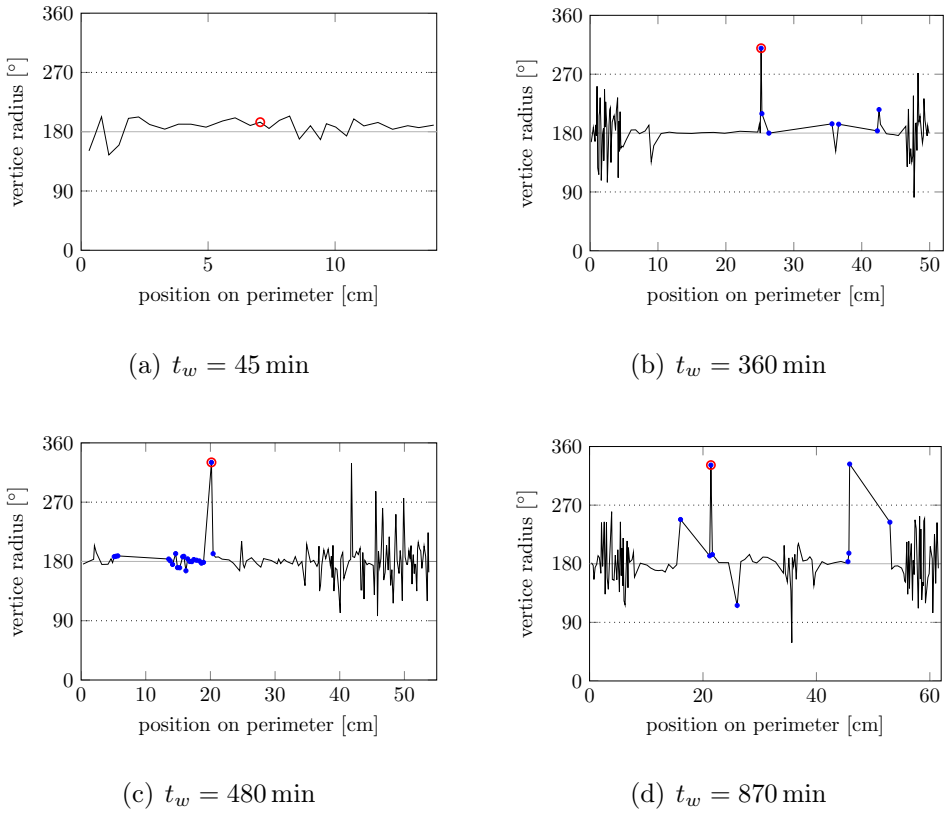

(a) $t_w = 45\,\text{min}$

(b) $t_w = 360\,\text{min}$

(c) $t_w = 480\,\text{min}$

(d) $t_w = 870\,\text{min}$

Figure 4.10: Intrusion curvature of experiment 1 (a), 5 (b), 6 (c), and 8 (d). The curvature is expressed using local radii of the vertices of the outer perimeter of the intrusion shape in the late stage of the experiment. The vertical axis is counterclockwise angle in degrees, the horizontal axis is intrusion perimeter length in cm. A flat curvature would be at 180°, with larger values being a concave bend and smaller values a convex bend in respect to the outer perimeter. The red ring marks the primary finger, while blue dots show where the intrusion is within 2 mm of the long edges of the cell.

Volume and perimeter

The traced contours also provide a means to get the intrusion volume and perimeter length as a function of time as seen in figure 4.11. One would expect the same linear volume increase for each of the experiments as the flow rate is constant, and this is the fact for experiments 1, 5, and 6, with 5 and 6 slightly lower volume increase than 1. Experiment 8 on the other hand, shows a linear increase interrupted by two abrupt volume increases at 18 and 28 s.

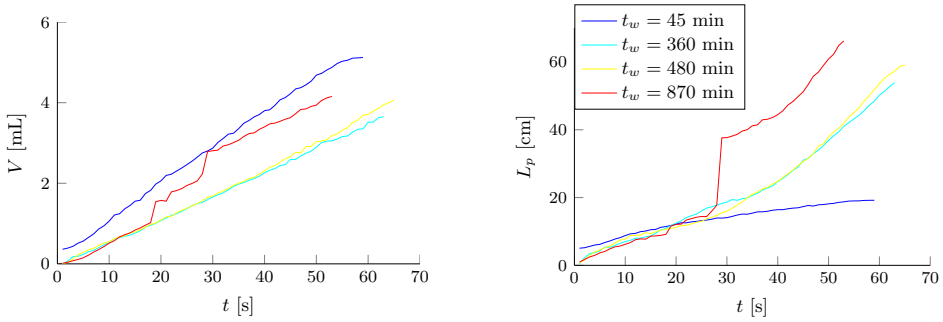

(a) Intrusion volume

(b) Intrusion perimeter

Figure 4.11: Intrusion volume (a) and perimeter (b) as a function of time for different waiting times.

The perimeter length evolution shows slowly decelerating increase for the shortest waiting time, which one would expect for an expanding round body. The medium waiting times shows the same trend as the initial blobs increase in size, with an accelerated increase when the primary finger starts to grow and even more when the finger connect with the cell edge, then stabilizing when the finger propagates in a somewhat stable manner.

Again the longest waiting time displays errant behavior. The perimeter length increases similar to the other experiments until it reaches 18 s where a small sudden increase occurs. At 28 s a large sudden increase is seen before the increase again follows a steady path. The largest volume and perimeter length increases for the longest waiting time are concurrent with the sudden finger propagation when the fingers first emerge.

4.1.1.2 Finger tip shape

The curvature analysis was too inaccurate to describe the tip shapes, but looking at the images provides the desired detail. A humble selection of tip

shape variety can be seen in figure 4.12, where the variation for different waiting times is shown, and figure 4.12, where the spatial variation for different fingers in experiment 6 is shown.

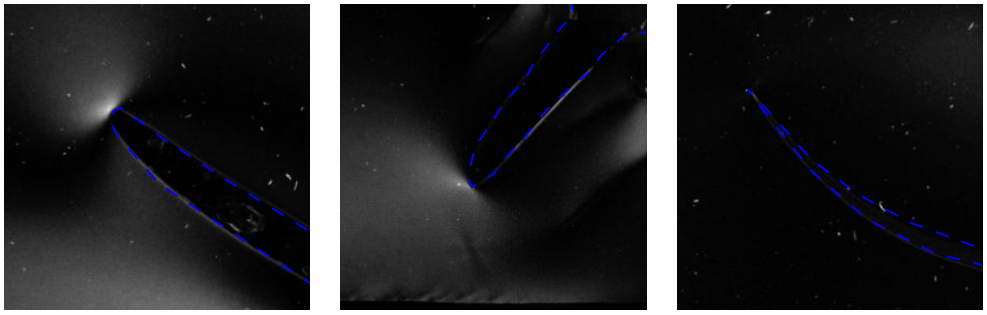

(a) N2, $t_w = 240\,\text{min}$ (b) N3, $t_w = 360\,\text{min}$ (c) N8, $t_w = 870\,\text{min}$

Figure 4.12: Examples of tip shape variation for different waiting times. Intrusion boundary in blue.

For the shortest waiting time (experiment 1, $t_w = 45\,\text{min}$, not depicted) the round-shaped intrusion is the finger. Examples of the narrower but still rounded finger tips of the lower medium waiting times (experiment 4 and 5, $t_w = 240\,\text{min}$ and $t_w = 360\,\text{min}$, respectively) can be seen in figure 4.12(a) and 4.12(b). The curvature is convex around the whole, with a sharpening in the front that distinguishes the tips from the rounded blob of experiment 1.

For the upper medium waiting times, (experiment 6 and 7, $t_w = 480\,\text{min}$ and $t_w = 600\,\text{min}$, respectively), an abundance of different shapes can be seen, with the primary fingers showing sharp, but still convex tip shapes. In figure 4.13 we see a series of different tip shapes from experiment 6, which are taken from the same time frame, but on different fingers as seen in the reference map, figure 4.13(d).

Figure 4.13(a) shows the primary finger tip which is sharp and convex. Figure 4.13(b), depicting the secondary finger tip, has about the same sharpness, but the walls on the tip are fairly straight meeting at the tip point producing a wedge-like tip shape. In figure 4.13(c) we see a tertiary finger emerging between the primary and secondary. It has a very sharp tip with convex curvature on the left side and concave curvature on the right side, so that the finger makes a bend towards the right as it propagates.

The same tip shape can be seen for the longest waiting time (experiment 8, $t_w = 870\,\text{min}$) in figure 4.12(c), albeit with an even narrower finger and sharper tip.

An interesting observation concerning the tips is the high intensity birefringence in the laponite gel in front of them, often displaying a lobe pattern, e.g. 4.12(b).

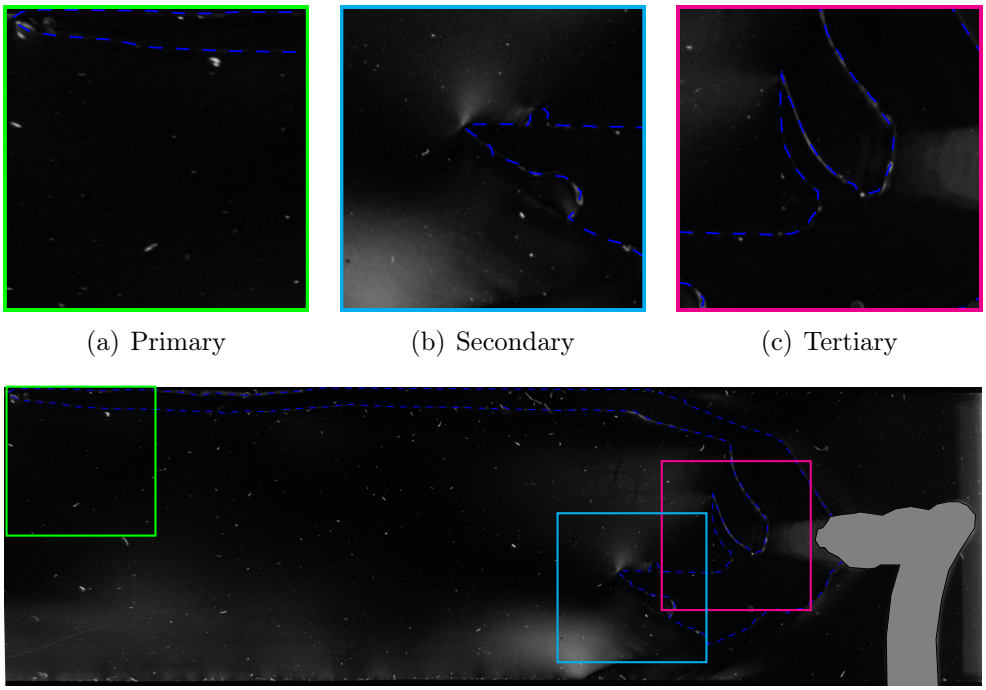

(a) Primary (b) Secondary (c) Tertiary

(d) Spatial reference map

Figure 4.13: Examples of tip shape spatial variation in experiment 6, t_w = 480 min. The primary (a), secondary (b) and tertiary (c) fingers in the last image before the primary finger exits are shown. See (d) for spatial reference. Intrusion boundaries in blue, inlet is gray

4.1.1.3 Finger widths

The primary fingers width (W_f) was measured for selected experiments on images where the finger was perceived as relatively stable. The widths were averaged over 5 sections with 1 cm spacing from approximately 2 cm to 7 cm behind the tip.

The finger widths are shown in the table and plot in figure 4.14. The collected widths are indicative of finger narrowing as waiting time increases and the laponite becomes stiffer. If a regression fit of the scatter was to be performed a first guess would be a hyperbola fit, or linear fit if using the reciprocal time. To perform an acceptable fit more precise measurements

are needed, especially in the waiting time range between the first and second experiment (45 min to 240 min) were there is a jump in values.

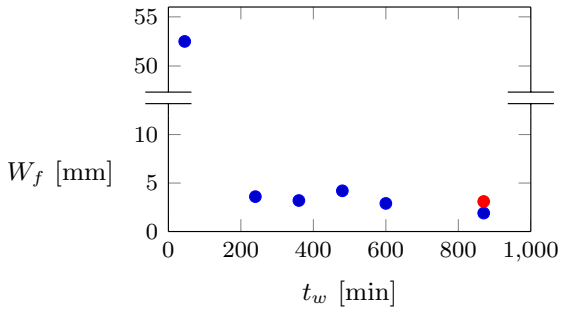

N	t_w	W_f ●	λ_f
1	45	52.5	0.74
4	240	3.6	0.050
5	360	3.2	0.045
6	480	4.2	0.059
7	600	2.9	0.040
8	870	1.9	0.028
8	870	3.1●	0.044

Figure 4.14: Plot and table of the finger width W_f as a function of waiting time t_w. The table also lists the finger width to cell width ratio, or relative finger width λ_f. The blue dots marks the first fingers, while the red dots marks the secondary fingers which were suppressed for all but the longest waiting time.

The longest waiting time (experiment 8, $t_w = 870$ min) produces two stable fingers of different widths; however the secondary finger propagated through a laponite gel that had been subjected to more flow than the primary. Considering the shear-thinning behavior of the gel, one should expect the primary finger to travel through a laponite gel with more viscosity and elasticity than the secondary finger. This would explain the fact that the primary finger is thinner than the secondary. This is also the reasoning behind choosing the primary finger width as the relevant figure when discussing an overall trend of narrowing with waiting time.

The table in figure 4.14 also provides the relative finger width (λ_f) of each finger as this is found to be a characteristic of fingering in Newtonian and low shear-thinning rheologies (see section 2.2.5.2 in the literature review). For classical Newtonian viscous fingering the relative finger width has a upper limit of $\lambda_f = 1/2$[1], meaning the finger in experiment 1 (λ_f), was not fully evolved in the last image taken. The other experiments show relative finger widths considerably lower than the limit, which is consistent with the literature review.

4.1.1.4 Tip splitting angles

As mentioned, the initial tips often come in pairs forming a V-like shape, with each finger initially propagating at angles in respect to the cell centerline. As fingering occurs with characteristic wavelengths (see section 2.2.5.2), we suggest that the tip splitting angles is dependent on these and

the cell geometry. These angles, listed in the table in figure 4.15, are measured at the first occurrence of observable tip splitting. Because of the irregular shape of many of the fingers, these measurement are highly suggestive, and the figures are rounded to the nearest 5°. Nevertheless, there seems to be a link between the tip splitting angles and the laponite rheology.

The initial splitting angles are plotted in figure 4.15 and the scatter plot of the primary fingers seem to follow a bell-shaped curve. For the two shortest waiting times the primary fingers follow small angles. The angles increase steadily for longer waiting times until reaching the largest observed angle in experiment 6, then the angles narrow again when reaching the more elastic regime for the two longest waiting times. The secondary fingers do not follow the same curve, so more data is needed for a satisfactory regression fit.

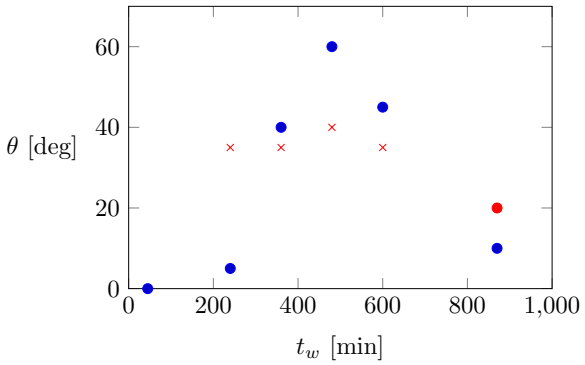

N	t_w	θ_1 ●	θ_2 ●
1	45	0	-
4	240	5	35x
5	360	40	35x
6	480	60	40x
7	600	45	35x
8	870	10	20

Figure 4.15: Plot and table of initial tip splitting angle θ as a function of waiting time. Primary fingers in blue, secondary in red. Suppressed and halted secondary fingers are marked with a cross.

4.1.2 Matrix and intrusion flow properties

In this section we study the flow properties using different approaches. First a bulk flow profile is estimated on the basis of observed particle flow and birefringence banding. Then we present measurements of tip velocities for the primary fingers, and lastly finishing the flow study with a basic PIV.

4.1.2.1 Laponite flow velocity profiles

In the far end of the cell a cross-sectional flow velocity profile of the laponite should be representative for the rheological regime. Observing the particle

flow and laponite birefringence provides an approximate solution, and the sketch in figure 4.16 shows these assumed laponite flow velocity profiles.

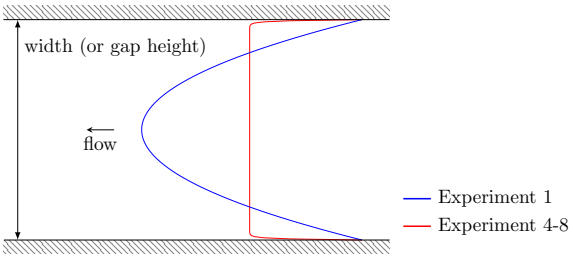

Figure 4.16: Sketch showing caricatured velocity profiles in experiments of set 1 based on observations of particle flow. Experiment 1 had waiting time $t_w = 45\,\text{min}$, while experiments 4 to 8 had waiting times $t_w = 240\,\text{min} to 870\,\text{min}$. The velocity profile scale is exaggerated in the flow direction to highlight the differences.

For the shortest waiting time, particles in the plane of the cell seem to flow with a parabolic-like velocity profile. Interestingly, in this experiment, particles following the same streamlines seem to have different velocities. This suggests that a similar flow-profile is present also normal to the plane of the cell, and that we observe a two-dimensional parabolic velocity profile. No flow birefringence is observed for this waiting time.

In experiments with medium and long laponite waiting times, the particles follow a seemingly flat flow profile with only small velocity slow-down at the edges of the cell. Particles on the same streamline have the same speed, unless they are fixed. The particle flows in these experiments are too similar to differ them apart; nevertheless, subjectively the particles follow a typical shear-thinning velocity profile, with an approximately flat profile normal to the plane.

The longer waiting times have distinct birefringence bands along the cell edges, well illustrated earlier in figures 4.6 and 4.7. From no birefringence in the first images, the bands starts at the inlet propagating fast until reaching the air-laponite interface in the far end of the cell. The intensity increases as intrusion occurs, especially towards the cell long edges. After some time, the laponite gradually provides less resistance to flow, and the birefringence bands slowly diminish.

4.1.2.2 Tip velocities and conduit flow

We measured the primary finger tip velocities and calculated the conduit flow, as tip propagation rate and internal flow is known to vary from dykes to diapirs, or from hydraulic fracturing to viscous fingering (see section 2.1.3).

The velocities v_f, listed and plotted in figure 4.17, were based on tip displacement in a 10 s time frame — less for fast propagating fingers. The velocities were measured on the images where the fingers were considered as stable as possible.

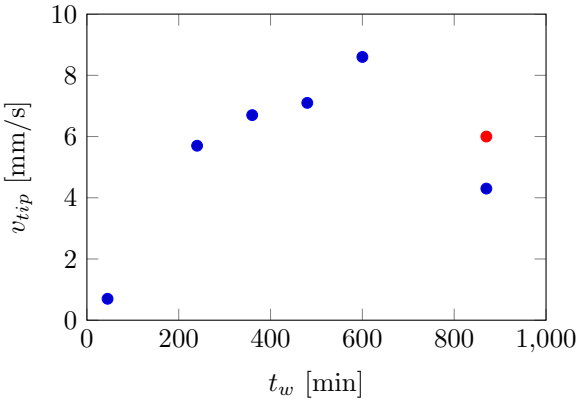

N	t_w	v_{tip}	Q_f	Q_f/Q
1	45	0.7	4.6	0.92
4	240	5.7	2.6	0.52
5	360	6.7	2.7	0.54
6	480	7.1	3.8	0.76
7	600	8.6	3.1	0.62
8	870	4.3	1.0	
8	870	6.0	2.3	
8T			3.3	0.66

Figure 4.17: Plot and table of the tip velocities u_{tip} [mm/s]as a function of waiting time t_w [min]. The table also lists the conduit flow rate Q_f [mL/min] and the last column, Q_f/Q, is the ratio of flow in the finger in respect to the pump flow rate. Experiment 8 had two fingers, and the flow rate is summed in the last row under the index 8T. The blue dots marks the primary fingers, while the red dot marks the secondary finger for the longest waiting time.

In the tip velocity plot a tendency for finger tip velocity increasing with waiting time is evident in all but the longest waiting time (experiment 8, $t_w = 870$ min), where there is a drop in tip velocity. This is as expected since there are two fingers propagating simultaneously and the fluid load is shared between the two. There are too few measurements for an acceptable regression fit, but the tip velocity increase seems to decelerate as waiting time becomes longer, like it is approaching a limit.

The primary fingers' cross-sectional conduit flow rate Q_f, also listed in the table in figure 4.17, were estimated using the following formula:

$$Q_f = v_f H W_f,$$

where H, the cell gap height, and W_f, the finger width, composes the cross-sectional area over which the conduit flow rate is calculated. The ratio of

finger flow rate to pump flow rate is also calculated, and indicates how much of the flow is carried inside the conduit of the finger and how much is directed to deformation of the laponite gel matrix along the finger.

Looking at the ratio of finger conduit flow rate to the pump flow rate, listed in the table in figure 4.17, it can be seen that for the shortest waiting time (experiment 1, $t_w = 45\,\text{min}$), the flow rate in the finger approaches the pump flow rate. For the medium to long waiting times (experiment 4-8, $t_w = 240\,\text{min} to 870\,\text{min}$), a substantial part of the flow occurs in the surrounding gel matrix.

The internal flow velocity profile is hard to measure as we have not prepared the experimental setup for such measurements. However, the motion of particles and bubbles inside our intrusions provides rough characteristics of the velocity profile. In figure 4.18 we follow a chunk of laponite moving freely inside an oil intrusion, clearly having greater speed than the intrusion tip. This is also seen for air bubbles inside the flow, even though the bubble in the example is stuck in a rough bend of the intrusion. Some smaller particles can be seen first traveling fast and erratically in the center of the intrusion until reaching the tip, where they move to the intrusion side walls and stop or move backwards at a slower speed.

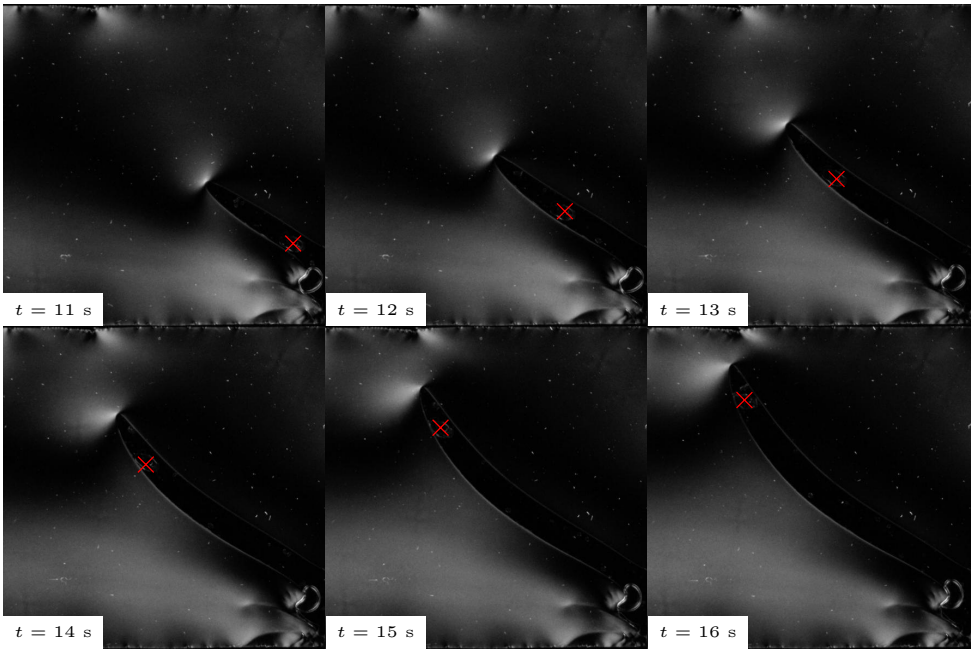

Figure 4.18: The movement of a laponite chunk (red cross) inside an oil intrusion as an example of observed intrusion conduit flow properties. The time step between the images is 1 s. From experiment 4.

The observation of high flow rates inside the intrusions is also supported by the PIV velocity field plots e.g. at the tip of the primary finger in the bottom plot of figure 4.21.

4.1.2.3 Particle image velocimetry

To support the flow observations we performed a basic PIV analysis and were able to derive velocity fields and cross-sectional flow profiles for a selection of experiments.

An example of the PIV-derived velocity fields (experiment 6) is shown in figure 4.21. The vector plots show that the laponite flow is fairly homogeneous from the inlet towards the outlet, while the area towards the right edge of the cell has near-zero velocities and no preferred direction. As the intrusion propagates we can see that velocities along the cell edges increase. A bending of the velocity field close to the intrusion also occurs in such a way that the velocity vectors are pointing away from the intrusion. As birefringence in the cell increase we can see errant velocities in the areas with high intensity birefringence, which is likely to hail from noise that we were unable to filter out.

In figure 4.19 we have plotted five equally spaced cross-sectional velocity profiles corresponding to the velocity field plots in figure 4.21. We see that, initially, the velocity profile is somewhat curved, and similar to the parabolic profile we inferred in figure 4.16 for experiment 1. All cross-sectional profiles at $t = 10\,\mathrm{s}$ seem to be similar, but the profiles become more noise the closer they are to the inlet.

As time passes we see that the profiles on average show a more flattened shape similar to the non-parabolic profile in figure 4.16, and that the spatial difference becomes larger, with profiles in the far end of the cell showing higher velocities than that of the cross-sections close to the inlet. In the profiles at $t = 50\,\mathrm{s}$ we can see that the laponite is almost stagnant for the to cross-sections closest to the inlet. Both of these cross-sections have been passed by the primary finger. The profiles show an increased amount of peaks as time passes, both in positive and negative direction, and although some of these peaks can be explained by the intrusion passing through the respective cross-sections, most of the peaks have no logical explanation in the flow itself. The noise is most prominent on the cell edges, i.e. where the birefringence intensity is highest.

We also did a velocity profile comparison between experiments 1, 6, and 8, shown in figure 4.20. Two series of profiles is shown for each experiment, one at $t = 10\,\mathrm{s}$ and one at $t = 50\,\mathrm{s}$. We see that the profiles in experiment 1 are very noisy and, while in the expected velocity range,

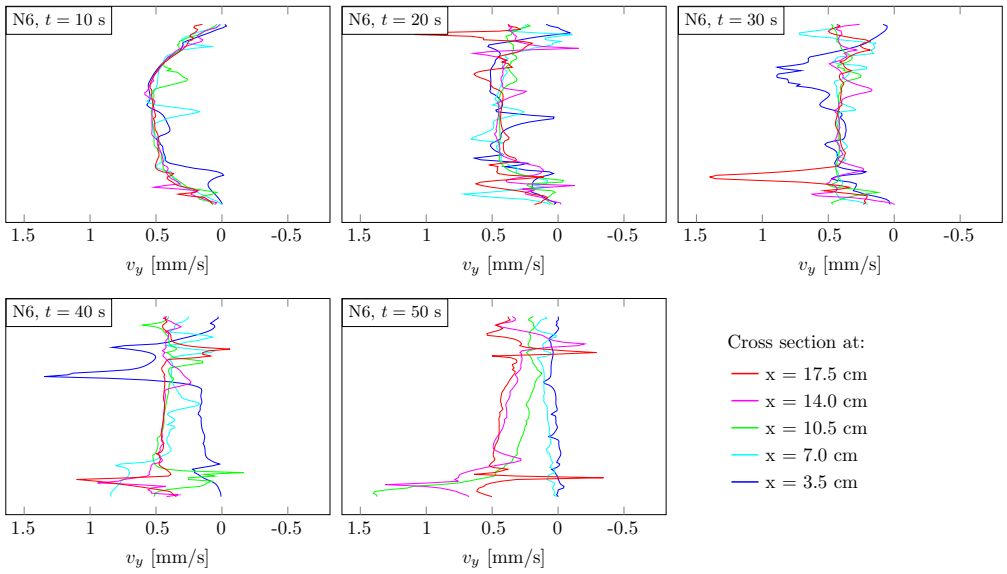

Figure 4.19: Velocity profiles v_y of experiment 6 ($t_w = 480\,\text{min}$) from PIV. The profiles are extracted from the cross-sections depicted in figure 4.21. The cross-section distance in the legend is measured from the outlet side of the images, that is; the red lines are closest to the inlet, the blue lines are closest to the outlet.

completely unintelligible. However, as we remember from the observations of particle flow in section 4.1.2.1, experiment 1 showed different particle velocities along the same streamline, which is a likely source for the noise. If we can say anything about the flow profiles of experiment 1 based on PIV, it must be they are consistent in noise and velocity range over time.

If we instead compare experiments 6 and 8, we see that in spite of very distinct peaks at the cell edges, both negative and positive, experiment 8 clearly has a considerably flatter velocity profile at $t = 10\,\text{s}$, very similar to the non-parabolic profile caricatured in figure 4.16. For $t = 50\,\text{s}$, at which point experiment 8 has to propagating fingers and much birefringence, the velocity profile plot gets messy again, but we see that also here the velocity profile has a higher mean furthest away from the inlet.

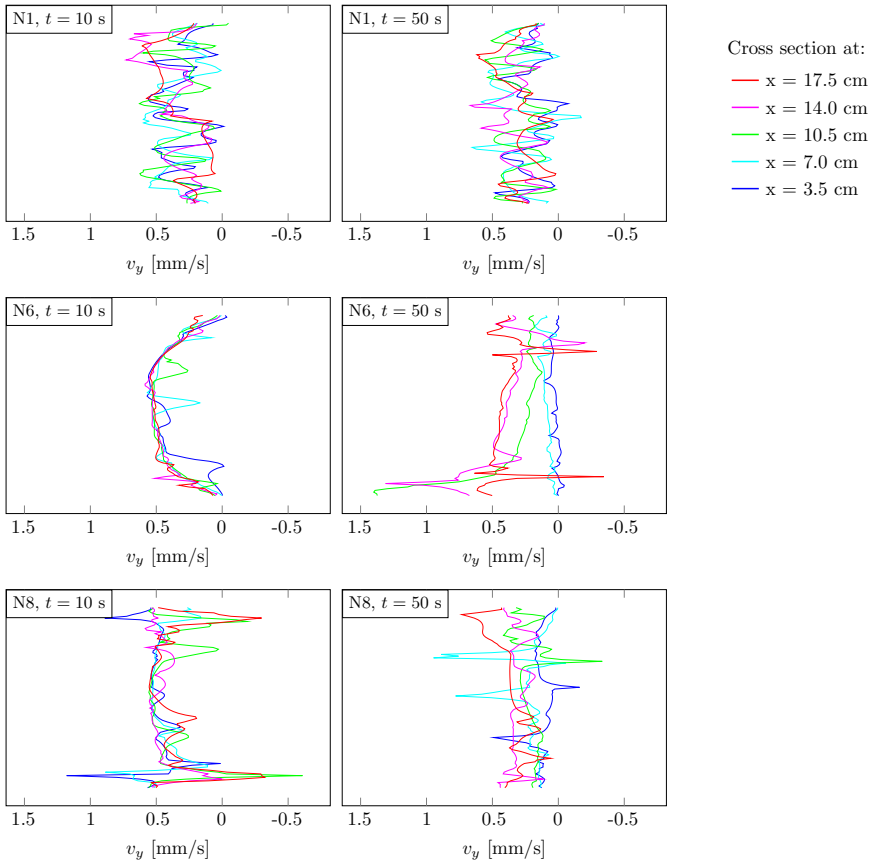

Figure 4.20: Cross sectional velocity profiles v_y of experiment 1 ($t_w = 45\,\text{min}$), 6 ($t_w = 480\,\text{min}$), and 8 ($t_w = 870\,\text{min}$), from PIV. The profiles are extracted from cross-sections similar to what is depicted in figure 4.21. The cross-section distance in the legend is measured from the outlet side of the images, that is; the red lines are closest to the inlet, the blue lines are closest to the outlet.

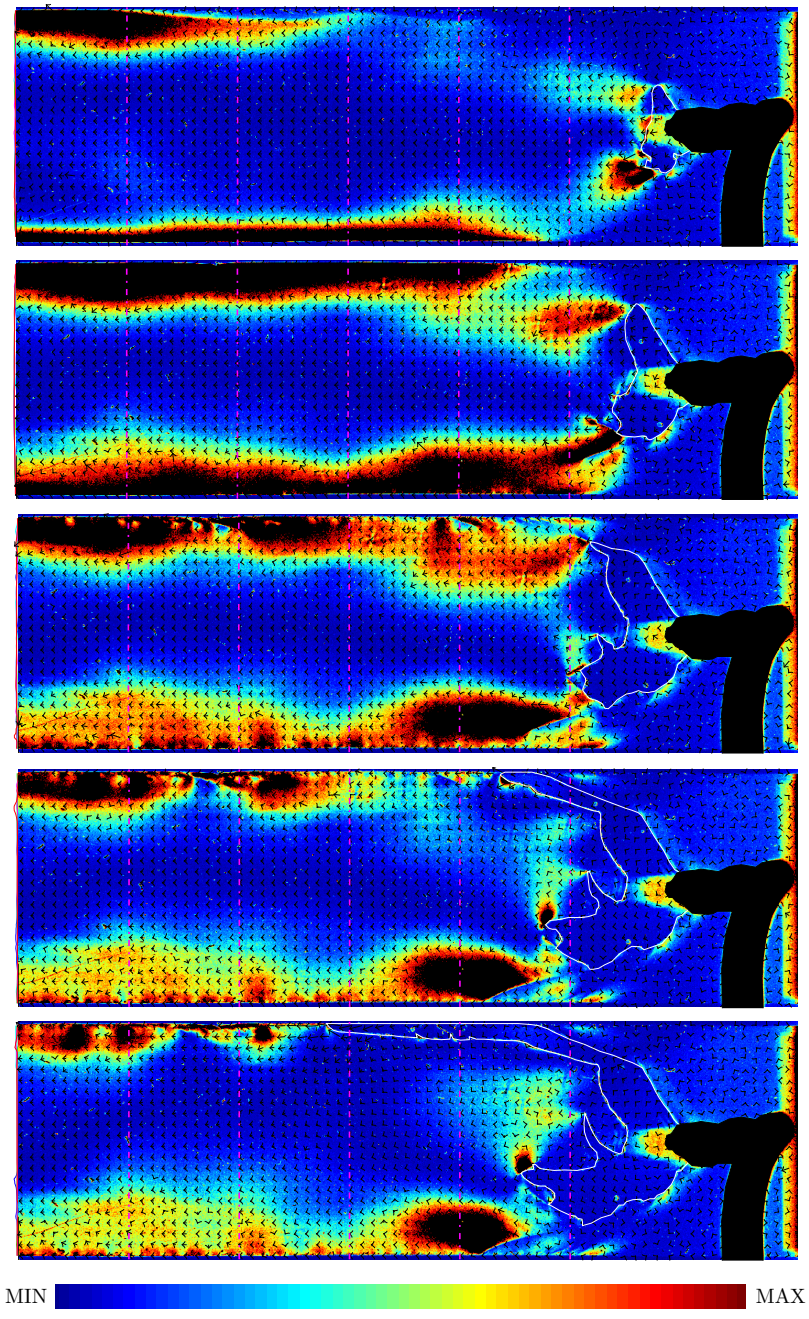

Figure 4.21: Velocity field in experiment 6, waiting time $t_w = 480\,\text{min}$. The time interval between the frames is 10 s, and the images are chronologically ordered from top to bottom. The vector velocity field (in black) is layered over an birefringence intensity image (color scale bar at the bottom), the intrusion boundary is in white, while the inlet is blacked out. The vertical magenta dash-dotted lines show the cross-sections where velocity profiles are extracted.

4.2 Set 2: laponite concentration dependence

As with waiting time, the laponite concentration is reported to affect rheology (see section 3.3.2). Only 2 intrusion experiments were performed varying the laponite concentration. The concentration was $C = 2.9\,\%$ for experiment 1, and $C = 3.5\,\%$ for experiment 14. The waiting time was not constant, but similar at $t_w = 45\,\text{min}$ and $t_w = 60\,\text{min}$ respectively. In both experiments olive oil was injected into a Hele-Shaw cell of aspect ratio $\epsilon = 0.030$ at a constant flow rate $Q = 5\,\text{mL}\,\text{min}^{-1}$.

An effect of increasing the concentration to $C = 3.5\,\%$ is present already in the sample preparation phase. A vortex is produced during mixing in the gels, and for the low concentration this vortex is stable in shape for the entire mixing time. For the higher concentration on the other hand, the vortex narrows considerably during mixing and it is evident that the laponite gelation process is faster than the rate of which laponite bonds are broken down in this particular mixing procedure.

The blob slowly evolving to a wide finger for a laponite concentration of $C = 2.9\,\%$ in experiment 1, was presented in the previous sections and figure 4.5. In comparison, the shapes of experiment 14 are still rounded, but much narrower.

As can be seen in figure 4.24, the initial blob only experience a minuscule expansion before tip splits at approximately 30° angles. The secondary finger is halted almost immediately while a primary finger of width 9 mm propagates steadily, bending slowly towards the cell center until it becomes parallel with the cell centerline 20 s out in the experiment. A perturbation of the tip is visible at this point, but fingering is subdued. The tip sharpens slightly after the attempted tip split, however blunts again. At the very last image frames, before the finger exits the view, one can see another perturbation of the tip which is shown in detain in figure 4.22(a). The tip splitting seemed to happen at similar wavelengths of perturbation. For all three tip splits, halted or not, a characteristic perturbation wavelength of 7 mm to 8 mm was observed.

The birefringence banding seen in experiment 14 is similar to what is seen in experiments 4-8 from set 1. However, one feature stands out. In figure 4.22(b) one can see the emergence of what is believed to be localized shear zones within each of the laponite birefringence bands, forming a flow channel in the laponite. The intrusion finger keeps within this flow channel at all times, clinging to the shear zone instead of the cell edge. The observed particle flow substantiate the presence of shear zones, as particles within the flow channel move with a velocity profile similar to what is described for experiment 4-8 in figure 4.16, while particles outside the flow channel

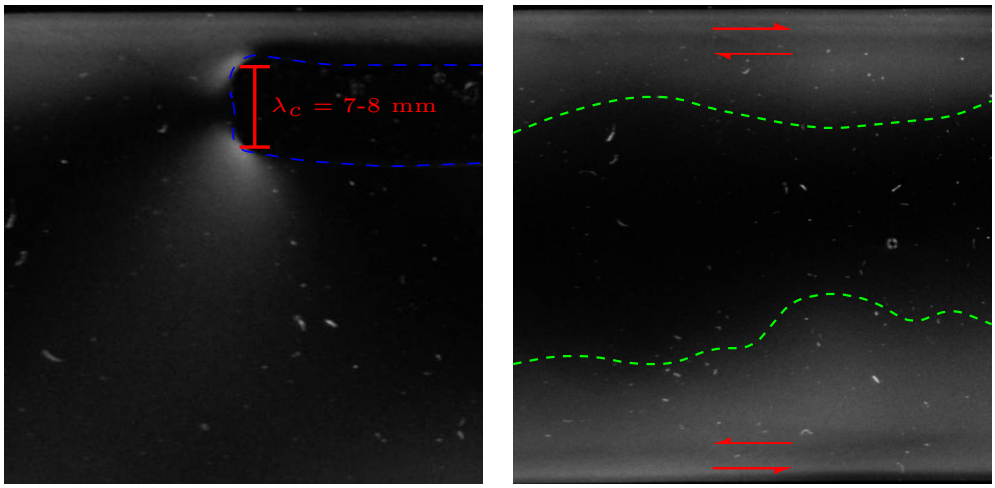

(a) Tip splitting (b) Localized shear zones

Figure 4.22: Details from experiment 14. Subfigure (a) shows the tip splitting of the primary finger, annotated with the finger contour (dashed blue) and the characteristic wavelength (red). Subfigure (b) depicts a shear zone localization (red arrows) within the laponite birefringence bands (dashed green boundaries).

are observed to be stationary.

In the contour analysis for this experimental set we only did an intrusion perimeter and volume comparison as seen in figure 4.23. The intrusion volume over time is quite similar for both concentrations, while perimeter length increases more rapidly for the higher concentration laponite.

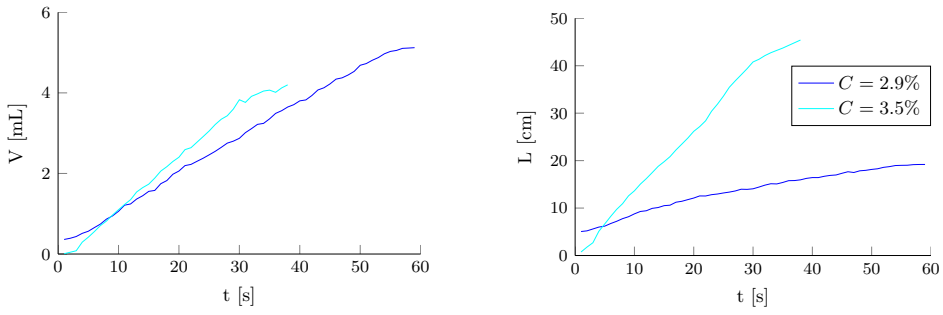

(a) Intrusion volume (b) Intrusion perimeter

Figure 4.23: Intrusion volume (a) and perimeter (b) as a function of time for different laponite concentrations.

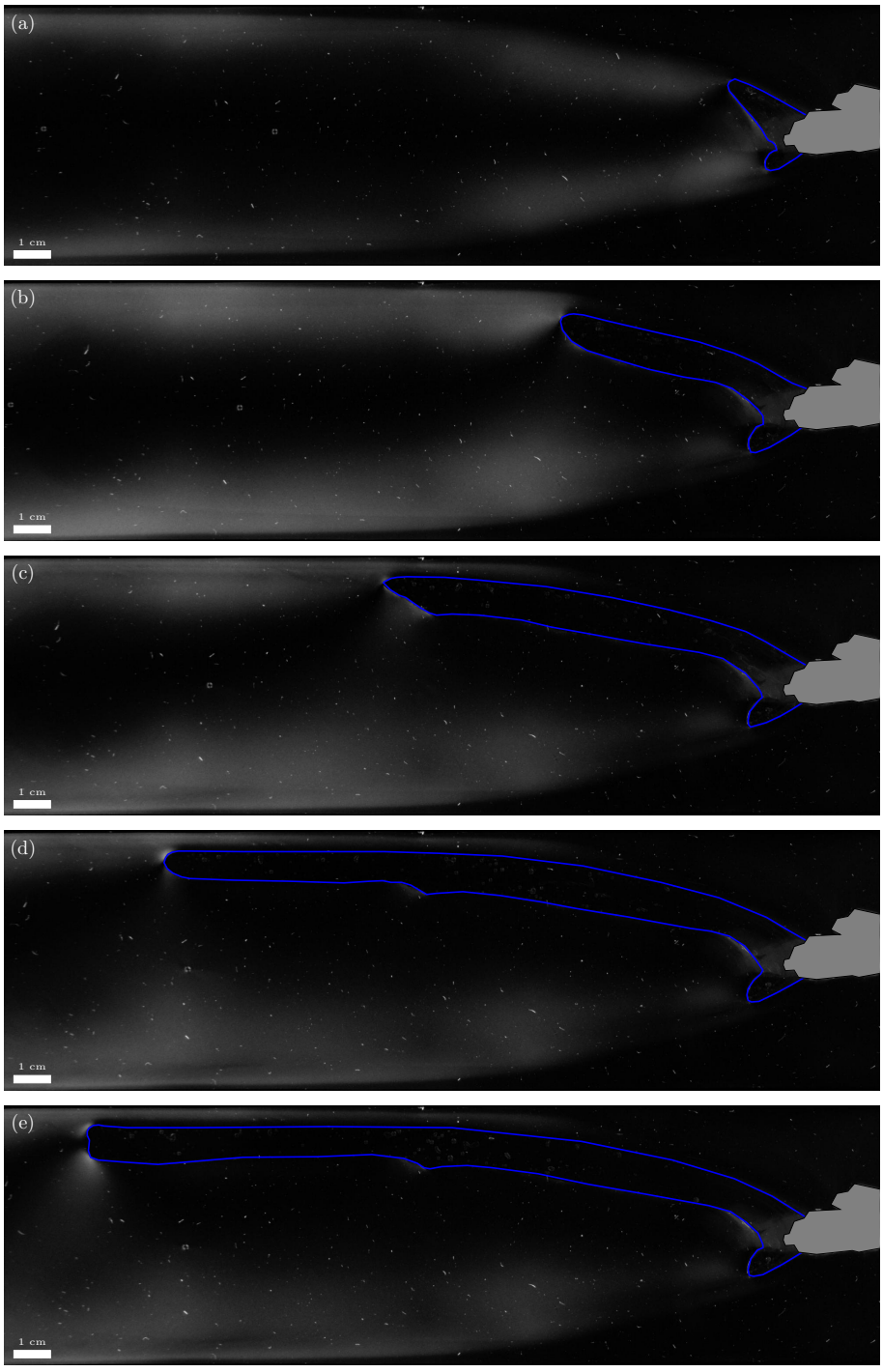

Figure 4.24: Selection of images showing the time development for experiment 14, $C = 3.5\,\%$. The time-step between the images is 8 s. Intrusion boundary in blue, inlet is gray.

4.3 Set 3: injected fluid dependence

In set 3 the intension of was to highlight the effect of changing the viscosity ratio between the laponite gel and injected fluid, using different fluids instead of changing the laponite rheology. The reason we do this is that the viscosity contrast is thought to be of important for the rheological response of the host rock during magma intrusions (see Rubin (1993)[30]). Only two experiments were performed and we only present observations from this set.

The two intrusion experiments composing set 3 used water (experiment 10) and oil (experiment 11) as injected fluids while other parameters were fixed. The fixed parameters were laponite concentration $C = 3.5\,\%$, waiting time $t_w = 10\,\text{min}$, and flow rate $Q = 10\,\text{mL}\,\text{min}^{-1}$. The aspect ratio varied slightly between the two with $\epsilon = 0.030$ for experiment 10 and $\epsilon = 0.026$ for experiment 11. The difference in aspect ratio is minimal, but the cell with the smaller aspect ratio has almost half the gap height H of the other which according to theory would promote elastic response in the matrix (see section 5.1.3.2 for validation of this claim). Despite multiple variables affecting the flow, the distinction between the two experiments is clear.

In figure 4.25, we see that the water intrusion makes a very thin fracture with an acute tip. Keeping in mind that the inlet is blocking most of the view, no initial blob can be observed. The fracture emerges from the inlet at a 50° angle going straight for the edge and clings to it. The fracture propagates at high speed towards the far end of the cell, reaching the laponite to air boundary in approximately 3 s.

After approximately 15 s the primary fracture closes and a second emerge at a 70° angle behind the primary. The secondary fracture follows the same path as the primary, until initiating a new fracture just before reaching the laponite to air boundary. The new path is parallel to the initial split angle of the secondary fracture and crosses the cell while bending.

The glass plates composing the cell in this experiment were poorly constructed and non-planar; in consequence the birefringence observed is caused by stress in the glass plates when clamped. Judging by particle movement, the laponite stays stationary for the entirety of the experiment, except in the proximity of the fractures.

In comparison, the oil intrusion in experiment 11, depicted in 4.26, produce two wide fingers with blunted tips, one tip filled by an air bubble. The fingers initiate from a small blob, making 10° angles with the cell centerline. The fingers are less stable in width than the experiments in set 1, and the primary finger narrows considerably at its tail, forming an eloping diapir-like shape. Just before the finger exits the view we can actually observe what we believe to be a small wake turbulence at the end of the

head of this eloping finger. In the secondary finger some branching occurs, with small new blunt tips developing behind the tip, rather than the tip front.

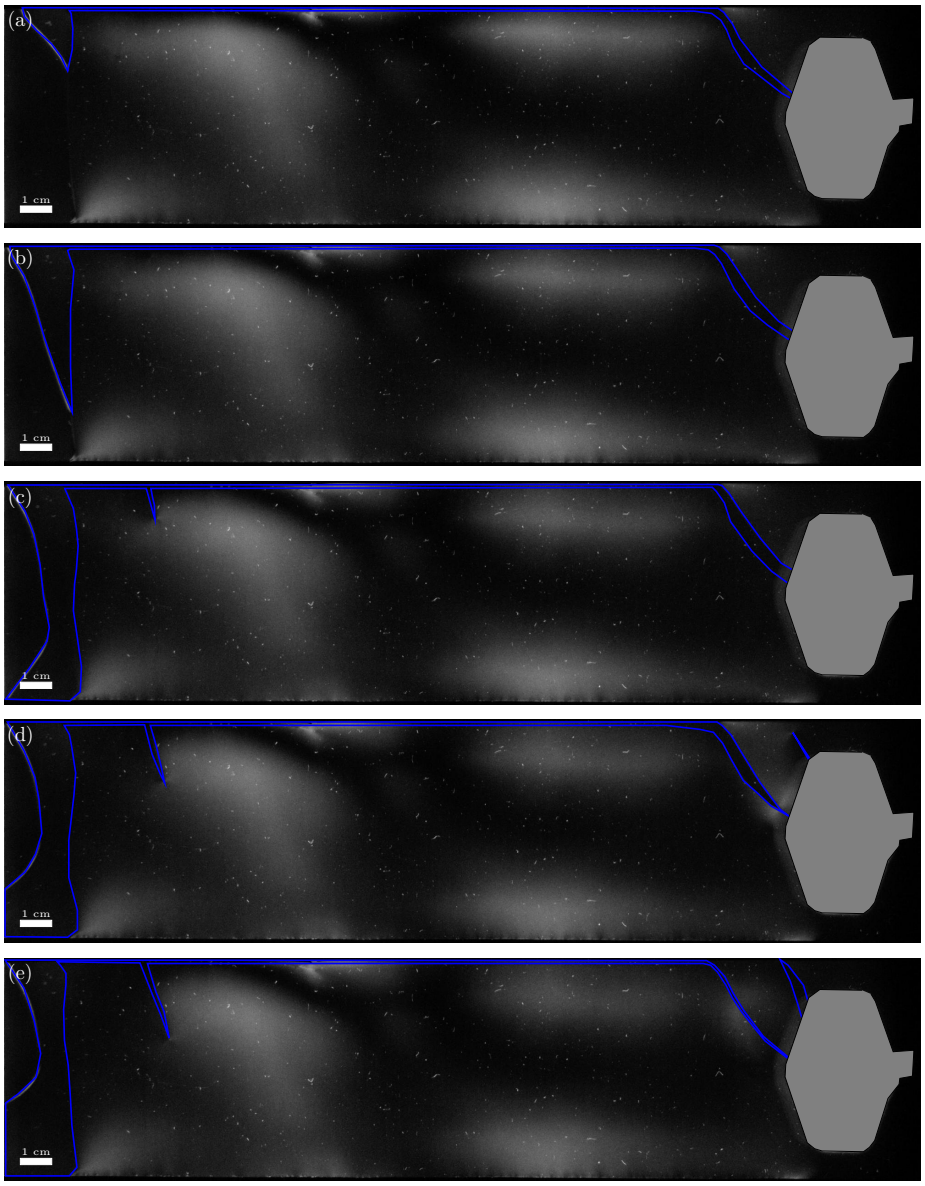

Figure 4.25: Selection of images showing the time development for experiment 10, with water as injected fluid. The time-step between the images is 10 s.

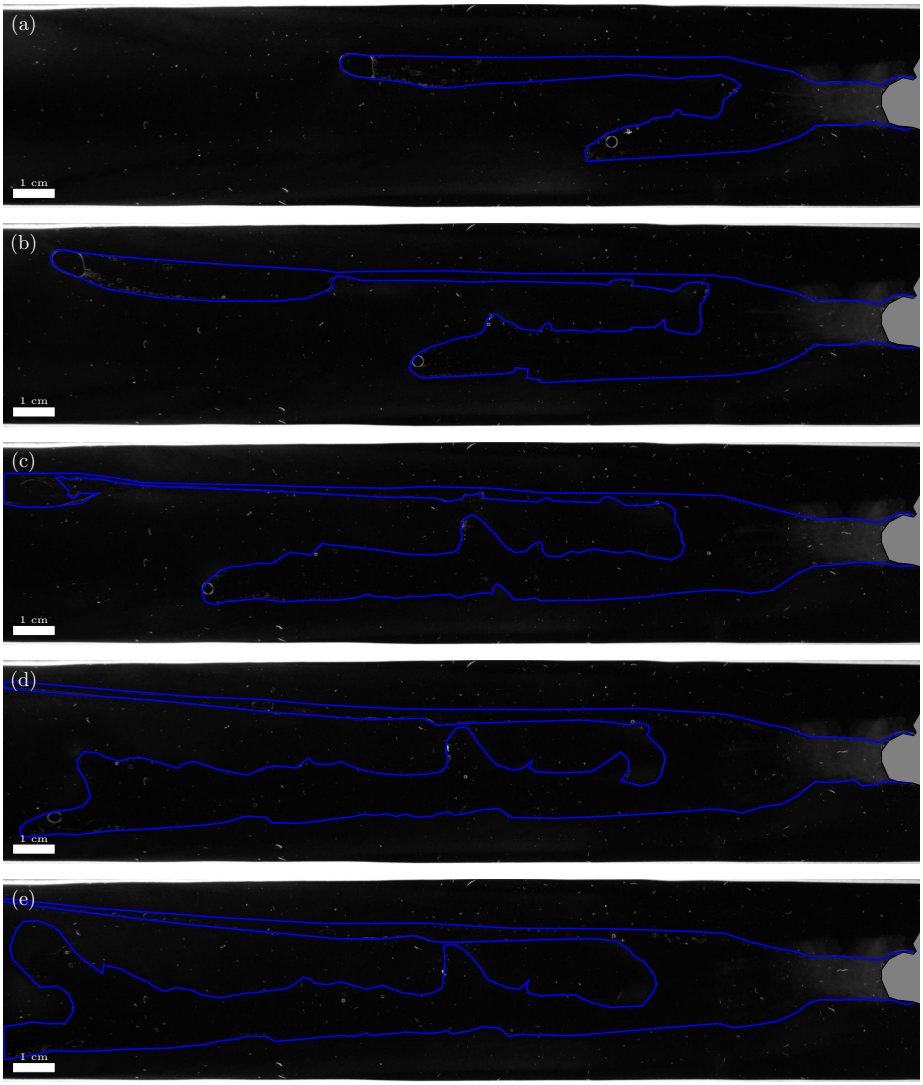

Figure 4.26: Selection of images showing the time development for experiment 11, with oil as injected fluid. The time-step between the images is 5 s.

4.4 Heterogeneities

As the experiment setup is a prototype we will not go into an in-depth display of the observed artifacts and heterogeneities, but instead focus one the most interesting heterogeneity, dubbed black holes, and the most prominent heterogeneity, bubbles.

4.4.1 Black holes

In some experiments we observe spherical black objects which themselves show no polarization, but in the laponite surrounding we can see a distinct lobe birefringence pattern. The black holes, as we named them, are depicted in figure 4.27 They are very distinct from the other particles in the flow which are white and show birefringence themselves, but not around themselves. The objects follow the laponite particle flow and the lobe pattern is observed to rotate or skew as the flow goes.

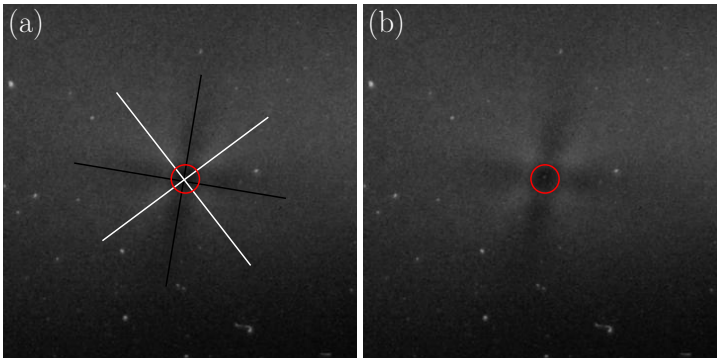

Figure 4.27: Images showing an example of the black hole heterogeneity. In (a) the intensity image is annotated with white stripes indicating the local birefringence intensity maxima surrounding the object, while black stripes indicate the local minima surrounding the object. In (b) we see the unaltered intensity image. Both (a) and (b) have a red circle marking the black hole object position.

4.4.2 Bubbles

We observe two main types of bubbles in our intrusion experiments, bubbles coming from within the laponite, and bubbles coming from the inlet. Both types of bubbles are seen to affect the results.

The bubbles within the laponite mostly stick to the separator frame on the cell edges, as seen in figure 4.6, causing a lubrication of the edge and gross alteration of the polarization patterns nearby.

The bubbles originating from the inlet will be a part of the intrusion and can be seen affecting the intrusion to matrix interface curvature. One example is the big bubbles in the initial blobs of experiment 1, see figure 4.1(a), which cause perturbations on the interfacial boundary. Another example is the bubble composing the tip of the primary finger in experiment 11, see figure 4.26(a) and 4.26(b), which makes the tip curvature suspiciously round and smooth in comparison with secondary finger.

Chapter 5

Interpretation and discussion

We start this chapter discussing the concept and method. We then turn the focus to the physical results and their interpretation.

5.1 Method validity and limitations

Since the method used is in development, we want to give a thorough evaluation of its validity and limitations, so that we can evolve the, at present, highly qualitative setup to a more quantitative solution, that can bring us the information we seek on stress-strain relationships in viscoelastic fracturing.

5.1.1 Observables: what do we actually see?

As mentioned in the results introduction, all observed features are some pattern of birefringence or polarization occurring within the cell, however the origin is not necessarily the same from feature to feature. This naturally calls for the questions: what do we see, and what are the underlying mechanisms? Asking and answering these questions are important to understand how to choose materials and optical setup in order to favor and enhance the relevant features, and to remove or reduce unwanted features. Knowledge of the nature of the observed patterns is also vital for correct physical interpretation of the results.

5.1.1.1 No polarization

To establish the discussion of what we see, we need to start with the background state — when nothing is observed. Since laponite is optically isotropic when unstressed and below a concentration of $C = 3.0\,\%$ (refer

section 3.3.2.3), no polarization will occur in the matrix and the light keeps its initial polarization when traveling through the cell. When it reaches the analyzer, which has a 90° angle with the polarizer, the light is completely blocked out and the background is perceived as black. At $C = 3.5\,\%$, laponite is observed to have a nematic state causing an optical anisotropy and birefringent properties [34]. However, we do not observe such a feature. According to the stress-optical rule the light retardation caused by the birefringence is proportional to the sample thickness [6], the retardation is what change the polarization of the light, and we infer that the gap height is too small for the retardation to be noticeable.

5.1.1.2 Bulk birefringence

Perhaps the most interesting polarization feature to discuss is the birefringence patterns shown in the bulk of the laponite, manifesting itself as a diffused pattern of varying intensity e.g. in shear zones, around fractures, and the lobe patterns forming around finger tips and inlet (see e.g. figure 4.12(b)). These features may be come from two mechanisms; particles aligning to the flow causing flow birefringence, and restructuring of the laponite gel network coming from the need to distribute stress causing stress birefringence [6].

The observation of the shear zone localization (see figure 4.22(b)) and the fact that no birefringence is observed in the laponite bulk in experiment 1, which is the only assumed pure viscous experiment, suggests that flow alignment plays a lesser role in causing birefringence for our case. This is also substantiated by the presence of similar birefringence in both flow and no-flow areas.

The absence of flow birefringence has its pros and cons. A gel can be considered a two-phase system; a gel network which is solid, and a liquid phase filling the gaps of the network. In our case we assume that the bulk birefringence is caused by the need for restructuring of the gel network to distribute stresses, in other words, a gel network is present whenever we observe this. Since the presence of a gel network is what gives elasticity to the laponite, we can deduce that laponite showing this kind of birefringence is elastic to some extent, and that the local birefringence intensities should correlate to the local stress magnitude of the stress distributed in the gel-network. However, stress is also distributed by flow inside the network. On one side the birefringence allows us to isolate information on the elastic stress component, on the other we have no information of the viscous stress component.

Stress is also distributed by deformation and destruction of the gel structure. In other words, as laponite is shear-thinning, we lose our stress feedback when the network breaks down.

5.1.1.3 Interfacial polarization

On the interfaces between laponite, olive oil, and air, we see a clear line, however varying in intensity spatially and temporally. Intuitively, since we see no birefringence within the oil or air, this is a feature of the boundary itself. The refractive indices vary between the materials with $n_{lap} \approx 1.34$ [27], $n_{oil} \approx 1.47$, and $n_{air} \approx 1.00$ [45], and we expect that the boundary will be curved in respect to the cell normal, dependent on e.g, local flow profile and interfacial tension between the materials. A curved interface between materials with different refractive indices would cause refraction and reflection of the incident light in accordance with Snell's law, resulting in the polarization we observe. The larger the difference in refractive index, the stronger refraction [37].

The surface tension between air and water is $\gamma_{air/water} \approx 72.86\,\mathrm{mN\,m^{-1}}$, between air and olive oil $\gamma_{air/oil} \approx 33.67\,\mathrm{mN\,m^{-1}}$ [19], and between olive oil and water $\gamma_{oil/water} \approx 16.42\,\mathrm{mN\,m^{-1}}$ [41]. Using water as a rough approximation substitute for laponite, since no accurate figures were found, one may argue that the higher surface tension values for the air-interfaces versus the oil-water interface would result in a stronger curvature at air-interfaces than oil-water. More curvature means a broader surface in which the incident light is polarized, and it is observed that air bubbles in our experiments have a thicker contour than the oil intrusions.

The intensity of the observed patterns is measure of how much light changes polarization state within the interface. Brewster's angle is an angle of incidence where light of a certain polarization is perfectly transmitted, leaving both refracted and reflected light linearly polarized. Using Brewster's law,

$$\theta_B = \arctan\left(\frac{n_2}{n_1}\right),$$

we can calculate the Brewster angle's for the different interfaces. We simplify the problem by only looking at the first curved boundaries the light will pass when traveling from the bottom of the cell and upwards, and get:

$$\underset{\text{lap}\to\text{air}}{\theta_B} = \underline{36.73^\circ} \qquad \underset{\text{oil}\to\text{air}}{\theta_B} = \underline{34.23^\circ} \qquad \underset{\text{lap}\to\text{oil}}{\theta_B} = \underline{47.65^\circ}.$$

The high θ_B of the laponite to oil interface, along with a relatively flat curvature normal to the cell plane, means that the angles of incident are

likely to be far from Brewster's angle. Conversely, for the air-interfaces the lower θ_B and stronger curvature suggest that incident angles are likely closer to Brewster's angle. This can explain that air-interfaces show higher intensities than the laponite to air interfaces.

For experiment 10 (see section 4.3), where we inject water, the contour of the intrusion is vague. This is logical considering the above discussion and the fact that the interfacial tension between oil and water is vanishing, and that they have practically the same refractive index.

One should also take into account that shear and compressional stresses are present in the laponite close to the oil intrusion. This means that the laponite gel network close to the interface is likely to show some stress birefringence. It is interesting to note that after an experiment was completed, and the cell was disassembled for cleaning, the laponite gel seemed to hold the boundary structure imposed by the oil intrusion after the oil was poured out, while the bulk laponite was slow flowing. Considering that the laponite had experienced recent shear, especially at the boundary, it might be that a forced structural alignment on the boundary has helped in formation of PPO-bonds (see figure 3.7(b)) and a speeded regeneration occurred.

We find it likely that the polarization at the laponite-oil interface is likely caused by a combination of curvature polarization and induced birefringence, however we believe that the curvature polarization is more prevalent, due to the often high contrast to nearby bulk birefringence.

5.1.1.4 Laponite particle birefringence

Partially hydrated laponite particle clusters are observed as bright spots. As these particle clusters will consist of aggregations of laponite platelet stacks, exemplified in figure 3.6, their observed birefringence can be explained by an ordered molecular structure which show optical anisotropy, so called intrinsic birefringence. Some of the rod-like laponite particles are seen rotating when close to the cell edges, their birefringence intensity changing as they rotate. The same can be seen when rotating optically anisotropic crystals in a polariscope. Thus, we deduce that it is intrinsic birefringence we observe in this case.

The irregular size, shape and distribution of the particles, along with the varying intensity they show, makes them unsuitable as seeding particles for PIV, as confirmed by our basic PIV-tests (see section 4.1.2.3). In addition if PIV is attempted with proper seeding particles, laponite particles will be noise that complicate the extraction of particle trajectories. Thus, in future

experiments such particles should be avoided altogether through filtering, or by choosing other materials.

5.1.1.5 Black holes

The black hole heterogeneity, described in section 4.4.1, is seen as a spherical object which itself show no polarization features, but the bulk laponite surrounding the object has a distinct lobe birefringence pattern. Since it is observed to be optically isotropic, and no polarization on the boundary, it is likely that the object has similar refractive index as laponite, so that little refraction or reflection occurs. The strong lobe patterns around it, suggest that the object is rigid and translates stress rather than absorbing it by deformation, similar to what is seen for rigid spherical inclusions in simple shear flow (reference??? Marcin's course?).

A plausible candidate for these black holes are glass particles. In preliminary experiments, glass particles were mixed with the gel as seeding particles for PIV. The use was discontinued before the experiments presented in the results, as the available particles were much denser than laponite, and sank to the bottom of the cell while the gel aged. The glass particles used were dust-like and similar in appearance to the laponite used, so it might be that a few glass particles has contaminated the laponite container without our knowledge. The same measuring spoon was used when weighing the substances and it is likely that the spoon was not properly cleaned between all weighings. Thus, one may argue that rigid particles are unsuitable as seed particles for combined PIV and polariscopy as they seem to produce significant birefringence in the gel. It also emphasizes the importance of cleanliness and following protocol.

5.1.1.6 Parasitic birefringence

The glass used in the Hele-Shaw cells was standard soda-lime glass. Some glass sheets were poorly prepared, as they were cut and annealed by myself, an unexperienced glass worker. This resulted in a slight unevenness in the sheets which caused strong birefringence patterns when the cell was clamped e.g figure 4.25. Such parasitic birefringence makes it hard to distinguish the birefringence patterns induced by the intrusion, and one should therefore take choose glass that is designed to show little birefringence when stressed, and also make sure that the sheets are properly cut and annealed. Glass sheets with parasitic birefringence is relatively easy to identify by placing an empty test cell, fully assembled and clamped, under a polariscope.

5.1.1.7 Reflections

Polarized reflections on the glass surfaces was limited significantly by enclosing the experiment in a box with the insides painted in matte black. However, the use of transparent plastic tubing and inlet compromised the light barrier by acting as an optical fiber, providing a path for outside light to enter the cell. This light caused significant polarized reflections near the inlet, which clouded the picture of what happened below. Choosing opaque black matte materials or coatings on the experiment parts inside the box would remove this noise.

5.1.2 2D mechanics approximation

Magma intrusions are three-dimensional processes. When reducing the problem to two dimensions certain features are inhibited and there is a considerable loss of information, however, for our purposes, this is trumped by the ease of observation and data acquisition using a transparent Hele-Shaw cell.

Another advantage of the quasi-two-dimensionality of the Hele-Shaw cell is that, assuming low deformability of the cell, the narrow gap height and wide surface area restrict strains to occur in the two dimensions of the plane. The stress is not zero perpendicular to the plane, as fluid pressure, being a scalar, has no direction. However, if the stresses perpendicular to the plane are too small to noticeably deform the cell, they should be of little importance for the results of the experiment. In other words, we can assume plane strain conditions.

No turbulence is observed for low flow rates, while high flow rates show small turbulence in isolated areas. Thus, the gel flow perpendicular to the cell plane can be considered laminar for low flow rates, and mostly laminar for high flow rates. The particle flow in the bulk laponite suggests that the velocity profile in respect to the cell normal is similar to that of a strongly shear-thinning fluid, except for slow flow in viscous end-members (see section 4.1.2.1). Such a velocity profile would result in high shear close to the glass plates, destroying the gel structure and induce self-lubrication, making the laponite in the low-shear areas move like a plug. With this reasoning we can assume that plane strain conditions holds for the bulk laponite. In fact, in the optical rheometry studies of stagnation flows in polymer melts by Soulages (2007)[39] a thin film of silicone oil is used in the experiment cell to provide lubrication. In Soulages's experiments the intrinsic velocity profiles of the polymer melts are parabolic, so lubrication

is needed for the two-dimensional approximation to hold, and to avoid unquantifiable birefringence from a three dimensional flow.

The discussion of the interfacial curvatures in section 5.1.1.3 argues that the oil-laponite curvature is relatively plane perpendicular to the cell, while air-interfaces are more rounded. This suggests that the plane strain approximation holds for the oil-laponite interfaces as well, but perhaps not around air bubbles.

If plane strain conditions are considered, and we ignore the perpendicular stresses, we can describe the stress and strain state inside the cell with tensors of dimension 2, and the problem is truly reduced to two dimensions. This means that similar numerical, or even analytical, models are relatively easy to develop, and a combined approach can bring further insight to the problem. That is, if we are able to extract the correct stress and strain data in the first place.

5.1.3 Variable control

The experiments conducted for this thesis were prototypes, and performed mainly to provide proof of concept. Therefore, no real discussion on variable control was done until after the experiments. Nevertheless, the rough prototyping as well as the literature review gave valuable insight into what variables should be controlled in an ideal experiment. Many variables are found to affect results, so future work would need a robust parameter study.

An ideal experiment has only one variable of interest — an element that is varied and tested. All other variables should be held consistent between experiment runs. Only through variable control can one safely assign an observed response as an effect of changing a certain variable. Proper variable control removes ambiguity from the conclusions of the experiment and is imperative when comparing to former work. If the model is unaffected by a variable, it can be removed from the equation and neglected, and the model is thus simplified. Choosing the right variables to strip away is the essence of creating an idealized model of a physical system.

The independent variables that are identified in our experiments are discussed below, while the dependent variables, i.e. the observables, have already been discussed in section 5.1.1.

5.1.3.1 Cell deformability

Lemaire et al. (1991)[15] found in their experiments that the deformability of the cell affects the morphology and rheology in an intrusion experiment. Their results tell us that the critical pressure for viscoelastic fracture to

occur, P_{VEF}, have the following relationships with parameters concerning cell deformability (see equation (2.2)):

$$P_{\text{VEF}} \propto E^{\frac{2}{3}},\ e^2,\ L^{-\frac{7}{3}},$$

where E is the elastic modulus of the glass plate, e the plate thickness, and L the span length of the plate. This is of course based on their experiment, and will also vary with e.g. the nature of clamping or support for the glass plate, but we see that low deformability (large E and e, and small L) will give a high critical pressure P_{VEF} and favor viscous fingering, while high deformability (small E and e, and large L) will give a small critical pressure and favor elastic fracturing.

When considering deformability for cells used in photoelasticity measurements, low deformability is always desired. Large enough deformation of the glass in the cell walls will induce parasitic stress birefringence as discussed in section 5.1.1.6. Thus, all glass plates should be tested for parasitic stress birefringence in e.g a three point flexural test, using a measured maximum injection pressure as the point load.

The clamping of the glass sheets in our experiments was done by several uniformly spaced screw clamps with circular heads made of rigid plastic (see figure 3.2). This means that the clamping was not uniform and there was a sharp leverage point at the rim of the screw clamp heads. A perhaps better solution would be a frame clamp ensuring uniform clamp pressure, and a soft padding, e.g. rubber, between the glass and clamp to remove sharp leverage points. The padding would also reduce risk of scratching the glass.

Another important discussion point of cell deformability is that ideally one would like the cell geometry to change as little as practically possible to ensure constant boundary conditions.

In conclusion the glass sheet quality, geometry, and clamping method, must be chosen so that the glass has low enough deformability to not produce parasitic birefringence or change the cell geometry during experiments. This should be done after materials and experiment geometry are scaled to the relevant natural process.

5.1.3.2 Cell geometry and boundary conditions

Magma intrusion processes have a large range of spatial scales (see sections 2.1.1.2 and 2.2.1), making it hard to assess the natural bounding geometry and properly scale the problem according to Hubbert's similarity criteria[10].

In our experiments the cell geometry was based mainly on the desire to produce single fingers with straight trajectories in a linear cell to be able to focus on the process zone around the crack tips. This reasoning was based on similar experiments in Newtonian fluids (e.g. Lindner and Wagner (2009)[17]) and turned to be a flawed reasoning for strong shear-thinning and viscoelastic experiments. As we see in most of our results the trajectories are seldom straight and we get several fingers or fractures from splitting and branching. The bounding conditions were chosen to restrict the intrusion direction, with three confining walls giving a no-penetration Dirichlet boundary condition, and a free boundary towards the outlet side of the cell. Nevertheless, the experiments were rich in results and served their purpose as prototypes.

Considering Lemaire et al.'s discussion on cell deformability and the resulting equation (2.2) we get the following cell geometry dependencies for the critical pressure for viscoelastic fracture to occur:

$$P_{\mathrm{VEF}} \propto a^{\frac{1}{3}},\ L^{-\frac{7}{3}}$$

where a is the cell gap height ($a = H$ for our cells), and L is the span length of the glass plates. In our case the ratios would be different as the width W and length L are different, and since $W < L$, W will be the most relevant length scale of the two. Arguably, the confining geometry is found to significantly affect the morphology and rheology of the experiment, meaning a reduction to two dimensions makes proper scaling difficult.

Referring to the previous discussion on observables (section 5.1.1) and two-dimensional mechanics approximation (section 5.1.2), the cell thickness must be chosen in such a way that the plane strain assumption is valid, and the contrast of the observables is acceptable. Thinner cells would lead to poor interfacial contrast and less light retardation from birefringence, while thicker cells would lead to three-dimensional mechanics. So a trade-off has to be done to fit the experiment geometry to the restrictions.

During experiments we want the injected fluid to push the matrix material rather than slipping in between the cell edges and the matrix. We see that in our experiments (e.g. figure 4.4(a)) the injected oil has a tendency to cling to the walls of the separator frame, so that the matrix is displaced instead of being intruded. The shear-thinning nature of laponite is not favorable in this aspect as the the laponite close to the edges will experience higher shear stress than the bulk, causing the gel structure to break down and lowering the yield stress. The intrusions are not observed behaving like this in respect to the glass sheets.

In some experiments, e.g. experiment 6 (see figure 4.6), we experienced bubble formation on the cell edges. Bubbles were not observed before some

time had passed, and it is likely that the mixing introduced a laponite gel oversaturated with air, and that this air easily nucleated on the separator frame edges. The bubbles caused disturbances in the bulk birefringence and is assumed to lubricate the edges, so we decided to remove them by degassing the samples prior to injection.

Inlet geometry was chosen based on similar experiments, however the injection hole does not fit the natural problem of a perturbation on a magma to host-rock interface that evolves into dykes and diapirs. An inlet setup like the original Saffman-Taylor viscous fingering experiment [35], where the initial fluid to matrix interface was flat, would be more similar to the natural problem.

The outlet geometry had little influence on the boundary conditions. The free laponite to air boundary was of some distance to the outlet, and the outflow of air was unrestricted.

Based on what is discussed above, we argue that a radial horizontal cell with a central hole inlet might be better for further study of splitting and branching properties of viscoelastic fracturing, as side wall effects are removed from the equation. Such experiments can possibly be used for comparison with radial dyke swarms as seen in figure 2.3. For study of single fingers and fractures, and analog experiments for ascending magma, a wide linear cell with vertical alignment, free top boundary, and a bottom inlet like the Saffman-Taylor experiment might fit our purposes. The buoyancy of the injection liquid can be controlled by carefully selecting the density ratio between the matrix and injection fluid, and will give us the directional restriction we want. A perturbation can be made on the fluid to matrix interface in the center of the cell so that the initial fingers evolve from this point.

5.1.3.3 Material selection and properties

The results show that laponite is indeed a plausible material for simulating viscoelastic deformation. No control experiments were done to establish reproducibility, however the results seem to follow expected trends, in contrast to the reported unwieldy behavior of laponite (see Ruzicka and Zaccarelli (2011)[34] for references).

The selection of laponite gel as a host rock analog was not based on a proper scaling analysis, but its ability to provide a wide range of different rheologies by adjusting the concentration, waiting time, and ionic strength. We now that rock and laponite both show time-dependent shear-thinning (reference??? Ranalli?), however scaling such behavior might prove very difficult.

For all purposes, if its a solely viscoelastic intrusion experiment or a scale model of magma intrusion, a solid rheometry analysis on all materials must be done prior to experiments. Our rheometric study was very basic and not fit to fully describe non-Newtonian rheology.

Rubin argued that host rock needs a viscosity of 11 to 14 orders of magnitude higher than the intruding magma in order to behave as essentially elastic. For dike thickness to length ratios less than 0.1 he found that the required viscosity contrast was of 6 to 8 orders of magnitude. Our rheometry results on laponite (concentration $C = 3.5\,\%$, waiting time $t_w = 10\,\mathrm{min}$) and water show a viscosity contrast of 4 orders of magnitude (using the gel viscosity of laponite), and in experiment 10 which had the same material parameters we observed very elastic-like behavior (see section 4.3).

The density parameter is mostly relevant for intrusion experiments featuring buoyancy, were it plays a vital role in controlling ascent rate, however if there are large density differences between the injection fluid and the matrix in a horizontal cell, inertial effects may induce a Rayleigh-Taylor instability in addition to the instability related to the rheology difference.

Compressibility is seldom addressed in intrusion experiments although several researchers use air as their injection fluid when exploring hydraulic fracturing processes e.g. Hirata 1998[8]. Personally I would argue that there is a fundamental difference between hydraulic and pneumatic fracturing, and that using high compressibility injection fluids may induce specific artifacts that are not seen for incompressible fluids. In Hirata's defense they continuously measure the injection pressure to ensure its constancy. However, as we have seen in our experiments (e.g. experiment 8, see figure 4.7), some elastic cracks close at the tail, producing an eloping intrusion. Even though rigid pressure control is done at the inlet, it is not possible to avoid compression inside such intrusions. In our experiments compressibility is not relevant, except when considering fast moving and deforming air bubbles, which are undesired heterogeneities.

Interfacial tension is another parameter that is often neglected when discussing the resulting morphology and rheological nature of intrusion experiments (e.g. Lemaire et al.). As we have observed in our experiments and discussed in section 5.1.1.3 the interfacial tension is of vital importance to the curvature and thus morphology of the intrusions. Lindner and Wagner (2002, 2009) [16, 17] gives an introduction to the effects of interfacial tensions in viscous and viscoelastic fingering.

We did not concern ourselves with miscibility or chemical reactivity in our experiments, however for magma intrusions they are both important aspects. In experiment number 10 we used water as injection fluid and water

is miscible with laponite. We had no observations that we can assign as effects of miscibility, but the propagating rates in this particular experiment were large, so it is likely that the water and laponite had too little time to mix. Both miscibility and chemical reactivity would complicate the physical problem we want to research, and should be avoided if they are not the variables of interest.

As we want to use our experimental concept to determine stress-strain relationship through combined photoelasticity and PIV we need our materials to be suitable for both. We argued in section 5.1.1.2 that we could only extract the elastic components of the stress field from the observed bulk birefringence, and we saw no fringe patterns which could enable us to determine the magnitude and directions of the stresses. The lack of fringe resolution could perhaps be addressed using fringe multiplication techniques (see e.g. Post (1970)[24] or Ramesh (2000)[25]), which would call for complex optical setups. The lack of viscous stress observation could be derived from PIV if the constitutive relation of the matrix material is known, and maybe it is an advantage that they are separated. However, this discussion is beyond the reach of this thesis and is left for others to explore. Nevertheless, if photoelasticity is to be performed an in depth study is needed to decide the aptness of the materials for such analysis. For PIV experiments, the removal of the laponite particles, as discussed in section 5.1.1.4, should be enough for the laponite to be a suitable material.

5.1.3.4 Sample protocol

Our sample protocol (see section 3.3.2.7) seems to function quite well. We did not follow the recommendations from Ruzicka and Zaccarelli on using a glovebox to prepare samples, filtering the samples or drying the laponite to remove absorbed water, but in spite of these lacks we got results that showed consistency. There is however one thing that should be changed in our sample preparation and that is the mixing apparatus. A magnet stirrer is not designed to produce high shear, and the lack of high shear leads to the formation of the partially hydrated laponite particles we see in our experiments. Ideally we would use a mixing apparatus designed for high shear mixing, e.g with radial flow impellers [9].

We introduced degassing as a means to remove bubbles in our laponite, and it was a success for laponite concentrations of $C = 3.0\,\%$. For concentrations of $C = 3.5\,\%$ the gelation process is so rapid that degassing resulted in a foam formation, and we degassed the water prior to mixing instead for these samples. We found that using plastic containers when degassing led to bubbles sticking to the container walls, and the same

occurred if the stirring rod from the magnet stirrer was left in the container. This problem was solved using glass beakers and removing the stirring rod.

5.1.3.5 Fluid injection flow control

We used continuous constant flow rate in our experiments, while in magma intrusions the flow is reported to be controlled by constant pressure, i.e. the effective pressure caused by magma buoyancy, and flow is not necessarily continuously but batch-like [30, 33]. This means that the rate of deformation in our experiments is proportional to the flow rate, while it in the natural process rather is controlled by the time under load. Thus, if one seeks to simulate magma intrusions, the injection flow should be pressure controlled. Another recommended improvement from our setup is continuous monitoring of the pressure and flow rate by sensors separated from the actual flow control.

5.1.3.6 Optical setup

The first step towards a successful image analysis would be to get the best possible raw imagery. This is achieved by the non-trivial task of choosing an optical setup that shows the observables that are desired in clear contrast to those that are not.

Validity, limitations and improvements

As we did not follow an idealized optical setup procedure like the one listed below (section 5.1.3.6), our optical setup was of the simplest kind and not fit for neither optical rheometry nor particle image velocimetry. We did, however, manage to extract qualitative data from both polarization features and particle flow.

To address the specific challenges and accomplishments regarding the optical setup that we experienced during our experiments, we will start with the camera itself. We did adjust the camera settings to best fit our needs (see section 3.2.2) and the resulting images were of reasonable contrast, however the temporal resolution, as in frame rate and shutter speed, was to low and we were not able to adequately extract highly dynamic features like e.g. fast propagating intrusions and turbulent particle flow.

We had large difficulties tracking the particle flow, partly because of the variation in particle intensity (see section 5.1.1) and birefringence noise (see section 4.1.2.3), but also because of the lack of time resolution as described above. The slow shutter speed caused smearing of fast moving particles

and the frame rate was so low that even slow flowing particles were able to move several times the mean particle distance between frames.

A challenge we did not overcome in our image analysis was to track the injection fluid to laponite matrix interface. The interface was easy enough to discern for the human eye, but not so distinct that we could easily extract it from the images. The fact that the interfaces, particles, and the stress birefringence is observed because they polarize light in some way suggests that we should use another approach to contrast our interface from the others. As argued in section 5.1.1, an interface between to materials of different refractive indices and interfacial tension will cause polarization. Thus, the interface polarization is hard to remove if we do not use miscible materials with the same refractive indices, which might not be desired based on the strong rheological parameter dependence on interfacial tension (see e.g. section 2.3.1).

An alternative solution is to use different colored materials for intrusion and matrix, but contrasting color difference and transparency of liquids might be hard to achieve simultaneous considering the experiment takes place in a polariscope. Our proposed solution is the addition of unpolarized image acquisition, simultaneous to the polarized image acquisition. This can be done in many ways. A second camera is an obvious alternative, but that will call for a setup for synchronized trigging. Synchronized trigging of two cameras is not to difficult to do, but there are also self-synchronizing alternatives e.g. stereographic setup using beam splitters or mirrors with a polarizing filter only on one side. This way the captured image will have two parts, one polarized and one not. However, this solution will effectively halve the available spatial resolution of the camera. We will not argue that one of these solutions is more suitable than the others, they all have positive and negative sides, and they will all exhibit slight stereographic effects.

In our experiments we observed that the thin fractures patterns seen under polariscope were not visible when inspected with the naked eye, so another benefit with the addition of unpolarized image acquisition is that we have a reference image for comparison.

Lastly, a setup detail with potentially damaging effects is the choice we made on fluorescent lighting which produced considerable heat. Since heat can induce viscosity changes, athermal lighting is imperative. We solved the problem by turning the light on just before the experiment was initiated, a ventilator fan to cool down the light, and temperature measurements before and after the experiments. However, the restrictions on switching the light on and off is a nuisance when preparing camera settings and checking polarizer alignment. It also lead to a few discarded experiments as the light was off when the experiment started.

Idealized setup procedure

For proof-of-concept our simple setup was fitting, however, if we want to achieve the aim of a complete stress-strain analysis of complex viscoelastic and shear-thinning rheologies a more thorough approach is needed. Paraphrasing Fuller (1995)[6] the following sequence of successfully choosing an optical technique and setup is proposed:

- First and foremost one needs knowledge of the desired microstructural information to be extracted, and its relation to the mechanical and dynamical properties one seek to explore. Our discussion on the observables and their meaning in section 5.1.1 is a humble start, but a more in-depth study is needed to fully understand the observables' connection to the underlying mechanisms.

- When we know our desired observables, the type of interaction between light and matter must be correctly chosen so that the desired information can be extracted.

- Then an optical technique should be chosen, motivated by its ability to measure the light-matter interaction, its sensitivity, and dynamic range.

- Once the optical technique is selected, the arrangement of optical elements required to perform the desired measurement must be designed. This involves not only selecting the elements themselves and calibrating them, but also choosing their alignment.

- Finally, a proper interpretation of the observables will depend on one's ability to correlate the measurement to the sample's microstructure or microstructural response.

5.2 Physical interpretation

The interpretation of our results starts with identifying the end-members of the different experimental sets, and discussing the major trends and relationships seen here in terms of background laid out in the introduction. We then turn our focus to the intermittent behaviors, before we suggest a rheological categorization of the results.

5.2.1 Effect of varying matrix rheology

In sections 4.1 and 4.2 we observed that the intrusion morphologies were dependent on the laponite gel waiting times t_w and laponite concentrations C.

The morphological end-members of the experiments in set 1 and 2 show us that for short laponite waiting times or low concentrations, the injection of oil produces wide and rounded conduits. Conversely for long laponite waiting times or high concentrations, the oil injection produces thin and sharp conduits.

According to our study on morphological behavior in hydraulic fracturing (section 2.2.4) and viscous fingering (section 2.2.5) this suggests that laponite behaves more elastically for long waiting times and high concentrations and more viscously for short waiting times and low concentrations. This fits with the laponite rheological behavior we know from section 3.3.2.

Based on the morphology and flow studies in sections 4.1 and 4.2 we have identified several behaviors characteristic of the viscous and elastic end-members.

5.2.1.1 Characteristics of viscous end-members

The following characteristic behaviors for injection of oil into laponite are identified for the viscous end-members:

- The finger curvature is smooth and round, with wide fingers and rounded concave tip shapes.
- The finger propagates along the centerline of the cell and no tip-splitting is observed.
- The intrusion volume increases linearly with time.
- The intrusion perimeter increases smoothly with time, with the perimeter increase rate decreasing with time.
- The cross-sectional velocity profile in the far-end velocity field is parabolic-like.
- The tip velocity is slow.
- No birefringence is observed in the bulk laponite.

These characteristics fit well with what we would expect for a viscous end-member. The rounded curvature, wide fingers and rounded tip shapes are all well-known from viscous fingering theory and experiments in Hele-Shaw cells (2.2.5). For comparison it is established that Newtonian Saffman-Taylor fingering, described in section 2.2.5.2, produces similar shaped fingers. We know from section 3.3.2 that laponite has a complex non-Newtonian rheology, however for the short waiting times in the viscous end-member the gel network structure has had little time to form, and the low concentrations means greater mean particle distance, making it harder for the laponite particles to bond [34]. This supports a near Newtonian rheology for the viscous end-member.

For such fingers the width and curvature is controlled by the competition between capillary forces, seeking to stabilize the finger to matrix interface, and the viscous forces from fluid pressure, seeking to push the finger[1]. The flow rates are small in these experiments and the interfacial tension, a vital part of the capillary forces, is relatively high at $\gamma_{air/oil} \approx 33.67\,\mathrm{mN\,m^{-1}}$ [19], which would explain the round and stable fingers. The absence of finger tip splitting and the central trajectory is a result of the same interplay[17].

The volume and perimeter behavior are basically different traits of the same phenomenon. Since the finger is stabilized by the dominating capillary forces, the ideal shape is round, and as the round shape expands, the volume increases proportional to the flow, while the bounding surface or perimeter increases proportional to $1/r$, where r is the blob radius.

The described parabolic-like cross-sectional velocity profile, sketched in figure 4.16), is a well known characteristic of Newtonian viscous flows in circular pipes, see figure 2.6, and similar velocity profiles are shown for rectangular conduits [9]. The parabolic shape of the cross-sectional velocity profile is the result of the linear relation between the viscous stresses and the strain rate for Newtonian fluids, and it will be similar for a near-Newtonian fluid.

For viscous fingering the tip velocities are inversely proportional to the relative finger width, the finger width to cell width ratio, leaving also the slow tip velocity a result of the interplay between viscous and capillary forces[36].

The lack of birefringence in the bulk can be seen in relation to the discussion on the laponite bulk birefringence in section 5.1.1.2 where we inferred that the we most likely only observe the birefringence as an effect of elastic stresses in the gel network, which has negligible presence in the viscous end-member as argued above. Since the concentration is just below the what is needed for transition to a nematic structural phase[34], it is reasonable that we do not see any flow birefringence from particle alignment.

5.2.1.2 Characteristics of elastic end-members

The following characteristic behaviors for injection of oil into laponite are identified for the elastic end-members:

- The finger curvature is angular and rough, with thin fracture-like fingers and sharp convex tip shapes.
- The finger splits at oblique angles to the cell centerline, bending strongly towards the cell edges as it propagates, when reaching the edges the finger has a tendency to cling to the cell edges.
- The intrusion volume increases stepwise linearly with time, the increase is thus discontinuous.
- The intrusion perimeter first increases roughly linear with time, then has an abrupt increase and thereafter continues increasing, albeit with the perimeter increase rate increasing with time.
- The cross-sectional velocity profile is similar to a flattened parabola.
- The tip velocity is fast.
- Strong bulk birefringence is observed along the edges and in proximity to fractures and flow.
- Multiple very thin fractures are observed in the laponite bulk.

The characteristics of the elastic end-member fit well with what we know from hydraulic fracturing theory (section 2.2.4). As we would expect from the literature study of laponite, the long waiting time of the elastic end-members, and high particle density for high concentrations, allows for a gel network to generate, the strong ionic bonds in the network giving elasticity to the laponite.

The rough angular shapes of the curvature, fracture-like fingers and sharp convex tip shapes are morphological traits of elastic hydraulic fracturing [5]. To produce a hydraulic fracture in the laponite the fluid pressure in the intrusion must be sufficiently larger than the ambient effective stress so that the minimum principal stress becomes tensile and overcomes the tensile strength of the laponite gel network. As we use constant flow rates, the fluid pressure will increase until reaching the yield stress limit and tensile fracturing occurs. As the initial intrusion blob expands we see thin incipient fractures surrounding the blob. The fluid pressure continues to grow and will overcome the gel compressional ambient

pressure keeping the thin fractures closed. The fractures will open and the fractures propagate.

The stepwise volume increase and abrupt change in perimeter length (figure 4.11) indicates a pressure building up until the yield stress limit is reached, and fracturing occurs. The coeval occurrence of two suddenly propagating fractures, as seen in figure 4.7(c), substantiates this line of thought. However, for the abrupt change in volume, one would expect a pressure build-up which would mean a deceleration of the flow rate prior to the fracturing. Such a flow rate decrease is not observed in the corresponding flow rate plot in figure 4.9(d). This possibly suggest an instrument error has occurred during the intrusion, and we did experience erratic behavior with the syringe pump in preliminary experiments not presented in this thesis. Nevertheless, the sudden fracturing is similar to predicted hydraulic fracturing behavior [5, 20].

The flattened parabola shape of the cross-sectional velocity profile is inferred from observation of particle flow (see figure 4.16), and it is found to correlate with the velocity profile derived from PIV (figure 4.20). The flattened parabola shape is indicative of strong shear-thinning behavior and is a well known characteristic of such fluids [9].

We know that aged laponite show a strongly shear-thinning and thixotropic rheology (see section 3.3.2.5), and the observation of the fractures clinging to the cell edges supports the assumption of shear-thinning. The flat parabola velocity profile, as well as the birefringence banding seen at an early stage in figure 4.7(a), indicates that shear is most prominent at the cell edges, rapidly decreasing inwards. The shear-thinning effect would thus destroy the gel network in the laponite around the edges, causing the bulk laponite to move as a plug. After some time, the laponite gradually provides less resistance to flow, and the birefringence bands slowly diminish. Intuitively, the oil intrusion would follow the path of least resistance, which explains why the fingers tend to cling to the edges as seen in 4.7(e).

Initially the tip shape of the both primary and secondary fracture is acute convex as shown in 4.7(c), and the tip velocity is very fast, both indicative of hydraulic fracturing. As the fractures start clinging to the edges a slower propagation is observed, wider fingers and the tip shapes turn from acute convex to acute concave, a predominantly shear-thinning trait. This is in coherence with the assumed destruction of the gel network, and the resulting shear-zones. As the primary and secondary finger ventures into the shear-zones it experiences a different rheological response from the laponite, and the elastic fractures evolve into viscous fingers with a shear-thinning effect.

The strong bulk birefringence in the elastic end-member case supports the hypothesis that we are only able to observe the birefringence effect from elastic stresses, as argued in section 5.1.1.2.

5.2.1.3 Transitional behavior

At waiting times in between the viscous and elastic end-members we observe coeval viscous and elastic morphology and behavior, as well as shear-thinning effects. The images in figure 4.6 are good examples of this hybrid behavior. In this experiment the waiting time $t_w = 480\,\text{min}$ was almost in the midpoint between the viscous end-member ($t_w = 45\,\text{min}$) and the elastic end-member ($t_w = 870\,\text{min}$), and the experiment produced a wide variety of curvatures, widths and tip shapes.

As an example of the temporal variation let us follow the primary finger of this experiment. We see that it initially is a seemingly viscous blob with rounded shape, however, with thin fractures pointing from it (figure 4.6(a)). The finger then grows to a thicker even more viscous-like blob (figure 4.6(b)), before secondary splitting occurs and it evolves into a narrow finger (figure 4.6(c)), however still with a fairly rounded tip shape. The tip shoots out to the cell edge and starts clinging to the edge (figure 4.6(d)). As it enters the shear zone at the edge it sharpens and form a acute but concave finger tip (figure 4.6(e)).

The spatial tip shape variation was also substantial, as presented in figure 4.13, where we present three highly different tip shapes on the same frame. Ranging from the sharpened but concave primary finger tip, to the wedge-like shape with small perturbations at the secondary finger tip, and to the tertiary finger's more hydraulic-fracture-like tip shape.

These observations of coeval viscous and elastic effects show that our experiments explore a truly viscoelastic regime. If we compare them with similar intrusion experiments on viscoelastic fracturing in Hele-Shaw cells, like Lemaire et al. (1991)[15], figures 2.16 and 2.19, and Hirata (1998)[8], figure 2.20, we see that although there are similarities on the actual intrusion morphologies, the use of polariscopy in our experiment allows to observe cracks thin like hair strands, which are not seen in their results.

The revelation of hidden fracture patterns through the means of polariscopy, is perhaps the most interesting observation in our results. In fact all thin fractures observed between polarizers were found to be invisible to the naked eye. Unfortunately, this revelation was realized after the experiments, so no imagery confirming this claim is available.

Table 5.1: Rheological classification of set 1, showing the intrusion type (IT) dependence on laponite waiting time t_w. The intrusion types are viscous fingering (VF), viscoelastic fracturing (VEF), and elastic fracturing (EF).

N	t_w	IT
1	45	VF
4	240	VEF
5	360	VEF
6	480	VEF
7	600	VEF
8	870	EF

5.2.2 Rheological categories

In short, a plethora of viscous, elastic, and hybrid effects can be seen in our experiments with different laponite waiting times. From the discussion of laponite's rheological response to injected oil we conclude that laponite viscosity and elasticity increases with laponite waiting time. Using a morphological comparison we classify our results into three commonly used categories of rheological response to fluid injection into a gel matrix: viscous fingering (VF), viscoelastic fracturing (VEF), and elastic fracturing (EF). Table 5.1 lists the fingering/fracturing dependence on laponite waiting time.

5.2.3 Effect of varying injection fluid rheology

In set 3 (section 4.3) we see that morphological and rheological response is indeed dependent on viscosity ratio.

In figure 4.26 we see the time development of oil injected into laponite gel producing wide fingers with blunted tips propagating in along the centerline of the cell. As the flow rates are high, $Q = 10\,\mathrm{mL\,min^{-1}}$, we observe wake turbulence, tip narrowing, and branching, which is typical for viscous shear-thinning rheologies at high flow rates[9]. Semi-ductile like shear zones are barely visible close in the birefringence patterns close to the cell edges, correlating with shear-thinning behavior. The primary finger reaches the far end of the cell in 12 s.

For comparison figure 4.25 shows the time development of deionized water injected into laponite gel. The injected water forms a very narrow fracture like intrusion shape, with concave tip shape, which split at an 50° angle propagating to the edge and clings to it. The morphology is typical for hydraulic fracturing (see section 2.2.4). This fracture propagates very fast and travels the entire length of the cell in approximately 3 s. The difference

in morphology and flow between the two experiments is vast.

Using the viscosities from the rheometric measurements (section 3.3.3) we are able to determine the viscosity contrasts of the two fluids to the laponite gel. The water to laponite viscosity contrast has an order of magnitude of 5, while the olive oil to laponite viscosity contrast has an order of magnitude of 3.

Rubin propose that considering expected ratios of the excess magma pressure at the dyke entrance to the elastic stiffness of the host rock, the host rock has to have a viscosity contrast of 11 to 14 orders of magnitude to the magma to behave as essential elastic during dyke intrusion. For dyke width to length aspect ratios of 10^-1 he finds that a viscosity contrast of 6 to 8 orders of magnitude is sufficient. Disregarding the ratios of excess pressure to elastic stiffness in the laponite we achieve elastic behavior for smaller width to length aspect ratios, with a viscosity contrast of only 5 orders of magnitude. Moreover, at only 2 orders of magnitude lower viscosity contrast, the rheological behavior is viscous and shear-thinning.

However, there is one parameter difference that might make this hypothesis of viscosity ratio dependence weaker. The interfacial tension between olive oil and water $\gamma_{oil/water} \approx 16.42\,\mathrm{mN\,m^{-1}}$ [41] is higher than the assumed interfacial tension between laponite and water, which we assume is negligible as water is miscible with laponite. The interfacial tension is seen to widen fingers in viscous fingering[1].

In addition it should strongly be noted that the cell used in the oil injection, having a similar aspect ratio to the cell used for the water injection, had just half the gap height H of the other. According to Lemaire et al. (1991)[15] narrower gaps would promote elastic response in the matrix (see section 5.1.3.2 for validation of this claim). The laponite used in the oil injection also had a 5 min longer waiting time which also should promote elastic response (see section 3.3.2.5).

Thus, we conclude that large viscosity ratios between fluid and matrix promote elastic behavior, whereas small viscosity ratios promote viscous behavior. This can also be substantiated by the results of Lemaire et al., where he saw that using the injecting the more viscous dodecane, as supposed to water, into a smectic clay, caused a shifting of his phase diagram towards viscous behavior[15].

Chapter 6

Conclusion

6.1 Method

In this thesis I develop a novel concept for extracting the stress-strain relationships and deformation features in viscous fingering and hydrofracturing caused by fluid injection into complex viscoelastic and shear-thinning materials.

Using a prototype I made myself, I explore the limitations and validity of using optical rheometry and velocimetry in couple to observe stress birefringence and particle flow in the gel matrix, and infer qualitative constraints on the rheological response. From viscous and elastic behavior, to the more complex viscoelastic and shear-thinning response. In fact we observe predominantly viscous and elastic features appearing simultaneously alongside transitional behavior which varies both temporally and spatially.

The simple and cost effective prototype setup provides a vast number of qualitative results, and we conclude that with the right modifications and improvements, the setup will be a valuable asset in the research of intrusion response in complex rheologies. With time we believe that quantitative stress-strain data can be extracted and a with proper scaling of the experimental model we may be able to answer the questions on transitional magma behavior which we posed in the introduction.

6.2 Physical interpretation

A significant conclusion from the experiments is that the rheological response in a gel matrix subjected to fluid injection is indeed dependent on viscosity ratio.

We have also seen that the use of polariscopy enables us to see cracks that are invisible to the naked eye. These cracks can be seen also when the intrusion morphology itself suggests viscous or viscous shear-thinning behavior. Several similar studies on viscous fluid injection into a viscoelastic matrix use intrusion morphology analysis to infer matrix rheological response. Our observations suggests that the conclusions made in these studies need to be reconsidered.

Bibliography

[1] C. Chevalier, a. Lindner, M. Leroux, and E. Clément. "Morphodynamics during air injection into a confined granular suspension". In: *Journal of Non-Newtonian Fluid Mechanics* 158.1-3 (May 2009), pp. 63–72.

[2] Benoit Cordonnier, Michael Manga, Melanie Forien, Boris Kauss, Philippe Yamato, and Thibault Duretz. "Non-Newton Man: An exploration of magmatic shear thinning sources." In: *EGU General Assembly Conference Abstracts*. Vol. 15. 2013, p. 12744.

[3] E. Di Giuseppe, F. Funiciello, F. Corbi, G. Ranalli, and G. Mojoli. "Gelatins as rock analogs: A systematic study of their rheological and physical properties". In: *Tectonophysics* 473.3-4 (Aug. 2009), pp. 391–403.

[4] Petri Fast, L. Kondic, Michael J. Shelley, and Peter Palffy-Muhoray. "Pattern formation in non-Newtonian Hele–Shaw flow". In: *Physics of Fluids* 13.5 (2001), p. 1191.

[5] Haakon Fossen. *Structural geology*. Cambridge University Press, 2010.

[6] Gerald G Fuller. *Optical Rheometry of Complex Fluids*. New York, NY: Oxford Univ. Press, 1995.

[7] Henry Selby Hele-Shaw. "The flow of water". In: *Nature* (1898).

[8] T. Hirata. "Fracturing due to fluid intrusion into viscoelastic materials". In: *Physical Review E* 57.2 (Feb. 1998), pp. 1772–1779.

[9] F.A. Holland. *Fluid flow for chemical engineers*. Edward Arnold, 1973.

[10] MK Hubbert. "Theory of scale models as applied to the study of geologic structures". In: *Geological Society of America Bulletin* (1937).

[11] J. Hutton. *Theory of the earth; or an investigation of the laws observable in the composition, dissolution and restoration of land upon the globe. (From. the Trans., Roy. soc. of Edinb.).* 1788.

[12] J. C. Jaeger, N. G. W. Cook, and R. W. Zimmerman. *Fundamentals of rock mechanics 4th edition*. Malden, USA: Blackwell Publishing Ltd, 2007.

[13] Manish Kaushal and Yogesh M. Joshi. "Linear viscoelasticity of soft glassy materials". In: *Soft Matter* 10.12 (2014), p. 1891.

[14] Ljubinko Kondic, Michael Shelley, and Peter Palffy-Muhoray. "Non-Newtonian Hele-Shaw Flow and the Saffman-Taylor Instability". In: *Physical Review Letters* 80.7 (Feb. 1998), pp. 1433–1436.

[15] E Lemaire, P Levitz, G Daccord, and H Van Damme. "From viscous fingering to viscoelastic fracturing in colloidal fluids". In: *Physical review letters* (1991).

[16] Anke Lindner, Daniel Bonn, Eugenia Corvera Poiré, Martine Ben Amar, and Jacques Meunier. "Viscous fingering in non-Newtonian fluids". In: *Journal of Fluid Mechanics* 469.October 2002 (Oct. 2002).

[17] Anke Lindner and Christian Wagner. "Viscoelastic surface instabilities". In: *Comptes Rendus Physique* 10.8 (Nov. 2009), pp. 712–727.

[18] J.G. Moore and T.W. Sisson. "Geologic map of the Triple Divide Peak quadrangle, Tulare County, California". In: *US Geol. Surv. Map* GQ-1636 (1987).

[19] M. O'Meara. "Determination of the Interfacial Tension Between Oil-Steam and Oil-Air at Elevated Temperatures". In: (2012).

[20] B. Persson and E. Brener. "Crack propagation in viscoelastic solids". In: *Physical Review E* 71.3 (Mar. 2005), pp. 1–8.

[21] Nick Petford. "Dykes or diapirs?" In: *Transactions of the Royal Society of Edinburgh: ...* (1996).

[22] Nick Petford and JD Clemens. "Granites are not diapiric!" In: *Geology Today* October (2000), pp. 180–184.

[23] W.S. Pitcher. "The nature, ascent and emplacement of granitic magmas". In: *Journal of the Geological Society* 136.6 (Dec. 1979), pp. 627–662.

[24] Daniel Post. "Photoelastic-fringe Multiplication - For Tenfold Increase in Sensitivity". In: *Experimental Mechanics* (1970), pp. 305–312.

[25] K. Ramesh. *Digital photoelasticity: advanced techniques and applications*. v. 1. Springer-Verlag, 2000.

[26] Giorgio Ranalli. *Rheology of the Earth*. Springer, 1995.

[27] N.V.N. Ravi Kumar, K. Muralidhar, and Yogesh M. Joshi. "On the refractive index of ageing dispersions of Laponite". In: *Applied Clay Science* 42.1-2 (Dec. 2008), pp. 326–330.

[28] M. Reiner. "The Deborah Number". In: *Physics Today* 17.1 (1964), p. 62.

[29] Rockwood Additives. *Laponite: performance additives*. Tech. rep. 2012.

[30] Allan M. Rubin. "Dikes vs. diapirs in viscoelastic rock". In: *Earth and Planetary Science Letters* 119.4 (Oct. 1993), pp. 641–659.

[31] Allan M. Rubin. *The transition from diapirism to dike intrusion: implications for planetary volcanism*. Tech. rep. 1993.

[32] Allan M. Rubin and Dominique Gillard. "Dike-induced earthquakes: Theoretical considerations". In: *Journal of Geophysical Research* 103.B5 (1998), p. 10017.

[33] AM Rubin. "Propagation of magma-filled cracks". In: *Annual Review of Earth and Planetary Sciences* (1995), pp. 287–336.

[34] Barbara Ruzicka and Emanuela Zaccarelli. "A fresh look at the Laponite phase diagram". In: *Soft Matter* 7.4 (2011), pp. 1268–1286.

[35] P. G. Saffman and Geoffrey Taylor. "The penetration of a fluid into a porous medium or Hele-Shaw cell containing a more viscous liquid". In: *Proceedings of the Royal Society. Series A: Mathematical and Physical Sciences* 245.1242 (1958), pp. 312–329.

[36] PG Saffman. "Viscous fingering in Hele-Shaw cells". In: *Journal of Fluid Mechanics* (1986), pp. 73–94.

[37] F.W. Sears. *Optics*. Addison-Wesley, 1946.

[38] T. Al-Shemmeri. *Engineering Fluid Mechanics*. Bookboon, 2012.

[39] JM Soulages. "Flow birefringence and velocity measurements for polymer melts in a cross-slot flow channel". In: (2007).

[40] Ikuro Sumita and Yukari Ota. "Experiments on buoyancy-driven crack around the brittle–ductile transition". In: *Earth and Planetary Science Letters* 304.3-4 (Apr. 2011), pp. 337–346.

[41] P Than, L Preziosi, DD Josephl, and M Arney. "Measurement of interfacial tension between immiscible liquids with the spinning road tensiometer". In: *Journal of colloid and interface ...* (1988).

[42] The Society of Rheology. "Official symbols and nomenclature of The Society of Rheology". In: *Journal of Rheology* 57.4 (2013), p. 1047.

[43] VEB MLW. *Instruction Manual Viscosimeter B3*.

[44] Jiri Vejrazka. *PIVsuite*. 2014. URL: http://www.mathworks.com/matlabcentral/fileexchange/45028-pivsuite.

[45] Wikipedia. *Refractive index — Wikipedia, The Free Encyclopedia*. [Online; accessed 10-July-2014]. 2014. URL: %5Curl%7Bhttp://en.wikipedia.org/w/index.php?title=Refractive_index&oldid=616284450%7D.